POLITECNICO DI MILANO

School of Industrial and Information Engineering
Department of Aerospace Science and Technology (DAER)
Master of Science in Space Engineering

Master Thesis

Spacecraft re-entry predictions through semi-analytical orbit propagation and differential algebra

Supervisor:
Dr. Camilla Colombo

Co-supervisor:
Dr. Alexander Wittig

Candidate:
Claudia Castracane

Academic Year 2019-2020

When referring to this work, full bibliographic details must be given, i.e.
Castracane Claudia "Satellite re-entry predictions through semi-analytical orbit propagation and differential algebra". 2020, Politecnico di Milano, Faculty of Industrial Engineering, Department of Aerospace Science and Technologies, Master in Space Engineering, Supervisor: Camilla Colombo, Co-supervisor: Alexander Wittig

Printed in Italy

To my parents, Sonia and Bruno,
and to my sister, Federica.

Je me demande si les étoiles sont éclairées afin
que chacun puisse un jour retrouver la sienne.

Antoine de Saint-Exupéry

Acknowledgements

Giunti alla fine di questo lungo, faticoso ma appagante percorso desidero ringraziare tutte le persone che ne hanno preso parte, per un tratto più o meno breve.
Esordisco ringraziando in primis la mia relatrice, la Dr. Camilla Colombo, e il mio correlatore, il Dr. Alexander Wittig, per avermi dato l'opportunità di lavorare su questa tesi. Vi ringrazio per la vostra pazienza, le vostre cortesi e chiare spiegazioni, vi sono grata per avermi trasmesso la passione per i temi trattati in questo elaborato.
Grazie mamma, grazie papà, grazie infinite. Grazie per il vostro sostegno e il vostro appoggio. Grazie per avermi sempre fatto percepire la vostra presenza nonostante i chilometri di lontananza. Siete stati con me a Milano, a Southampton ed infine a Zurigo, e sono certa che ovunque la vita mi porterà voi sarete sempre al mio fianco, con le nostre infinite telefonate e il mio occupare l'intero spazio sonoro quando parlo, come dice papà.
Grazie alla mia sorellina Federica, che ormai tanto piccola non è. Non nego che nonostante gli anni di differenza vedo te come un modello da seguire. La tua bontà, la tua pazienza e le tue mille attenzioni per gli altri sono ammirevoli, e spero con il tempo di arrivare ad assomigliarti almeno un po'. Grazie per i tanti abbracci, rispettando il silenzio quando le parole non servivano a consolare.
Ringrazio con tutto il cuore le mie nonne, perchè sono sempre state con me e mi hanno costantemente fatto sentire a casa. Grazie nonna di Guardiagrele per i sughi, che hanno allietato i miei pranzi inglesi, e per condividere con me i tuoi ricordi svizzeri. Le preghiere di nonna di Chieti Scalo sono state una certezza, ed hanno certamente contribuito alla mia riuscita negli esami.
Grazie Giovanni, non ho timore di dire che senza di te questa tesi non esisterebbe. Sono stati mesi difficili ma grazie di essere ancora qui al mio fianco, a cercare di darmi comprensione e amore. Sei stato il regalo più grande che il Polimi potesse farmi.
Voglio inoltre ringraziare tutti gli amici di sempre e quelli conosciuti in questi anni. Grazie per aver condiviso con me le confidenze più intime, e per il vostro supporto durante tutti i momenti in cui sentivo di non essere abbastanza.
Grazie.

Summary

The thesis defines a numerical model for the re-entry prediction in the differential algebra mathematical environment, describing the orbit propagation through semi-analytical methods. The spacecraft is represented as a point-mass and its orbital dynamics is analysed under the presence of uncertainties in the initial conditions.
Spacecraft re-entry in the Earth's atmosphere poses a serious threat to the population and activities on ground. Uncertainties affecting the orbital environment and the spacecraft state cause typical prediction errors to often exceed thousands of kilometres, even when simulations are issued one or two hours before the actual event. Therefore, significant research efforts aim at developing fast and accurate methods for re-entry predictions.
Differential algebra allows to represent the satellite state through Taylor series of the initial uncertain variables. The spacecraft dynamics, expressed in averaged form, is propagated until the eventual re-entry. Semi-analytical methods are used to model the effect of the atmospheric drag on the orbital semi-major axis and eccentricity. The resulting polynomial expansion is then evaluated for a cloud of displaced conditions without performing additional integrations.
The thesis provides the mathematical formulation of the re-entry trajectory, and an analysis of the features of the numerical environment proposed. A special attention is given to the implementation of the domain splitting and constraint satisfaction routines, which are essential to guarantee the method convergence. Finally, the innovative methodology is tested on the historical re-entry of two objects, the GOCE satellite and the Chinese space station Tiangong-1, demonstrating its accuracy and computational time savings, compared with a numerical Monte Carlo simulation. In fact, Monte Carlo methods require a large number of samples to give statistically meaningful results, becoming tremendously expensive. The methodology investigated within the present study allows to increase the number of samples without compromising the computational burden.

Keywords: Re-entry problem; Differential Algebra; Semi-analytical methods.

Sommario

Il presente lavoro di tesi definisce un modello numerico per le previsioni del rientro di veicoli spaziali, nell'ambiente matematico dato dall'algebra differenziale, e propagando la traiettoria con metodi semi-analitici. Lo spacecraft è rappresentato come un punto materiale e la sua dinamica è analizzata in presenza di incertezze nelle condizioni iniziali.
Il rientro dei velivoli in atmosfera rappresenta una seria minaccia per la popolazione e le attività sulla Terra. Incertezze riguardanti l'ambiente orbitale e lo stato dello spacecraft comportano che le previsioni siano spesso caratterizzate da errori che eccedono migliaia di chilometri, anche quando le simulazioni sono rilasciate una o due ore prima il verificarsi dell'evento stesso. Ne consegue che ingenti sforzi di ricerca sono volti a sviluppare metodi veloci e accurati per le previsioni del rientro.
L'algebra differenziale permette di rappresentare lo stato del satellite attraverso serie di Taylor, in funzione delle variabili caratterizzate da incertezze. La dinamica dello spacecraft, espressa in forma mediata, è propagata fino all'eventuale rientro. L'effetto dell'attrito atmosferico sul semiasse orbitale e l'eccentricità è modellato attraverso metodi semi-analitici. L'espansione polinomiale che ne risulta è quindi valutata per una nuvola di punti senza il bisogno di integrazioni aggiuntive.
La tesi presenta la modellizzazione matematica del rientro di un satellite in atmosfera e analizza diverse caratteristiche dell'ambiente numerico proposto. Un'attenzione particolare è data all'implementazione delle tecniche di domain splitting e constraint satisfaction, essenziali per garantire la convergenza delle simulazioni realizzate. Infine, il modello proposto è testato su due effettivi casi di rientro, il satellite GOCE e la stazione spaziale cinese Tiangong-1, con lo scopo di dimostrare l'accuratezza e il risparmio computazionale rispetto alle simulazioni numeriche di tipo Monte Carlo. Infatti, quest'ultimo richiede un alto numero di campioni per dare risultati statisticamente significativi e può così diventare eccessivamente costoso. Il modello sviluppato nella presente tesi permette di aumentare il numero di campioni senza compromettere il costo computazionale.

Parole chiave: Rientro in atmosfera; Algebra Differenziale; Metodi semi-analitici.

Contents

List of Figures

List of Tables

Nomenclature

Symbols

R_E	Earth's radius	6378.16 [km]
μ	Earth's gravitational parameter	398,600 [km^3/s^2]
A	Cross sectional area of the spacecraft	[m^2]
a	Semi-major axis	[km]
a_{drag}	Acceleration due to drag	[kg/s^2]
α	Right ascension	[rad] or [deg]
β	Azimuth	[rad] or [deg]
c	Auxiliary variable	[-]
C_D	Drag coefficient	[-]
δ	Declination	[rad] or [deg]
δ_r	Area to mass ratio	[m^2/kg]
E	Eccentric anomaly	[-]
e	Eccentricity	[-]
e_b	Eccentricity boundary condition	[-]
ϕ_{fpa}	Flight path angle	[rad] or [deg]
H	Scale height	[km]
h	Altitude	[km]
i	Inclination	[rad] or [deg]
$I_n(x)$	Modified Bessel function of first kind, of order n	[-]
J_2	First order zonal harmonics of the Earth's gravity field	[-]
M	Mean anomaly	[rad] or [deg]
m	Mass spacecraft	[kg]
n	Mean motion	[1/s]
Ω	Right ascension of the ascending node	[rad] or [deg]
ω	Argument of perigee	[rad] or [deg]
P	Orbital period	[s]
p	Semi-latus rectum	[km]

r	Position magnitude	[km]
ρ	Density	[kg/m^3]
ρ_p	Partial density	[kg/m^3]
σ	Standard deviation	[-]
t	Time	[s]
θ, ν	True anomaly	[rad] or [deg]
T_∞	Reference temperature	[K]
v	Velocity magnitude	[km/s]

Acronyms

CS	Constraint Satisfaction
DACE	Differential Algebra Computationa Engine
DA	Differential Algebra
DS	Domain Splitting
ESA	European Space Agency
FPA	Flight Path Angle
GOCE	Gravity field and steady-state Ocean Circulation Explorer
GTO	Geostationary Transfer Orbit
KH	King-Hele
PDF	Probability Density Functions
SA	Semi-analytical
SI-KH	SuperImposed King-Hele
TLE	Two-Line Elements

Chapter 1

Introduction

1.1 Background

As of 4 March 2020, since the decay of the Sputnik 1 launch core stage on December 1st 1957, 45,326 catalogued objects, including space debris, reentered the Earth's atmosphere[1]. Each day, satellites, rocket stages or fragments reenter the denser layers of the atmosphere, where they usually burn up. Although, the re-entry frequency varies with the object size. Indeed, only a few large objects, such as heavy scientific satellites and exhausted rocket stages, reenter the Earth's atmosphere once a year. Objects of moderate size, i.e. 1 m or above, reenter about once a week, while on average two small tracked debris objects reenter per day[2].
From an altitude of 110 km, during the last 10 minutes before an object reaches the ground, the atmosphere is dense enough that the object heats up due to air drag, and it decelerates, leading in the majority of cases to its complete demise. Therefore, reentering objects pose only a marginal risk to people or infrastructure on the ground or to aviation. However, in rare events, fragments may reach the ground, thus, it is important to monitor the risk to the population[2]. In addition, re-entry models are intrinsically multidisciplinary. They need to include both characteristics of the object involved and environmental features. In fact, they need to account for the attitude and the aerodynamic shape of the body, its orbital state and evolution, and the surrounding Earth's atmosphere, which influence is heavily dependant on the Sun activity and local variations in the aerosol distribution. Re-entry is an extremely complex phase because it constitutes

[1]Space Track Organization, *Satellite Catalogue*: `https://www.space-track.org/#catalog`, accessed: 04/03/2020.

[2]ESA website, *Reentry and collision avoidance*: `https://www.esa.int/Safety_Security/Space_Debris/Reentry_and_collision_avoidance`, accessed: 14/04/2020.

a transitory state between the nominal orbital equilibrium and the break-up due to air friction. The uncertainties on the model parameters affect re-entry predictions so deeply that a slight change can potentially cause drastic variation in re-entry epoch and region. Often, the large number of uncertainties in the orbit and space environment affecting the satellite, lead to indications for re-entry period and location that span over several days, in a latitudinal region between the orbital inclination of the spacecraft itself. Hence, a comprehensive formulation of the re-entry problem is a non-trivial task, while considering all the sources of uncertainty can easily become time consuming. Improving the re-entry predictability and the easiness to perform the simulations are contemporary topics, which are worth to deepen to lower or at least to limit the risk for the population.

Re-entry prediction is done by propagating an object until it reaches the altitude where the atmospheric break-up occurs, which is typically between 72 and 84 km[3]. Atmospheric drag is the main cause of orbital decay, it lowers the speed and the height of a spacecraft. In addition, the collisions of gas molecules with the satellite produce friction, heating it up. Eventually, drag leads to the break-up of the main body and a partial burning of the components. The perturbing acceleration depends on the spacecraft drag coefficient, C_D, the area-to-mass ratio, A/m, the velocity with respect to the atmosphere, $\boldsymbol{v}_{rel}$ and on the atmospheric density, ρ, as provided in Equation (1.1) (Vallado [2013]).

$$\boldsymbol{a}_{drag} = \frac{1}{2} C_D \frac{A}{m} \rho v_{rel}^2 \frac{\boldsymbol{v}_{rel}}{|\boldsymbol{v}_{rel}|} \tag{1.1}$$

The drag coefficient is generally uncertain and the area-to-mass ratio depends on the object's attitude which is often unknown. The local atmospheric density, on the other hand, depends on the solar and geomagnetic activity, which are difficult to predict. As a result, the uncertainties in the physical parameters describing the drag effects, cause the corresponding acceleration component to be challenging to estimate.

Due to the increasing number of objects in space, guidelines and recommended procedures are required to reduce the number of non-operational spacecrafts and spent rocket upper stages orbiting the Earth[3]. One method of post-mission disposal is to allow the re-entry of these spacecrafts, either from natural orbital decay, which is uncontrolled, or controlled entry. Uncontrolled re-entry is performed by lowering the perigee altitude, so that atmospheric drag will finally cause the spacecraft to enter the Earth's atmosphere more rapidly. Therefore, the re-entry is associated with a certain impact risk, since it is not guaranteed that the surviving debris would reach the Earth's surface in inhabited landmasses. Controlled re-entry is achieved by using a propulsion system, causing the

[3]NASA website, *Debris Reentry*: `https://orbitaldebris.jsc.nasa.gov/reentry/`, accessed: 14/04/2020.

spacecraft to enter the atmosphere at a steeper flight path angle. The vehicle will then enter the atmosphere at a more precise latitude and longitude, and the debris footprint can be positioned over an uninhabited region, generally located in the ocean. NASA-STD 8719.14[4] is a document which provides specific technical requirements and methods for limiting orbital debris. The scope is to ensure that the spacecraft and launch vehicles meet acceptable standards for limiting orbital debris generation. Reentries compliant with it must have a human casualty expectancy (i.e. the chance that anybody anywhere in the world will be injured by a piece of debris) lower than 1:10,000. Such alert threshold is now adopted by several organizations in the United States, Europe and Japan (Pardini and Anselmo [2012]).

The satellite state for re-entry predictions is often based on Two-line Elements (TLE), being the only public data source currently available for determining the orbit of a space object. TLEs are generated using Simplified General Perturbations (SGP4), and Simplified Deep Space Perturbations (SDP4) force models, which are based on the Brouwer theory (Brouwer [1959]) and only include the largest perturbations: J_2 to J_5 zonal harmonics, simplified drag and third body and solar radiation pressure. The assumptions can severely limit the accuracy of SGP4 propagation. Because many short-periodic perturbations are not taken into account, the maximum possible accuracy is limited (Gondelach et al. [2016]).

Re-entry predictions can be distinguished by their forecasting period into long term, medium term, short term. Short-term predictions range from several days to hours before re-entry, starting from around 200 until 80 km altitude, when break-up commonly occurs. Short-term predictions commonly report the expected decay epoch and the associated uncertainty as a percentage of the remaining orbital lifetime. The uncertainty in remaining time can be used to compute the potential footprint along the satellite ground-track (Geul et al. [2018]).

1.2 State of the art

This section provides an analysis of past research efforts concerning the re-entry problem, and it presents the current state-of-the-art for the applications of the differential algebra, especially within the astrodynamics field. In addition, it gives an overview on the spacecraft dynamics fields where semi-analytical methods are exploited.

[4]NASA website, *Process for Limiting Orbital Debris*: `https://standards.nasa.gov/standard/nasa/nasa-std-871914`, accessed: 13/05/2020.

1.2.1 Re-entry predictions

Re-entry prediction is a topic frequently addressed in literature. It is extremely difficult to exactly forecast re-entry epoch and region, even few hours before the actual decay. For this reason, a massive research effort is invested in this field, in order to exactly model all the parameters involved, making predictions more reliable.
Forecasts are affected by various sources of uncertainty, and mean relative errors in the re-entry epoch of 20% are typical. This means that predictions issued three hours before re-entry may be affected by an along-track uncertainty of 40,000 km, corresponding to one orbital path, possibly halved during the last hour (Pardini and Anselmo [2013]). The relative prediction error of ±20% is suggested by Pardini and Anselmo [2013] as the result of re-entry campaigns involving a list of 15 objects, comprising mainly spacecrafts and rocket bodies, and it should be adopted to compute the uncertainty windows covering all the possible error sources. The authors investigate the main features of re-entry statistics, with particular concern on uncontrolled spacecrafts, which often violate the alert causality expectancy threshold. The authors evaluate the re-entry risk by listing all the prediction uncertainties affecting the quality of the forecasts. Main causes of the poor predictability are uncertainties in the initial state, due to sparse and inaccurate tracking data, inaccuracies concerning environment models, which affects the computation of the density at the altitude of interest, and the evolution of the attitude, which can be difficult to model in the case of complicate shapes, or even completely unknown. In addition, more demanding conditions occur in the presence of high solar and geomagnetic activity, solar flare and coronal mass ejection alert and/or satellites of particular complex shape and attitude dynamics. In such cases, a more conservative prediction error of ±25/30% should be considered, especially during the last 2-3 days of residual lifetime. In another research work, Pardini and Anselmo [2018] investigate the risk represented by the uncontrolled re-entry of sizable spacecraft and upper stages. Overall, the mean prediction error is about 10%, increasing to 15% in the last 6 hours. It is explained that for the statistical distribution of the predictions, the amplitude of about ±20% around the nominal re-entry time is required to guarantee a confidence level of 90%. While a confidence level ≥95% is reached with an uncertainty window amplitude of ±30%. Moreover, it is found that the residual lifetimes are overestimated in approximately 40% of the cases, and underestimated in the remaining 60%, supporting the adoption of asymmetric re-entry uncertainty windows, with “tails” longer than “heads”.
Geul et al. [2018] analyse short-term re-entry predictions, focusing, in detail, on improving the state-of-the-art of the aerodynamic modeling and the statistical uncertain propagation. In particular, initial state uncertainties are estimated for Global Positioning System (GPS), and two-line elements. They propose a full-six-degree-of-freedom (DoF) model,

which improves the fidelity of the simulations, while reducing the number of assumptions on the evolution of the satellite's altitude. The aim of the article is to investigate the effect of uncertainties by studying the past re-entry of ESA's Gravity field and steady-state Ocean Circulation Explorer (GOCE) satellite. The analysis demonstrates that the atmospheric uncertainty is the primary driver of the decay-time distribution. Moreover, the statistically obtained windows are on average narrower than the Tracking and Impact Predictions (TIP) windows, which are publicly released by the Joint Space Operations Center (JSpOC).

Regarding the GOCE satellite, the huge amount of data available has resulted in a massive research effort concerning its re-entry, which is widely documented in literature. In the work done by Cicalò et al. [2017], the primary objective is to fully exploit the information content of the GOCE data collected during its re-entry phase for better understanding re-entry predictions. Thanks to the high accuracy of the GPS and attitude measurements, which would allow a Precise Orbit Determination (POD) of the spacecraft, GOCE data are used to assess the quality of external measurements and to characterise the corresponding re-entry predictions uncertainties.

Minisci et al. [2017] study the propagation of uncertainties on the atmospheric re-entry time, focusing on the GOCE decay. They consider 3 and 6 DoFs models, and uncertainties on the initial conditions, the atmospheric and shape parameters. They intentionally avoid the use of standard Monte Carlo (MC) methods, which can lead to unreasonable computational time. In their research they also discard the hypothesis of using intrusive techniques as Taylor differential algebra, opting for a non-intrusive method called Adaptive High-Dimensional Model Representation (AD-HDMR). The method decomposes the stochastic space into sub-domains of lower dimensionality, and models each of them with the most appropriate technique. The resulting model is therefore a summation of contributions from each sub-domain. The inclusion of uncertainties in the initial conditions lead to a statistical characterisation of the coefficients and representation of possible trajectories. Results have pointed out shapes of the Probability Density Functions (PDFs) for the re-entry time depending on the degrees of freedom (3 or 6).

Sánchez-Ortiz et al. [2017] investigate the re-entry of the GOCE satellite. In particular, it is studied the impact of the atmosphere uncertainties derived from space weather aspects, also comprising unexpected solar storms, which pose a major challenge to accurate re-entry predictions. Moreover, the paper describes the achievable accuracy of the estimation of the position and velocity of a re-entering object, and how it is translated into the re-entry prediction errors. It is proven that the size of the position and velocity uncertainty directly map to the re-entry prediction error. It is also concluded that velocity plays a major role in the prediction error, compared with position incertitude.

The accuracy of re-entry prediction is often limited by the quality of the publicly available TLEs. Some of them may be erroneous state vectors which should not be considered in the attempt to mathematically forecast the re-entry trajectory. Geul et al. [2017] define an uncertainty estimation for TLE, both classical and enhanced, using robust weighted differencing. Mathematical estimation of TLE error is in fact necessary, since no satellite orbit error is available for TLE. The method is described accurately, and also tested and compared with other methods. Therefore, it is advocated to be more reliable than previous differencing methods for TLE uncertainty. The validation is based on the GOCE satellite, using the dozens of TLE data available in the weeks prior to its re-entry. Armellin et al. [2016] propose a methodology to improve the accuracy of the TLE-based re-entry prediction by implementing a multi-stage TLE filtering, based on robust statistics and regression methods. The proposed algorithm is validated on the re-entry of rocket bodies located in Geostationary Transfer Orbits (GTO), characterised by high eccentricities. Their re-entry might be associated with high on-ground casualty risk, since spent upper stages consist of components likely to survive re-entry, as propellant tanks. It is observed that re-entry prediction accuracy may reduce due to TLE filtering, because fewer TLEs are available to perform object's parameters estimation and orbit determination. However, the research proves that filtering out the outlying TLEs is vital in order to reduce the prediction errors. An extension to the previous research is given by Gondelach et al. [2016]. The authors introduce a method which is constituted by four steps, consisting in TLEs filtering, the estimation of the ballistic coefficient and the initial state, and finally the prediction of the re-entry date. Again, TLEs are found to be the main reason for inaccurate predictions of the re-entry date and for failures in the orbit determination. Moreover, TLEs result to be less accurate and less robust for objects in highly eccentric orbits, rather than for orbits with low eccentricity.

Often, the statistical dispersion of the impact epoch is expressed by means of Probability Density Functions (PDFs). PDFs not only provide the re-entry window, but also the probability associated to each time interval. Ronse and Mooij [2013] propose a method, based on TLE data, to statistically predict the impact and location of orbital objects under 200 km altitude, investigating also the influence of the parameter uncertainties on the statistical dispersion. The result is a probability density faction of the impact time, and a ground map expressing the impact probability. The method's performance is tested by a comparative study with the tracking and impact predictions published by the U.S. Space Surveillance Network, providing a good match. On average, for all the case tested, the impact window is 15% smaller, but the true impact is always contained, proving the reliability of the method. Another study, carried on by Hoogendoorn et al. [2017], investigates a method to directly propagate a probability density function in time,

which has the potential to obtain more accurate results with less computational effort, compared with the traditional and time consuming Monte Carlo method. Although, no accurate impact-time distributions could be obtained, indicating that the methodology suffers from a curse of dimensionality which does not affect the MC method.
Trisolini and Colombo [2019] propose a density-based approach to propagate the probability distribution function of the re-entry uncertainties, using the continuity equation and the re-entry dynamics. The model considers uncertainties in the initial conditions (altitude, velocity, and flight path angle) and the ballistic coefficient of the satellite for different types of re-entry scenarios. The result is a quantification of the re-entry corridor, the impact location, and the casualty area. The methodology is able to provide statistically meaningful results with few sampled points, aiming at replacing Monte Carlo simulations, which are computationally expensive and require a large number of samples.
Concluding, re-entry strategies may involve a careful design of the spacecraft. Trisolini et al. [2017] recommend a spacecraft optimisation for demise and survivability. The implementation of design for demise strategies may favour the selection of uncontrolled re-entry, which are simpler and cheaper compared with controlled ones. It is also important to consider that a spacecraft designed for demise still has to survive the space environment for many years. Therefore, the design has also to comply with the requirements arising from the survivability against debris impacts. Two models are developed, aiming at assessing the demisability and the survivability of simplified mission designs. The optimiser is able to provide a wide range of solutions for different types of mission scenarios. The authors suggest that future developments will allow the optimisation of more complex spacecraft configurations, with many types of components (tanks, reaction wheels, batteries, etc.).

1.2.2 Differential algebra

The benefits arising from the use of Differential Algebra (DA) are widely advocated in literature. Differential algebra is introduced for the first time by Ritt [1950], and it is a numerical technique based on algebraic manipulation of polynomials. Some areas in which DA is successfully applied include accelerator physics and astrodynamics. Berz [1999] provides a general introduction to the single particle dynamics of beams, his work addresses the map theory for the description of the motion. The differential algebraic approach developed allows computations of nonlinearities of the maps to arbitrary order, and a transparent analysis of all relevant nonlinear effects. Di Lizia et al. [2007] propose a single-step integration scheme, that expresses the solution within the time step as high order Taylor expansion in time. Differential algebra allows to perform a high order

sensitivity analysis, since the solution can be expanded not only in time, but also in initial conditions and dynamical model parameters. To test the high order time integration scheme for implicit ODE problems, the motion of a controlled double-link manipulator is used. Differential algebra potentiality is also proven in the celestial mechanics field, which is the area of greatest interest for the scope of the present thesis.
Di Lizia et al. [2008] treat the two-point boundary value problems through high order expansion. The differential algebra is used to expand the solution around the reference one. The main advantage relies on the possibility to compute new solutions in a relatively large neighborhood of the reference condition through simple evaluation of polynomials. Astrodynamics problem, as halo orbits and aerocapture maneuvers, are tested to evaluate the performances of the method. The differential algebra framework used is implemented by Berz and Makino [2006], in the software COSY-Infinity. The article proves that the benefits of DA in the space trajectory design are undeniable. Ávila [2016] investigate the application of differential algebra techniques in orbital dynamics problems with uncertainties in the orbital determination. In particular, the DA propagator is tested in the field of asteroid impact risk monitoring. DA is advocated to halve the computational time, compared with the classical Monte Carlo simulation approach, while keeping the same level of precision. Wittig et al. [2014a] first propose the combination of differential algebra based methods with orbital elements averaging. The effect of orbit perturbations is fundamental when analysing the long-term evolution and stability of the motion of natural or artificial satellites. In particular, the models for the space debris evolution environment consider the effect of atmospheric drag, solar radiation pressure, anomaly of the Earth's gravity field and luni-solar perturbations. Semi-analytical technique based on averaging is an efficient approach, which allows to easily identify equilibrium, librational or rotational solutions. The averaging is performed, in Keplerian elements, on the true (or mean) anomaly. Applying the differential algebra to averaged equations is the best option in terms of computational time for the propagation of clouds, proving the efficiency of the methodology proposed.
The Differential Algebra Space Toolbox (DAST) for nonlinear uncertainty propagation in space dynamics, is developed by Rasotto et al. [2016]. The software DAST is in fact based on Taylor differential algebra, and it exploits the wide class of high-order methods. The Differential Algebra Computational Engine (DACE) has a core coded in Fortran, and two interfaces, C++ and Matlab. The software is applied to astrodynamics and space engineering examples, as the two body problem and the re-entry of the Hayabusa spacecraft. The results show that the final accuracy depends on the size of the uncertainty set considered, and on the order of the polynomials. Moreover, it proves the advantage given by differential algebra in terms of computational time, compared with classical approaches,

even if the time required for the simulations typically increases with the order and in the presence of large numbers of uncertainty variables. The modular design is also advocated to be beneficial, giving the possibility to apply DAST to any research field. In addition, Massari et al. [2018] propose a software library with automatic code generation for space embedded applications. The DA Core Engine 2.0 (DACE 2.0) is entirely developed in C11 with an interface in C++, its performances are proven to be superior compared with the first version DACE 1.0.
Sun et al. [2018] address the problem of propagating an initial orbital state around its reference value to a variable final time, in a DA-based framework. The authors introduce a high-order state transition polynomial including the time expansion (STP-T). The results show how the method provides a good approximation of the final state for the three orbital dynamics tested: unperturbed Keplerian dynamics, the J_2 perturbed Keplerian dynamics, and the nonlinear relative motion. Ortega Absil et al. [2016] propose a generalisation of Taylor differential algebra by using hyperinterpolation-based approaches, in particular truncated Tchebycheff series, which are part of the Generalised Intrusive Polynomial Expansion (GIPE). Differential algebra is proven to be more robust for dynamics presenting inherent singularities, while interval-based approaches are less prone to experience numerical instability when dealing with discontinuities and non-differentiabilities in the simulation model. The GIPE model is meant to be applied on the end-of-life analysis of Low Earth Orbit satellites, and validated on the de-orbiting and re-entry of the GOCE satellite. Wittig et al. [2015] introduce domain splitting to the propagation of large uncertainty sets in orbital dynamics. In fact, non-linearities of the dynamics can prevent the good convergence of Taylor expansion, in one or more directions. The domain splitting technique allows to split the polynomial expansion of the current state during the propagation itself. The routine acts automatically whenever the truncation error reaches a predefined threshold, the result is a list of final state polynomials. Accuracy is preserved and uncertainties are effectively tracked even in highly non-linear dynamics. The method is tested on the orbit of the asteroid (99942) Apophis, which propagation shows particularly high non-linearities close to the perigee passage.

1.2.3 Semi-analytical methods

Since the first launch of a man-made satellite in 1957, the study of the motion of an artificial satellite under the effect atmospheric drag has been intensive, due to the urgent need of understanding its dynamics and due to the vast potential in applications. It is well known that the dynamical system for the drag-coupled problem is nonlinear, non-conservative and complex in form, and the integration of the system, in general, is analytically intractable. Therefore one possibility is to deduce an approximate solution

with desirable accuracy. An overview of the first analytical and semi-analytical methods is available in Liu [1982].

The mathematical formulation of averaged equations for the semi-major axis and the eccentricity variations, under the influence of the atmospheric drag, was first developed by King-Hele [1964], who derived an analytical approximation of the integrals. Depending on the orbit eccentricity, different series expansions were found. Initially, the effect of air drag on satellite orbits of small eccentricity ($e < 0.2$) was studied on the assumption that the atmosphere was spherically symmetrical. The basic King-Hele (KH) formulation relies on the assumption that the atmosphere density decays strictly exponentially with altitude, meaning that the profile is characterised by a fixed scale height. Therefore, the theory has been extended multiple times, to take into account more complex density models. Cook et al. [1965] propose an atmospheric model that above 200 km exhibits a day-to-night variation, which is incorporated in the existing theory to make it more robust. Further research efforts done by Vinh et al. [1979] improve the method by removing the ambiguity arising from the regions of validity in eccentricity and applying a more rigorous Poincaré method for the integration. Swinerd et al. [1982] propose a model of the atmosphere that allows for oblateness and comprises a diurnal density variation, which consists in an improvement for the modeling of near circular orbits ($e \leq 0.01$) that have perigee altitudes greater than 200 km. Lately, Frey et al. [2019] extend the KH method by introducing an alternative atmosphere model derivative. The newly smooth density profiles, both static and dynamics, are derived from existing atmospheric models through a fitting procedure. By superimposing exponentially decaying partial atmospheres, the SuperImposed KH (SI-KH) method is more accurate, allowing for more complex density profiles. In fact, if the actual density profile does not satisfy the assumption of a fixed scale height, as is the case for Earth's atmosphere, the KH method introduces potentially large errors for non-circular orbit configurations, especially for highly eccentric orbits. As the assumption of a fixed scale height is satisfied for each component, the resulting decay rate is estimated with great accuracy. Finally, each individual contribution is summed up, resulting in the global contraction of the overall not strictly exponentially decaying atmosphere density. The KH method is further refined by deriving higher order terms during the series expansion, which guarantee a more reliable convergence of the averaged approach, compared with the full-dynamics, while saving computational effort.

Empirical and semi-empirical atmospheric models are partially or fully derived from a combination of satellite, radiosonde and ground-based measurements. A limited overview of existing models is provided below, in increasing degree of complexity.

The COSPAR International Reference Atmosphere (CIRA) proposes empirical models of atmospheric temperatures and densities as recommended by the Committee on Space

Research (COSPAR)[5]. It consists of a set of tables of average air pressures, altitudes and temperatures. The basic Jacchia atmospheric model (Jacchia [1977]) is static, and gives temperature and density profiles for the relevant atmospheric constituents for any specified exospheric temperature. Tables are given for heights from 90 to 2500 km and for exospheric temperatures from 500 to 2600 K. The Drag Temperature Model (DTM) (Bruinsma [2015]) is a semi-empirical model describing the temperature, density, and composition of the Earth's thermosphere. The total density data used in this study cover the 200–900 km altitude range and all solar activities.

Semi-analytical approximations of the full orbital dynamics are used in several researches available in literature. Bezděk and Vokrouhlický [2004] investigate long-term dynamics of low-altitude satellites or debris using a semi-analytic theory of motion, which is based on the classical work of King-Hele. The goal is to develop a fast computational tool enabling to propagate vast amounts of real or fictitious orbits which may be useful for studying multi-parameter orbital problems or evolution of a space debris population. The estimated lifetime differs from the observed value by a few percent typically. However, the error becomes about an order of magnitude worse for extrapolation to the future because of the limitations in the prediction of solar activity, to solve the issue more complex aerodynamic models should be included.

Colombo [2016] proposes a suite for long term propagation in perturbed environment, Planetary Orbit Dynamics (PlanODyn). The dynamic model is based on averaged equations, and the semi-analytical approximation for drag relies on the King-Hele theory. The scope is to provide a tool to identify deorbiting strategies exploiting the effects of orbit perturbations, optimising the re-entry trajectory from Highly Elliptical Orbits (HEOs) and the end-of-life re-entry through solar radiation pressure, as in the case of the INTEGRAL spacecraft. The suite PlanODyn is used by Colombo [2019] to deeply investigate the long-term evolution of spacecrafts in HEOs, which is heavily affected by luni-solar perturbation.

Colombo and McInnes [2011] apply the averaging technique, expressing the secular variation of Keplerian elements analytically. The scope is to prove how asymmetric solar radiation pressure and atmospheric drag could potentially be balanced to obtain long-lived Earth orbits for smart-dust devices.

Finally, Wittig et al. [2017] firstly introduce a methodology for orbit averaging based on both King-Hele formulation and DA techniques. The goal is to develop a method to

[5]NASA website, *ModelWeb Catalogue and Archive*: `https://ccmc.gsfc.nasa.gov/modelweb/models_home.html`, accessed: 15/04/2020.

propagate large clouds of initial conditions and their associated probability density function for long time, accurately and fast. The validation is performed over a cloud of high area-to-mass objects in Medium Earth Orbit (MEO), under the perturbing effects of solar radiation pressure, Earth's oblateness and luni-solar perturbation. The methodology is proven to be accurate and several order of magnitude faster than the integration of the full dynamics of the same points.

1.3 Scope of the thesis

In the re-entry predictions problem, uncertainties are the main source of inaccuracies, to such an extent that they heavily affect forecasts made few hours before the actual re-entry over the Earth's atmosphere. The intrinsic multidimensional nature of the uncertainties is particular demanding, in terms of modelling and also in terms of computational efforts. The main consequence is that several systems need to be modelled and connected, and all of them must be tested for an enormous number of variables. An exhaustive re-entry analysis requires thousands of simulations, to fulfil the re-entry statistics and proper probability density functions. Input variables are often only slightly adjusted, since intervals of variation are usually small. In fact, even minimal variations in the initial conditions, are characterised by completely different re-entry epochs and locations. Nevertheless, the simulation must be launched from the beginning, rapidly making the whole procedure extremely onerous. The standard Monte Carlo method represents a somehow brute-force approach to uncertainty propagation, as the required amount of simulations can lead to unreasonable computational times, especially when the number of uncertain variables is high (Minisci et al. [2017]).
A faster simulation would be a positive improvement, and increasing the number of simulations would guarantee a more accurate re-entry forecast. The re-entry problem severity is not going to diminish over the years, especially considering that the number of objects orbiting the Earth is continuously increasing. Therefore, a tool to increase the number of simulations while decreasing the computational time would be desirable and of great interest.
The aim of the thesis is to create a theoretical model, based on the propagation of initial state uncertainties, able to compete with the numerical Monte Carlo in terms of accuracy, while reducing the computational burden. The intermediary step consists of an analysis of the influencing parameters and the validation of the model itself.
More precisely, the main scope of the present thesis is to apply the differential algebra to re-entry predictions, in the presence of uncertainties on the initial state, using semi-analytical equations. Differential algebra has the impressive potential of speeding up the

re-entry campaign, while increasing the number of simulations completed. For the first time in literature, the differential algebra and the semi-analytical averaging technique are applied to the re-entry predictions problem. Another novel topic which is explored in the present thesis, is the application of the domain splitting procedure to the satellite re-entry in the Earth's atmosphere. Finally, global sensitivity indices are computed by differential algebra evaluations.

1.4 Methodological approach

The complete implementation of the thesis required multiple steps for the definition of the mathematical model, and its actual development and validation.
From the theoretical point of view, celestial mechanics texts have been helpful to build a background on the available models for the perturbing effects of the Earth's gravitational field and the atmospheric interaction. While the consultation of the available documentations regarding differential algebra, and semi-analytical methods has been fundamental.
In order to understand the basic principles of differential algebra and its implementation in the computer environment, the principal source has been the work done by Wittig [2015], who provided clear and detailed information concerning how to use the DACE 2.0 library, by means of examples and tutorial. After having acquired a first understanding about its basic principles, the next step has been the practical implementation of all the components of the model here presented.
Firstly, it has been necessary to code an ODE solver able to handle DA variables. The chosen integrator is the Dormand-Prince method, an explicit ODE solver of the Runge-Kutta family. The integrator has been firstly tested propagating the full dynamics, by means of the Gauss planetary equations, including the first order Earth gravitational perturbation, J_2, and the atmospheric drag, as provided by Vallado [2013]. In addition, a numerical Monte Carlo simulation environment has been created, since it is fundamental to study the validity region of the Taylor expansion generated in the DA framework, and the accuracy of the polynomial evaluations. Once the accuracy and the reliability of the self-coded integrator have been tested, the Gauss planetary equations in the right-hand side have been substituted with averaged equations. The drag contribution is expressed by means of King-Hele semi-analytical methods, while the Earth's oblateness perturbation is only considered through its long-term effect. The averaged mathematical formulation is a powerful tool to speed-up the integration while considering the secular perturbing effects. Since the King-Hele formulation requires a fixed scale height which decays strictly exponentially with altitude, firstly, a simple atmospheric density profile has been used,

given by a single exponential function. Nevertheless, a more complex model is necessary to guarantee the desired reliability of the results. In literature, several models exist, both static and dynamic. The main constraint influencing the choice of an atmospheric model is the differential algebra environment. It requires a continuous density profile, the non-satisfaction of this condition causes inaccuracies in the results obtained. The superimposed King-Hele method provided by Frey et al. [2019], not only constitutes an improvement compared with the classical KH formulation, but it also comprises a smooth atmospheric model, which also meets the DA requirement.
Finally, to efficiently apply the differential algebra and the semi-analytical methods to the re-entry problem, the constraint satisfaction and the domain splitting routines have been included in the model. The first allows to find the re-entry position and time for all the displaced points from the DA expansion of the reference state. The latter guarantees the propagation of large set of uncertainties, resulting in a final solution constituted by a set of polynomial expansions, each valid in a subdomain.
The model has been validated by means of an analysis for the initial state uncertainties and other influencing parameters, such as the DA order applied and the accepted tolerances. Moreover, the accuracy and the computational cost of the methodology is compared with the numerical Monte Carlo.
Concluding, the model has been applied to existing objects, which already re-entered the Earth's atmosphere, in order to show the potentiality of the method. The two chosen objects are the GOCE satellite, and the Chinese space station Tiangong-1. The results comprise the prediction of the probability density function of the re-entry time, the impact distribution over the Earth's surface, and a global sensitivity analysis.

1.5 Thesis outline

The present thesis tackles the re-entry problem, described in the differential algebra mathematical environment, and through the use of semi-analytical method for orbit propagation. The work is organised to provide the reader with the knowledge necessary to understand the methodology applied to study the re-entry predictions, its challenges and benefits.
Chapter 2 provides a detailed description of the theoretical environment. It outlines the basic fundamentals of the differential algebra, an introduction to the semi-analytic methods based on the King-Hele averaging procedure, the complete set of equations used, and some features of ODE solvers in general and of the coded integrator. Also, it provides a detailed description of the principles, the mathematical formulation and the actual implementation of the constraint satisfaction and the domain splitting techniques.

Chapter 3 consists in the analysis and validation of the mathematical methodology proposed to study the re-entry problem. The influence of the key parameters included within the model is discussed. The chapter provides the description of the influence of the different Keplerian elements, the role of the DA order to assure the convergence of the problem, and the order of magnitude of the displacements that can be applied. It also focuses on the computational time, and it shows the beneficial effect of the differential algebra, when thousands of simulations need to be completed. Moreover, it contains the analysis of how the domain splitting technique is applied to the re-entry problem and its main features in that contest. Finally, the effect of the uncertainties on different sets of variables is considered, including the flight path angle, the velocity magnitude and the azimuth.
Chapter 4 consists of a description of the results obtained applying the methodology to real re-entered objects, the GOCE satellite and the Chinese space station Tiangong-1. The DA-based methodology is compared with the traditional Monte Carlo method, in terms of PDFs, ground risk map, and computational time for the global sensitivity analysis.
Chapter 5 contains a final summary of the thesis, its intrinsic limitations and neglected aspects, and some remarks for future research efforts.

Chapter 2

Theoretical modelling

This chapter deals with the definition of the model created for the thesis work. The scope is to numerically model the satellite re-entry within the Earth's atmosphere due to the action of the drag, in the presence of uncertainties in the initial state. The numerical environment used is the differential algebra, which replaces all algebraic operations between numbers by ones that act on polynomials instead. The final state is therefore a Taylor series expansion, which can be evaluated in a displaced condition with respect to the reference one, a brief introduction about the differential algebra is given in Section 2.1. Section 2.2 contains an overview on the sets of coordinates used to represent the satellite state. The satellite dynamics is described in averaged terms, the time variations of the semi-major axis a and the eccentricity e are retrieved using semi-analytical methods, the technique was firstly introduced by King-Hele [1964]. The set of differential equations proposed in this thesis work, as well as the atmospheric density model used, are entirely developed by Frey et al. [2019]. The mathematical formulation of the satellite orbital trajectory is in Section 2.3. To propagate the initial uncertainty state an integrator is required. The one implemented for this thesis is a member of the Runge–Kutta family of ODE solvers, the Dormand-Prince method, which is presented in Section 2.4. In addition, two numerical techniques relying on the differential algebra are here described and included, the domain splitting and the constraint satisfaction. The domain splitting guarantees to preserve the accuracy of high order expansions while maintaining a good convergence, the procedure is described in Section 2.5. Finally, the constraint satisfaction is the core of this thesis work, it allows to retrieve the exact time instant and satellite state which characterises each displaced point when it encounters the Earth's atmosphere at the chosen re-entry altitude. Section 2.6 provides a detailed definition of the constraint satisfaction, describing how differential algebra can be applied to the re-entry problem.

2.1 Differential algebra

Differential Algebra (DA) was introduced for the first time by Ritt [1950]. It is a numerical technique based on the algebraic manipulation of polynomials. It allows to automatically compute high order Taylor expansions of functions, providing algorithms to manipulate these expansions. It is applied in several fields, as beam physics (Berz [1999]) and celestial mechanics (Di Lizia et al. [2008]). Moreover, the differential algebra supplies the mathematical tools required to compute the derivatives of functions within a computerised environment, substituting the classical implementation of real algebra with a new algebra constituted by Taylor polynomials. This means that DA technique can automatically generate the Taylor series of a sufficient regular function (Sun et al. [2018]), and manipulate them as with common floating numbers. In the present thesis, the DA library used (Massari et al. [2018]) provides for various methods for basic operations, but also for more complex algorithms, such as function composition, inversion or integration. A mathematical introduction to the differential algebra is given in Section 2.1.1 along with a simple illustrative example. Several DA methods are outlined in Section 2.1.2. Finally, Section 2.1.3 shows how DA can be introduced in ODE solvers.

2.1.1 Mathematical formulation

Consider a generic n-dimensional, sufficiently regular, nonlinear function

$$\mathbf{y} = \mathbf{f}(\mathbf{x}) \tag{2.1}$$

the DA environment is created by initialising the DA variable $[\mathbf{x}]$, which is the DA version of the independent variable $\mathbf{x}$ around its reference value $\bar{\mathbf{x}}$, by adding the perturbation $\delta\mathbf{x}$ to $\bar{\mathbf{x}}$, i.e

$$[\mathbf{x}] = \bar{\mathbf{x}} + \delta\mathbf{x} \tag{2.2}$$

which is already a Taylor expansion of $\mathbf{x}$ around the reference value $\bar{\mathbf{x}}$. The function $\mathbf{y}$ in the DA framework becomes

$$[\mathbf{y}] = \mathbf{f}([\mathbf{x}]) = P_{\mathbf{y}}^{k}(\delta\mathbf{x}) = \sum_{p_1+\ldots+p_n\leq k} \mathbf{c}_{p_1\ldots p_n} \cdot \delta x_1^{p_1} \ \ldots \ \delta x_n^{p_n} \tag{2.3}$$

where $P_{\mathbf{y}}^{k}$ is the k-th order Taylor expansion of the dependent variable $\mathbf{y}$ with respect to $\delta\mathbf{x}$, $p_1, \ldots, p_n$ are the orders of components $\delta x_1, \ \ldots \ , \delta x_n$, and $\mathbf{c}_{p_1\ldots p_n}$ are the Taylor coefficients of $P_{\mathbf{y}}^{k}$ (Sun et al. [2018]).
Similar to the computer representation of real numbers as Floating Point (FP) numbers,

DA allows the representation and manipulation of functions on a computer. A visual example of how DA works is provided in Figure 2.1. The expression $1/(x+1)$ is evaluated once in $C^r(0)$ (top) and then in DA with truncation order 3. Starting with the identity function x, by adding one the function $x+1$ is defined, the representation of which is fully accurate in DA as it is a polynomial of order 1. Continuing the evaluation, the multiplicative inversion is performed, resulting in the function $1/(x+1)$ in $C^r(0)$. As this function is not a polynomial anymore, it is automatically approximated in DA arithmetic by its truncated Taylor expansion around 0, given by $1\text{-}x+x^2\text{-}x^3$.

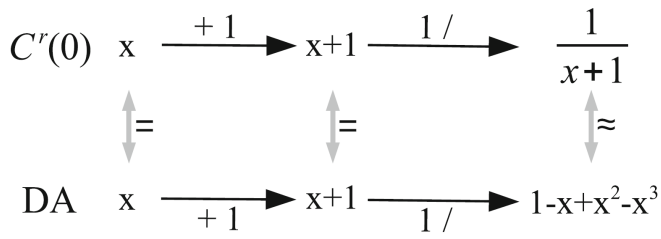

Figure 2.1: Evaluation of the expression $1/(1+x)$ in $C^r(0)$ and DA arithmetic. Source: Wittig et al. [2017].

As a final note, for all the variables in the thesis, being DA variables, the bracket notation has been omitted for the sake of clarity.
One simple example about how a DA expansion is able to approximate a real function is the circle, given by the *sine* and *cosine* functions, which are related by the well-known equation

$$\sin^2 x + \cos^2 x = 1 \tag{2.4}$$

Let x be the unitary DA variable around the reference state 0, it is possible to define the expansions of the sine and cosine functions. The two functions are evaluated with respect to x in the interval [$-\pi$, π]. The DA order k is the polynomial expansion order. As the order increases the accuracy of the polynomial improves as for a Taylor series.
Figure 2.2 represents the pairs of values in the 2D plane, to correctly reproduce the circle, a DA expansion of order 8 is needed.

2.1.2 Principal DA methods

The present thesis is completely relying on the differential algebra, which constitute the framework for every simulation, test and result here presented. In particular, the C++ library used is freely available in the open-source software DACE Core Engine 2.0 (DACE 2.0), created by Massari et al. [2018].

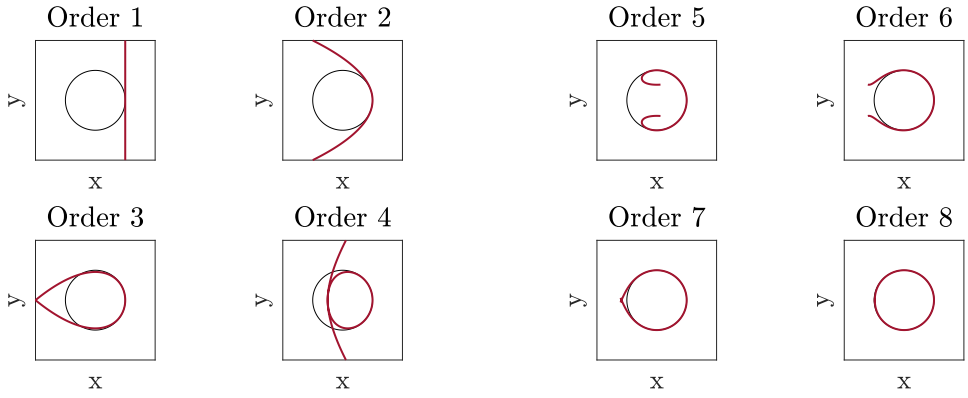

(a) From order 1 to 4

(b) From order 5 to 8

Figure 2.2: Circle representation with DA.

To familiarise with the DA environment, the consultation of the tutorials made available by Wittig [2015] has been extremely precious. They provide basic and advanced exercises to understand how the DA works, as well as its potentials and applications in the astrodynamics field.

Some functions and setting are particularly relevant for the present research project. Therefore, they are listed and briefly described below. For more details refer to the DACE 2.0 reference page in GitHub[1].

Set truncation epsilon

Due to the magnitude of the terms involved, it is of fundamental importance to set the truncation error, in order to efficiently run the propagation. The epsilon is set to zero throughout the project.

Modified Bessel functions of first kind

Semi-analytical equations require the modified Bessel function of first kind, and they need to be DA variables. The functions are available in the latest version of the DACE library. The function computes the n-th modified Bessel function of first type I_n, of a DA object.

Access to expansion coefficients

The function returns a specific coefficient of a DA object, by giving as input the vector of the exponent indices required.

Evaluation

The function returns the evaluation of a DA object with respect to a given vectors of variables.

[1]DACE Development Group, *DA Core Engine 2.0*: `https://github.com/dacelib/dace`.

Variable integration
The function computes the integral of a DA object with respect to a certain variable.

Variable inversion
The method gives the inverse of a set of DA polynomials $\Phi(\delta x)$, returning a new DA set. The new polynomials $x(\delta\Phi)$ are the expansion of the original DA variables as a function of the original set.

Variable translation
The method defines a transformation of the form $x = a\,x + c$, of a DA variable x, which is multiplied by the quantity a, and shifted by the quantity c.

Expansion norm estimation
The function estimates different types of order sorted norms for terms of a DA object, up to a specified order.

2.1.3 High order expansion of ODEs flow

The use of differential algebra provides great advantages when it is applied to the numerical integration of ODEs, as in the case of a satellite re-entry propagation. The following description is based on Wittig et al. [2014b]. Any arbitrary integration scheme requires a number of evaluations of the right hand side of the equation for each time step. If all the calculations are carried out in the DA framework, the final solution of the problem is a polynomial expansion around the initial state. Therefore, an evaluations of such polynomial gives the final solution for a variation in the initial condition without integrating again the equations. Consider the scalar Cauchy problem Equation (2.5) defined on $I \in [t_0, t_f]$ as

$$\begin{cases} \dfrac{\mathrm{d}x(t)}{\mathrm{d}t} = f(t, x(t)), & t \in I \\ x(t_0) = x_0, \end{cases} \tag{2.5}$$

Let $\Phi(t, \delta x_0)$ be the associated solution flow. It is possible to show that, starting from a DA representation of x_0, the flow polynomial can be propagated up to t_f. In fact, x_0 can be initialised as the DA identity function

$$x_0 = x_0 + \delta x_0 \tag{2.6}$$

Even if the DA truncation order is set to k, the initial state considers only the reference value x_0 and its first derivative. In particular, x_0 is equal to the flow evaluated at the initial time

$$x_0 = \Phi(t_0,0) \tag{2.7}$$

When, at each time step iteration j, the numerical scheme is evaluated in differential algebra, the solution

$$x_j = \Phi(t,0) \tag{2.8}$$

is the k-order polynomial expansion at time t_j around the initial condition x_0. The DA coefficients became less and less equal to zero as higher order terms are required to propagate the Taylor series during the integration. Finally, x_f gives the desired expansion at t_f. The key advantage of the differential algebra propagation is that the cost of a DA propagation is essentially constant. This is because the propagation of one condition, displaced from the central point of by δx_0, only requires a single polynomial evaluation, the cost of which is negligible compared to the integration. Therefore, the DA propagation shows a large initial cost of computing the polynomial expansion of the flow once, about two orders of magnitude higher than the cost of a single point-wise propagation, depending on the order k. However, once the polynomial is computed, there is practically no additional cost for the propagation of virtually any number of points (Wittig et al. [2017]).

2.2 Orbital mechanics fundamentals

There are several ways to describe the state of an orbiting satellite around a central body. This section provides few insights about the reference frame and coordinates that are used throughout the thesis. For a detailed description refer to Vallado [2013].

2.2.1 Orbital elements

The motion of a point object in space is governed by Newton's Law of gravitation, and the state of its centre of gravity is completely defined by 6 degrees of freedom. Besides Cartesian coordinates, a common representation of the state is given through the orbital elements, as reported in Curtis [2014] and Vallado [2013]. The complete set is defined as $\{a, e, i, \omega, \Omega, \nu\}$ where a is the semi-major axis, e the eccentricity, i the inclination, ω the argument of perigee, Ω the right ascension of the ascending node and ν the true anomaly. Figure 2.3 shows how the elements define the orbit position with respect to the Earth Equatorial plane.

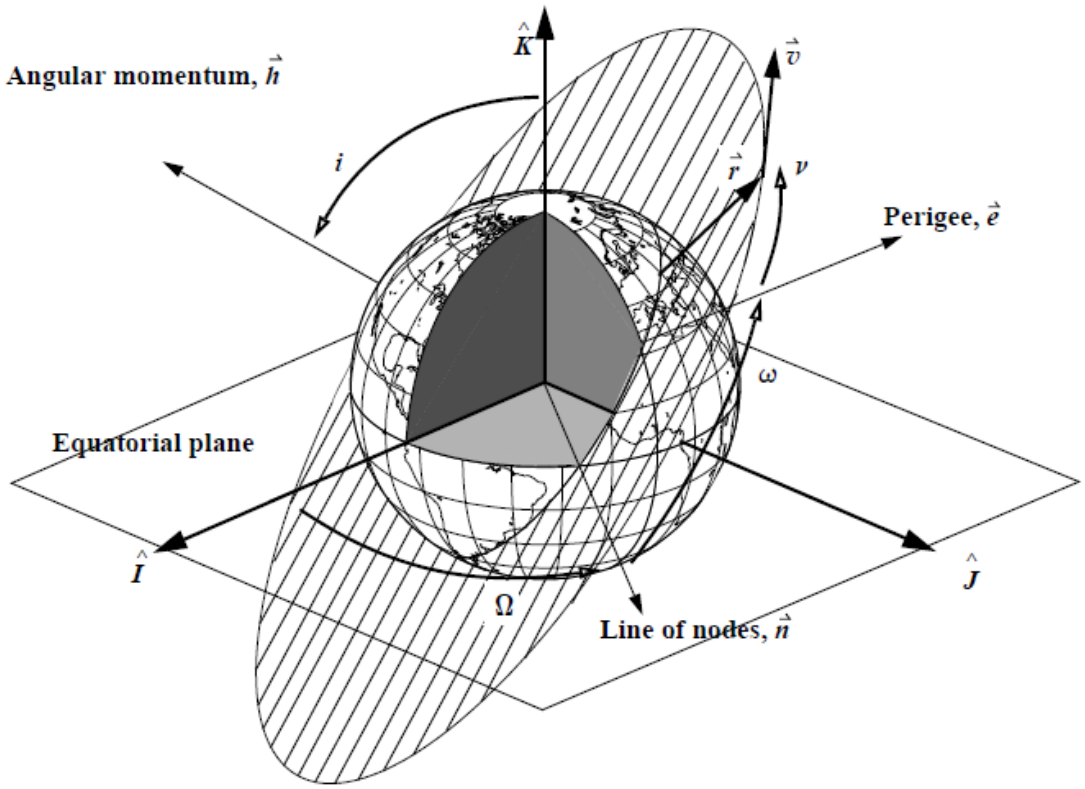

Figure 2.3: Definition of a single point orbit through orbital elements. Source: Vallado [2013].

The distance between the centre of the Earth and the object can be retrieved through equation Equation (2.9), and it can be used to compute the actual altitude h by subtracting the mean Earth's radius $R_E = 6378$ km as in Equation (2.10).

$$r = \frac{a(1-e^2)}{1+e\,\cos\nu} \tag{2.9}$$

$$h = r - R_E \tag{2.10}$$

The true anomaly ν varies along the orbit between $[0, 2\pi]$ during one revolution. In fact the mean motion $n = \sqrt{\mu/a^3}$ connects the time passed from a perigee passage $t - t_0$, with the variation of the mean anomaly $M - M_0$, as in equation Equation (2.11). Finally, the relations Equation (2.12) and Equation (2.13) define the true anomaly as a function of

the mean anomaly and the eccentric anomaly E, respectively.

$$M = M_0 + n(t - t_0) \tag{2.11}$$

$$\tan\frac{\nu}{2} = \sqrt{\frac{1+e}{1-e}}\tan\frac{E}{2} \tag{2.12}$$

$$M = E - e\sin E \tag{2.13}$$

2.2.2 Flight elements

Although being the most common state vector definition, orbital elements are not the only possible representation. Flight elements are a widespread choice in the field of objects re-entry, since the equation governing this phase can be expressed using these variables, as in Rasotto et al. [2016]. The set definition varies, as different reference frames can be chosen to determine the velocity angles, here is presented the theory illustrated in Vallado [2013].

The complete set is defined as $\{\alpha, \delta, \phi_{fpa}, \beta, r, v\}$. In particular, α and δ are the position right ascension and declination angles derived in the Earth-Centred Inertial (ECI) reference frame, as it is illustrated in Figure 2.4. ϕ_{fpa} and β are the flight path angle and azimuth angle describing the orientation of the velocity vector in the Topocentric Horizon Coordinate System (SEZ). SEZ coordinates are obtained following a double rotation using α and δ. The resulting fundamental plane lies on the local horizon, while the vertical axis points radially outward from the site. Finally, r and v are the position and velocity magnitudes.

The interpretation of the flight path angle is rather important when it is observed in the orbital plane, as is is shown in Figure 2.5. In fact, its value defines the angle between the velocity vector and the line orthogonal to the radius. The complementary angle ϕ_{fpav} is also sometimes referred in the literature. ϕ_{fpa} value is 0° only at the orbit perigee, apogee and for circular orbits, while it increases for high eccentricity orbits.

The formulas to move from the Cartesian elements to the flight elements are taken from Vallado [2013]. In particular, I, J, K represent the directions of the ECI reference system. The right ascension α is defined as

$$\sin\alpha = \frac{r_J}{\sqrt{r_I^2 + r_J^2}} \qquad\qquad \cos\alpha = \frac{r_I}{\sqrt{r_I^2 + r_J^2}} \tag{2.14}$$

while the declination δ is calculated by

$$\sin\delta = \frac{r_K}{r} \qquad\qquad \cos\delta = \frac{\sqrt{r_I^2 + r_J^2}}{r} \tag{2.15}$$

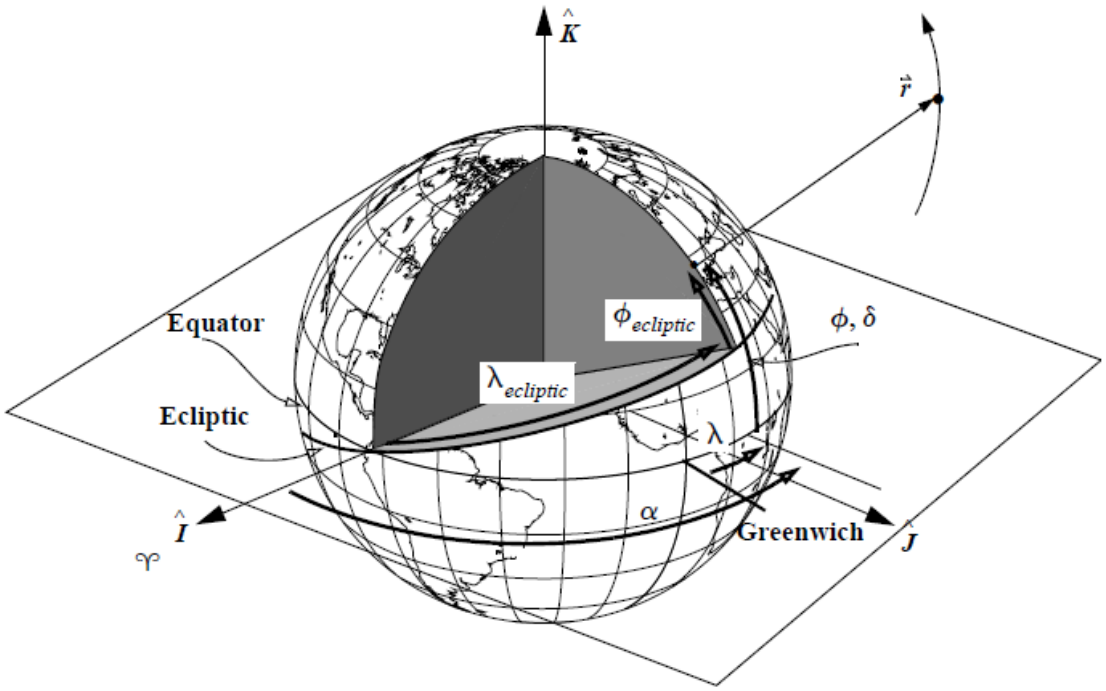

Figure 2.4: Right ascension and declination in the ECI reference frame. Source: Vallado [2013].

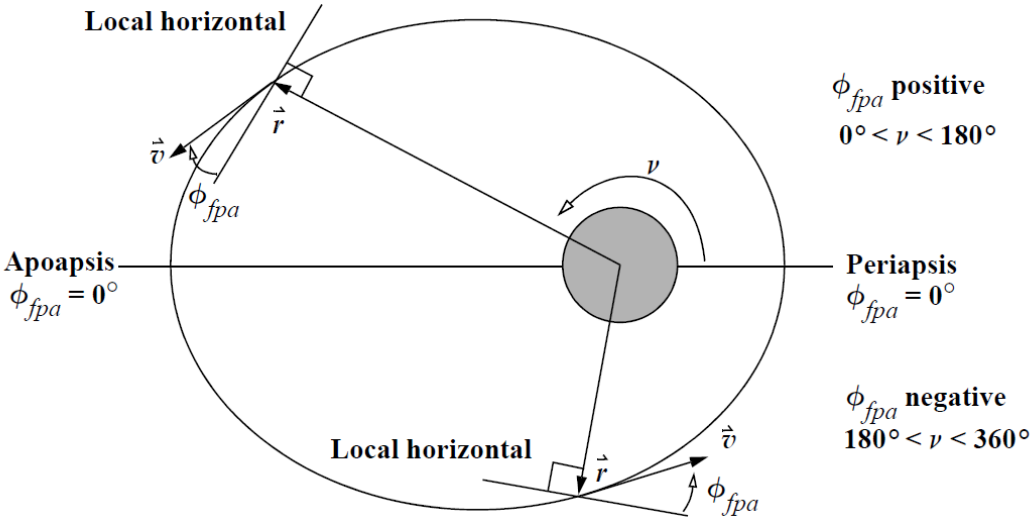

Figure 2.5: Definition of the flight path angle. Source: Vallado [2013].

The module of the position and the velocity are

$$r = \sqrt{r_I^2 + r_J^2 + r_K^2} \qquad\qquad v = \sqrt{v_I^2 + v_J^2 + v_K^2} \tag{2.16}$$

The rotation from the ECI reference frame to the SEZ system is given as

$$\left[\frac{SEZ}{ECI}\right] = R_2(90° - \delta)\, R_3(\alpha) = \begin{bmatrix} \cos\alpha\,\sin\delta & \sin\alpha\,\sin\delta & -\cos\delta \\ -\sin\alpha & \cos\alpha & 0 \\ \cos\delta\,\cos\alpha & \sin\alpha\,\cos\delta & \sin\delta \end{bmatrix} \tag{2.17}$$

$$\boldsymbol{v}_{SEZ} = \left[\frac{SEZ}{ECI}\right] \boldsymbol{v} \tag{2.18}$$

Once the velocity vector is in the proper reference frame, with components v_S, v_E, and v_Z, the flight path angle ϕ_{fpa} is

$$\sin\phi_{fpa} = \frac{\sqrt{v_S^2 + v_E^2}}{v} \qquad\qquad \cos\phi_{fpa} = \frac{v_Z}{v} \tag{2.19}$$

Finally, the azimuth β is equal to

$$\sin\beta = \frac{v_E}{\sqrt{v_S^2 + v_E^2}} \qquad\qquad \cos\beta = \frac{-v_S}{\sqrt{v_S^2 + v_E^2}} \tag{2.20}$$

2.2.3 Satellite Coordinate System

To study the spacecraft motion around the Earth, it is sometimes useful to express the Cartesian coordinates in a frame attached to the satellite and rotating along the orbit. The literature presents two main possibilities called Gaussian coordinate systems, which are shown in Figure 2.6. The fundamental plane of these frames lies in the orbital plane, while the third axis W is perpendicular to the position and velocity vectors. In particular, in the RSW system, the first axis R is directed as the position vector, and the along-track axis S is orthogonal to it. The velocity vector is aligned with the S axis only at apogee, perigee and in circular orbits. Differently, in the NTW reference frame, the T, in-track, axis is tangential to the satellite path, as it always points to the velocity vector, while the N axis is normal to it. The Cartesian coordinates can be expressed in both frames, starting from the perifocal reference frame, through additional counterclockwise rotations of ν and ν-ϕ_{fpa}, for RSW and NTW, respectively. These coordinates are mainly used to describe the satellite position from a sensor site and to express orbital errors.

2.3 Physical model

Within the present research project, the satellite dynamics is represented in orbital elements. The equations describing the satellite re-entry are written in an averaged form.

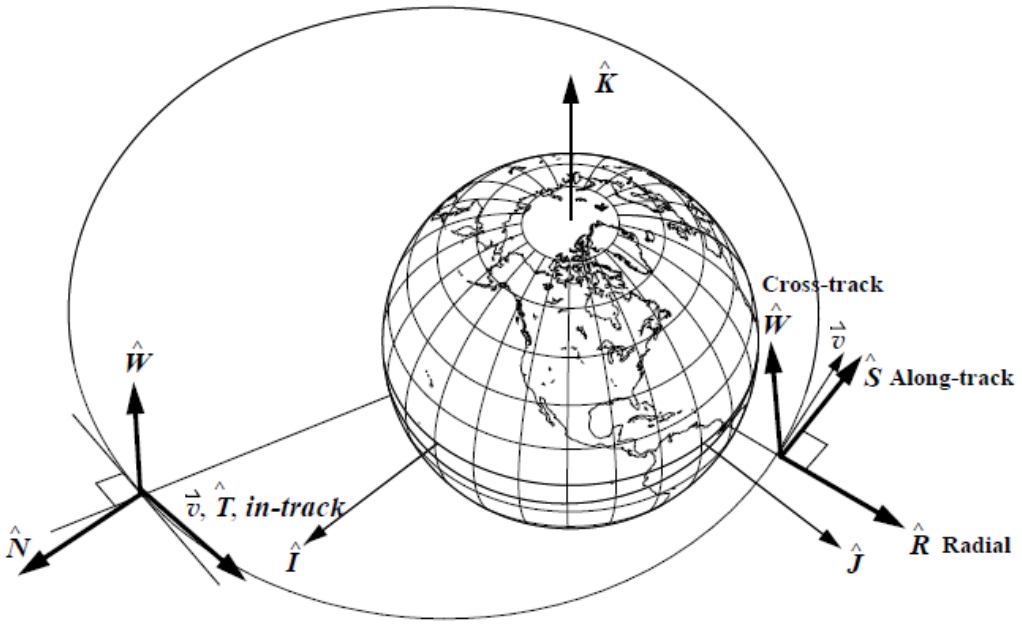

Figure 2.6: Satellite Coordinate System, RSW and NTW. Source: Vallado [2013].

Numerical integration of orbital trajectory of a large number of initial conditions is computationally expensive, therefore, averaged techniques allow to reduce the computational burden. Satellites re-entry is mostly caused by the action of atmospheric drag, which shrinks the orbit by reducing the semi-major axis a and the eccentricity e. Semi-analytical methods are used to approximate the time variation of a and e. The semi-analytic formulation requires a specific form of the atmospheric density model. The density profile used is static, and is completely based on the research done by Frey et al. [2019]. Also the version of the semi-analytical equations implemented in the methodology here described have been developed by the same authors. The inclination i is not affected either by the drag or by secular effects. While the derivatives of the right ascension of the ascending node Ω, the argument of perigee ω, and the mean anomaly M, comprise only secular variations due to the Earth's oblateness.

Section 2.3.1 introduces semi-analytical methods and how the orbit contractions are derived. The atmospheric model used is discussed in Section 2.3.2, and the semi-analytical equations are presented in Section 2.3.3. The secular gravitational effects are analysed in Section 2.3.4. Finally, a summary of the physical model used is in Section 2.3.5.

2.3.1 Semi-analytical methods

Numerical integration of the full orbital dynamics, including short-periodic variations, can be demanding from a computational point of view. For this reason, semi-analytical methods were developed to perform this task more quickly. Such methods remove the short-term periodic effects by averaging the variational equations, thereby reducing the stiffness of the problem. This is especially desired when orbits are to be integrated for many initial conditions, as it occurs in the case of uncertainty propagation of the initial state during the re-entry phase.

Atmospheric drag causes the contraction of the satellite orbit around the Earth. In the specific, it causes the orbit to circularise. Therefore, the eccentricity e reduces, and friction acts on the semi-major axis a, diminishing it until the full re-entry occurs. King-Hele [1964], in the '60s, derived an analytical approximation of the integrals of a and e under the action of the atmospheric drag. Depending on the orbit eccentricity, different series expansions were derived. Further research efforts done by Vinh et al. [1979] improved the theory by removing the ambiguity arising from the regions of validity in eccentricity, and applying more rigorous Poincaré method for the integration. The dynamical system is based on Lagrange's planetary equations, given in Keplerian elements. Only the tangential force f_T induced by the aerodynamic drag is considered

$$f_T = -\frac{1}{2}\,\rho\, v^2\, \delta_r \tag{2.21}$$

where ρ is the density, v the inertial velocity, and δ_r the effective area-to-mass ratio. The time variations of the semi-major axis a, the eccentricity e, and the eccentric anomaly E, are

$$\frac{\mathrm{d}a}{\mathrm{d}t} = -\frac{a^2\,\rho\,\delta_r\,v^3}{\mu} \tag{2.22a}$$

$$\frac{\mathrm{d}e}{\mathrm{d}t} = \frac{a\,\rho\,\delta_r\,v}{r}\,(1-e^2)\,\cos E \tag{2.22b}$$

$$\frac{\mathrm{d}E}{\mathrm{d}t} = \frac{1}{r}\left(\frac{\mu}{a}\right)^{\frac{1}{2}} \tag{2.22c}$$

with Earth's gravitational parameter μ, the radius r and v given by

$$r = a(1 - e\cos E) \tag{2.23a}$$

$$v = \sqrt{2\,\frac{\mu}{r} - \frac{\mu}{a}} \tag{2.23b}$$

Equation (2.22) is averaged over a full orbit revolution, under the assumption that a and e remain constant. This reduces the stiffness of the problem. The resulting contractions,

$\Delta\, a$ and $\Delta\, e$ are (Frey et al. [2019])

$$\Delta\, a = -a^2\, \delta_r \int_0^{2\pi} \rho(h) \frac{(1 + e\, \cos E)^{\frac{3}{2}}}{(1 - e\, \cos E)^{\frac{1}{2}}}\, \mathrm{d}E \tag{2.24a}$$

$$\Delta\, e = -a\, \delta_r \int_0^{2\pi} \rho(h) \left(\frac{1 + e\, \cos E}{1 - e\, \cos E}\right)^{\frac{1}{2}} \cos E\, (1 - e^2)\, \mathrm{d}E \tag{2.24b}$$

For the semi-analytical propagation of the orbit, the derivatives of the variables with respect to time are approximated by the change over one revolution divided by the time required to cover the revolution

$$F_x = \frac{\mathrm{d}x}{\mathrm{d}t} \approx \frac{\Delta\, x}{P} \qquad x \in [a,\, e] \tag{2.25}$$

where P is the orbital period defined as

$$P = 2\pi \sqrt{\frac{a^3}{\mu}} \tag{2.26}$$

A brief summary of the formulation is given by Frey et al. [2019], although, the exhaustive theory behind the KH approximation can be found in King-Hele [1964].

The integrals in Equation (2.24) can be approximated analytically by expanding the integrands as a power series in e for low eccentric orbits, and in the inverted auxiliary variable c

$$\frac{1}{c} = \frac{H}{a\, e} \tag{2.27}$$

for highly eccentric orbits. The power series are cut off at the appropriate degree.

With the assumption that the density ρ decreases exponentially with altitude, each expanded integrand can be represented by the modified Bessel function of first kind I_n, which, for $n \in \mathbb{N}_0$, is given as (Abramowitz and Stegun [1972])

$$I_n(x) = \frac{1}{\pi} \int_0^{\pi} \exp\{(x \cos\theta) \cos(n\, \theta)\}\, \mathrm{d}\theta \tag{2.28}$$

where θ is the true anomaly of the orbit.

The modified Bessel functions of first and second kind are the solution of the differential equation (Abramowitz and Stegun [1972])

$$x^2 \frac{\mathrm{d}^2 y}{\mathrm{d}x^2} + x\, \frac{\mathrm{d}y}{\mathrm{d}x} - (x^2 + n^2)\, y = 0 \tag{2.29}$$

For a real number α, the modified Bessel function of first kind can be computed using (Abramowitz and Stegun [1972])

$$I_\alpha(x) = \left(\frac{1}{2} x\right)^{\alpha} \sum_{k=0}^{\infty} \frac{\left(\frac{1}{4} x^2\right)^k}{k! \Gamma(\alpha + k + 1)} \tag{2.30}$$

where $\Gamma(x)$ is the Gamma function, provided in Equation (2.31) (Abramowitz and Stegun [1972]), defined as an extension of the factorial to complex and real number arguments.

$$\Gamma(x) = \int_0^\infty t^{x-1} \exp\{-t\} \, \mathrm{d}t \tag{2.31}$$

The mathematical formulation of the re-entry problem addressed in the present work is based on averaging techniques, but the equations used are taken from the work done by Frey et al. [2019], that further refined the King-Hele method by deriving higher order terms during the series expansion. The authors also introduced a variable boundary condition to choose the approximate eccentricity regime, based on the series truncation errors. Compared with the original King-Hele version, the major innovative element consists in the newly proposed atmospheric density model. King-Hele Semi-Analytical (SA) equations are derived based on an exponential form of the atmospheric density, as provided in Equation (2.32).

$$\rho(h) = \hat{\rho} \exp\{-h/H\} \tag{2.32}$$

where $\hat{\rho}$ is the reference density and H the (fixed) scale height.
During the SA propagation of an object trajectory subjected to air-drag forces, the change in the orbital element space is considered over a full revolution. This requires the integration of the density along the orbit. The advantage of semi-analytical methods resides on the fact that the average contraction can be computed analytically using only a single density evaluation at the perigee.

2.3.2 Atmospheric model

The analytical KH contraction method relies on the assumption that the atmosphere density decays strictly exponentially with the altitude. The actual Earth's density profile is not suitable to be approximated by a model characterised by a fixed scale height, due to its intrinsic complexity. In this condition, the KH method introduces potentially large errors for non-circular orbit configurations, which lead to an overestimation of the lifetime, especially for highly eccentric orbits. The method proposed by Frey et al. [2019], constitutes an improvement compared with the previous formulations, since it is not relying on the assumption of a fixed scale height. The new formulation consists in superimposing exponentially decaying partial atmospheres, each with a fixed scale height. This allows the King-Hele method to be applied in the presence of more complex density profiles. The KH formulation is then used for the calculation of the contraction of each individual component. Finally, each individual contribution is summed up, resulting in the global contraction of the overall not strictly exponentially decaying atmosphere density.
Moreover, the new density atmosphere, perfectly fits the requirements to use a DA environment. In fact, since the DA uses Taylor expansions, a continuous model for the

atmospheric density is required, otherwise discontinuities would cause the propagation to diverge in the regions where the discontinuities are crossed.
Table 2.1 provides the partial scale heights H_p and the partial reference densities $\hat{\rho}_p$ of the eight partial atmospheres, for three different values for the exospheric temperature T_∞. The smooth exponential atmosphere model, ρ_S, is obtained by superimposing exponential functions as

$$\rho_s(h) = \sum_{p=1}^{n_p} \rho_p(h) = \sum_{p=1}^{n_p} \hat{\rho}_p \, \exp\{-h/H_p\} \tag{2.33}$$

Where h is the altitude, $\hat{\rho}_p$ are the partial densities, H_p are the partial scale heights, and n_p is the number of partial atmospheres. The density model is static and derived by Frey et al. [2019], based on a fit of the Jacchia-77 model (Jacchia [1977]). In the cited model, the temperature and density profiles are a function of the exospheric temperature T_∞. The superimposed scale height, H_S, is

$$H_S(h) = \frac{\sum_{p=1}^{n_p} \rho_p(h)}{\sum_{p=1}^{n_p} \rho_p(h)/H_p} \tag{2.34}$$

The derivative of H_S with respect to h is monotonically increasing, as H_p is enforced to be larger than 0 for all p. Hence, the smooth atmosphere model can only be fitted to atmosphere models in altitude ranges where $\frac{\mathrm{d}H}{\mathrm{d}h} > 0$. The model in Equation (2.33) is fitted to the Jacchia-77 model for three different T_∞: in accordance to a low solar activity, $T_\infty = 750$ K; mean solar activity, $T_\infty = 1000$ K; and high solar activity, $T_\infty = 1250$ K. The fit is performed in the logarithmic space to avoid neglecting lower densities at higher altitudes, using least squares minimisation at heights between $h_0 = 100$ km and the upper boundary, $h_1 = 2500$ km.

Table 2.1: Smooth atmosphere model parameters resulting from a fit to the Jacchia-77 model, valid for altitudes $h \in [100; 2500]$ km. Source: Frey et al. [2019].

	$T_{\text{inf}} = 750$ K		$T_{\text{inf}} = 1000$ K		$T_{\text{inf}} = 1250$ K	
ρ	H_p [km]	$\hat{\rho}_p$ [kg/m^3]	H_p [km]	$\hat{\rho}_p$ [kg/m^3]	H_p [km]	$\hat{\rho}_p$ [kg/m^3]
1	4.9948	$2.4955e+02$	4.9363	$3.1632e+02$	4.9027	$3.6396e+02$
2	10.471	$8.4647e-04$	11.046	$5.2697e-04$	11.437	$3.8184e-04$
3	21.613	$9.1882e-07$	24.850	$3.7354e-07$	25.567	$2.8928e-07$
4	37.805	$1.2530e-08$	46.462	$1.0839e-08$	44.916	$1.2459e-08$
5	49.967	$1.3746e-09$	64.435	$1.0880e-09$	76.080	$9.2530e-10$
6	174.23	$1.5930e-13$	147.46	$3.8122e-13$	111.09	$1.6667e-11$
7	315.15	$1.1290e-14$	314.53	$4.8431e-14$	354.23	$5.9225e-14$
8	1318.1	$3.8065e-16$	1214.6	$4.2334e-16$	892.19	$1.7378e-15$

2.3.3 Semi-analytical equations

In this section SA equations are described. The extension of the KH contraction formulation into the superimposed King-Hele (SI-KH) version, proposed by Frey et al. [2019], is done by replacing ρ from Equation (2.32) with the one defined in Equation (2.33), the procedure leads to

$$\Delta\, a = \sum_{p=1}^{n_p} \Delta\, a_p = -a^2\, \delta_r \sum_{p=1}^{n_p} \int_0^{2\pi} \rho_p(h) \frac{(1 + e\, \cos E)^{\frac{3}{2}}}{(1 - e\, \cos E)^{\frac{1}{2}}}\, \mathrm{d}E \tag{2.35a}$$

$$\Delta\, e = \sum_{p=1}^{n_p} \Delta\, e_p = -a\, \delta_r \sum_{p=1}^{n_p} \int_0^{2\pi} \rho_p(h) \left(\frac{1 + e\, \cos E}{1 - e\, \cos E}\right)^{\frac{1}{2}} \cos E\, (1 - e^2)\, \mathrm{d}E \tag{2.35b}$$

Each partial contraction p reduces to the classical KH formulation with the partial exponential atmosphere ρ_p. The important difference is that now H_p is constant over the whole altitude range.
The rate of change is expressed as (Frey et al. [2019])

$$F_x = \frac{\mathrm{d}x}{\mathrm{d}t} = \sum_{p=1}^{n_p} (F_x)_p \approx \frac{1}{P} \sum_{p=1}^{n_p} \Delta\, x_p \qquad x \in [a,\, e] \tag{2.36}$$

In order to better visualise the final sets of equations, from now on it has been avoided to consider the summation performed over all the n_p components of the density vector. There are two different sets of semi-analytical equations for a and e, depending on the value of the eccentricity e. The boundary condition e_b is the value used as reference to distinguish between the two sets of equations, for low eccentric orbits ($e < e_b$) and highly eccentric orbits ($e > e_b$). It is defined as

$$e_b = \frac{1}{2} \left[-y + \sqrt{y^2 + 4\, y}\right] \tag{2.37}$$

where

$$y = \frac{H_e}{h_p + R_E} \quad \text{and} \quad H_e = -\frac{\rho_s}{\mathrm{d}\rho_s / \mathrm{d}h} \tag{2.38}$$

e_b formula is based on the truncation errors found in the formulations for the low and high eccentric orbits. The series truncation errors for the low eccentric orbit approximation (equations set valid when $e < e_b$), using the order notation $\mathcal{O}$, are of the order of (Frey et al. [2019])

$$\mathcal{O}_a^{low}(e^6) = a^2 \rho\, \exp\{(-c)\} I_0\, e^6 \approx a^2 \rho \frac{e^6}{\sqrt{c}} \tag{2.39a}$$

$$\mathcal{O}_e^{low}(e^6) = a \rho\, \exp\{(-c)\} I_1\, e^6 \approx a \rho \frac{e^6}{\sqrt{c}} \tag{2.39b}$$

The approximated version is only valid when the auxiliary variable c is large. For the high eccentric orbit approximation (equations set valid when $e > e_b$), the truncation errors are in the order of

$$\mathcal{O}_a^{high}\left(\frac{1}{c^6}\right) = a^2\rho\frac{1}{\sqrt{c}}\frac{(1+e)^{\frac{3}{2}}}{(1-e)^{\frac{1}{2}}}\frac{1}{c^6(1-e^2)^6} \approx a^2\rho\frac{1}{\sqrt{c}}\frac{1}{c^6} \tag{2.40a}$$

$$\mathcal{O}_e^{high}\left(\frac{1}{c^6}\right) = a\rho\frac{1}{\sqrt{c}}\left(\frac{1+e}{1-e}\right)^{\frac{1}{2}}\frac{1}{c^6(1-e^2)^6} \approx a\rho\frac{1}{\sqrt{c}}\frac{1}{c^6} \tag{2.40b}$$

Assuming the term $1/c^6$ dominates over the other terms including the eccentricity e. The assumption are proven to be valid by Frey et al. [2019].
The analytical formulas describe, for different eccentricities, the change in the semi-major axis a, and the eccentricity e, over one orbit. The rate of change of a and e are

$$F_a = \frac{\mathrm{d}a}{\mathrm{d}t} \approx \frac{\Delta a}{P} \tag{2.41a}$$

$$F_e = \frac{\mathrm{d}e}{\mathrm{d}t} \approx \frac{\Delta e}{P} \tag{2.41b}$$

where P is the period.
The functions k_a and k_e are used in the final formulation, and defined as (Frey et al. [2019])

$$k_a = \delta_r\sqrt{\mu\, a}\,\rho(h_p) \tag{2.42a}$$

$$k_e = \frac{k_a}{a} \tag{2.42b}$$

where $\delta_r = \frac{A}{m}C_d$ is the effective area-to-mass ratio, given by the product between the ratio of the cross-sectional area A and the mass m, and the drag coefficient C_d. μ is the gravitational parameter, and ρ is the atmospheric density evaluated at the perigee altitude, h_p.

Low Eccentric Orbit

For small $e < e_b(a,\, H)$ a series expansion in e is performed and then integrated using the modified Bessel functions for the first kind, $I_n(c)$, as (Frey et al. [2019])

$$\mathbf{e}^T = \begin{pmatrix} 1 & e & e^2 & e^3 & e^4 & e^5 \end{pmatrix} \tag{2.43}$$

$$\mathbf{I}^T = \begin{pmatrix} I_0 & I_1 & I_2 & I_3 & I_4 & I_5 & I_6 \end{pmatrix} \tag{2.44}$$

$$\Delta a = -2\,\pi\,\delta_r\rho(h_p)\,\exp\{(-c)\}\,a^2\,\left[\mathbf{e}^T\,\mathbf{K}_a^l\,\mathbf{I} + \mathcal{O}(e^6)\right] \tag{2.45a}$$

$$\Delta e = -2\,\pi\,\delta_r\rho(h_p)\,\exp\{(-c)\}\,a\,\left[\mathbf{e}^T\,\mathbf{K}_e^l\,\mathbf{I} + \mathcal{O}(e^6)\right] \tag{2.45b}$$

$\mathcal{O}(e^6)$ is the truncation error of the series of e, c is the auxiliary variable, $c = \frac{a\,e}{H}$, H is the scale height, h_p a single evaluation of the density at the perigee height. The constant matrices are given as (Frey et al. [2019])

$$\mathbf{K}_a^l = \begin{bmatrix} 1 & 0 & 0 & 0 & 0 & 0 & 0 \\ 0 & 2 & 0 & 0 & 0 & 0 & 0 \\ \frac{3}{4} & 0 & \frac{3}{4} & 0 & 0 & 0 & 0 \\ 0 & \frac{3}{4} & 0 & \frac{1}{4} & 0 & 0 & 0 \\ \frac{21}{64} & 0 & \frac{28}{64} & 0 & \frac{7}{64} & 0 & 0 \\ 0 & \frac{30}{64} & 0 & \frac{15}{64} & 0 & \frac{3}{64} & 0 \end{bmatrix} \tag{2.46}$$

$$\mathbf{K}_e^l = \begin{bmatrix} 0 & 1 & 0 & 0 & 0 & 0 & 0 \\ \frac{1}{2} & 0 & \frac{1}{2} & 0 & 0 & 0 & 0 \\ 0 & -\frac{5}{8} & 0 & \frac{1}{8} & 0 & 0 & 0 \\ -\frac{5}{16} & 0 & -\frac{4}{16} & 0 & \frac{1}{16} & 0 & 0 \\ 0 & -\frac{18}{128} & 0 & -\frac{1}{128} & 0 & \frac{3}{128} & 0 \\ -\frac{18}{256} & 0 & -\frac{19}{256} & 0 & \frac{2}{256} & 0 & \frac{3}{256} \end{bmatrix} \tag{2.47}$$

The rates of change of a and e for low eccentric orbits are obtained as

$$F_a = \frac{\mathrm{d}a}{\mathrm{d}t} = -k_a \, \exp\{(-c)\} \, \left[\mathbf{e}^T \, \mathbf{K}_a^l \, \mathbf{I} + \mathcal{O}(e^6)\right] \tag{2.48a}$$

$$F_e = \frac{\mathrm{d}e}{\mathrm{d}t} = -k_e \, \exp\{(-c)\} \, \left[\mathbf{e}^T \, \mathbf{K}_e^l \, \mathbf{I} + \mathcal{O}(e^6)\right] \tag{2.48b}$$

High Eccentric Orbit

The series expansion of e is infeasible for large values of $e > e_b(a, H)$. Therefore, the expansion is performed for a substitute variable $\lambda^2/c = 1 - \cos E$. The contractions over one orbit period are (Frey et al. [2019])

$$\mathbf{r}^T = \begin{pmatrix} 1 & \frac{1}{c\,(1-e^2)} & \frac{1}{c^2\,(1-e^2)^2} & \frac{1}{c^3\,(1-e^2)^3} & \frac{1}{c^4\,(1-e^2)^4} & \frac{1}{c^5\,(1-e^2)^5} \end{pmatrix} \tag{2.49}$$

$$\mathbf{e}^T = \begin{pmatrix} 1 & e & e^2 & e^3 & e^4 & e^5 & e^6 & e^7 & e^8 & e^9 & e^{10} \end{pmatrix} \tag{2.50}$$

$$\Delta a = -2\,\delta_r \sqrt{\frac{2\,\pi}{c}} \rho(h_p)\, a^2 \, \frac{(1+e)^{\frac{3}{2}}}{(1-e)^{\frac{1}{2}}} \, \left[\mathbf{r}^T \, \mathbf{K}_a^h \, \mathbf{e} + \mathcal{O}\left(\frac{1}{c^6}\right)\right] \tag{2.51a}$$

$$\Delta e = -2\,\delta_r \sqrt{\frac{2\,\pi}{c}} \rho(h_p)\, a \sqrt{\frac{1+e}{1-e}} \, (1-e^2) \, \left[\mathbf{r}^T \, \mathbf{K}_e^h \, \mathbf{e} + \mathcal{O}\left(\frac{1}{c^6}\right)\right] \tag{2.51b}$$

with the constant matrices (Frey et al. [2019])

$$\mathbf{K}_a^h = \begin{bmatrix} \frac{1}{2} & \frac{1}{16} & \frac{9}{256} & \frac{75}{2048} & \frac{3675}{65536} & \frac{59535}{524288} \\ 0 & -\frac{1}{2} & -\frac{3}{16} & -\frac{45}{256} & -\frac{525}{2048} & -\frac{33075}{65536} \\ 0 & \frac{3}{16} & \frac{75}{128} & \frac{675}{2048} & \frac{5985}{16384} & \frac{288225}{524288} \\ 0 & 0 & \frac{3}{16} & -\frac{75}{128} & -\frac{105}{2048} & \frac{10395}{16384} \\ 0 & 0 & -\frac{15}{256} & -\frac{3735}{2048} & \frac{21945}{32768} & -\frac{344925}{262144} \\ 0 & 0 & 0 & -\frac{45}{256} & \frac{13545}{2048} & -\frac{129465}{32768} \\ 0 & 0 & 0 & \frac{105}{2048} & \frac{110985}{16384} & -\frac{7687575}{262144} \\ 0 & 0 & 0 & 0 & \frac{525}{2048} & -\frac{836325}{16384} \\ 0 & 0 & 0 & 0 & -\frac{4725}{65536} & -\frac{16288965}{524288} \\ 0 & 0 & 0 & 0 & 0 & -\frac{33075}{65536} \\ 0 & 0 & 0 & 0 & 0 & \frac{72765}{524288} \end{bmatrix} \tag{2.52}$$

$$\mathbf{K}_e^h = \begin{bmatrix} \frac{1}{2} & -\frac{3}{16} & -\frac{15}{256} & -\frac{105}{2048} & -\frac{4725}{65536} & -\frac{72765}{524288} \\ 0 & -\frac{1}{4} & \frac{9}{32} & \frac{75}{512} & \frac{735}{4096} & \frac{42525}{131072} \\ 0 & \frac{3}{16} & \frac{39}{128} & -\frac{405}{2048} & \frac{525}{16384} & \frac{152145}{524288} \\ 0 & 0 & \frac{3}{32} & -\frac{375}{256} & \frac{735}{4096} & -\frac{31185}{32768} \\ 0 & 0 & -\frac{15}{256} & -\frac{1515}{2048} & \frac{123585}{32768} & -\frac{530145}{262144} \\ 0 & 0 & 0 & -\frac{45}{512} & \frac{31605}{4096} & -\frac{1165185}{65536} \\ 0 & 0 & 0 & \frac{105}{2048} & \frac{40845}{16384} & -\frac{10235295}{262144} \\ 0 & 0 & 0 & 0 & \frac{525}{4096} & -\frac{1505385}{32768} \\ 0 & 0 & 0 & 0 & -\frac{4725}{65536} & -\frac{5716305}{524288} \\ 0 & 0 & 0 & 0 & 0 & -\frac{33075}{131072} \\ 0 & 0 & 0 & 0 & 0 & \frac{72765}{524288} \end{bmatrix} \tag{2.53}$$

Two additional useful functions used to simplify the final form of the equations are

$$c_a = \sqrt{\frac{2\,\pi}{c}}\,\frac{(1+e)^{\frac{3}{2}}}{(1-e)^{\frac{1}{2}}} \tag{2.54a}$$

$$c_e = \sqrt{\frac{2\,\pi}{c}}\,\sqrt{\frac{1+e}{1-e}}\,(1-e^2) \tag{2.54b}$$

Finally, the rates of change for highly eccentric orbits are

$$F_a = \frac{\mathrm{d}a}{\mathrm{d}t} = -k_a\,c_a\,\left[\mathbf{r}^T\,\mathbf{K}_a^h\,\mathbf{e} + \mathcal{O}\left(\frac{1}{c^6}\right)\right] \tag{2.55a}$$

$$F_e = \frac{\mathrm{d}e}{\mathrm{d}t} = -k_e\,c_e\,\left[\mathbf{r}^T\,\mathbf{K}_e^h\,\mathbf{e} + \mathcal{O}\left(\frac{1}{c^6}\right)\right] \tag{2.55b}$$

2.3.4 Secular effects from zonal harmonics

In the orbital model used, the secular variation of the other Keplerian elements is also considered, which are subjected to the Earth's gravitational potential. The first-order secular effects resulting from the nonspherical gravity field come from the even zonal (axially symmetrical) harmonics of the Earth's gravity field, J_2. The equations and the physical description of the secular gravitational perturbations are taken from Vallado [2013]. The Earth's oblateness creates an additional attraction of the Earth's equatorial bulge, thus introducing a force component toward the equator. The resulting acceleration causes the satellite to reach the equator (node) short of the crossing point for a spherical Earth. This phenomenon causes the regression of the node (for direct orbits), or a counter rotation of the orbital plane around the polar axis. This affects the right ascension of the ascending node Ω. The nodal regression is described in Equation (2.56) and a visualisation of its effect is provided in Figure 2.7a (Vallado [2013]).

$$\frac{\mathrm{d}\Omega_{sec}}{\mathrm{d}t} = -\frac{3\,n\,R_E^2\,J_2}{2\,p^2}\,\cos i \tag{2.56}$$

Another effect concerns the secular variations caused by J_2 with respect to the apsidal motion, which causes the perigee and apogee locations to change (Figure 2.7b). Note that certain values of inclination can cause $\dot{\omega}$ to vanish, defining a critical inclination ($i = 63.4°, 116.6°$). Those are used to reduce the effect of the J_2 perturbations. The apsidal motion affects the argument of perigee ω, and its expression is given by Equation (2.57) (Vallado [2013]).

$$\frac{\mathrm{d}\omega_{sec}}{\mathrm{d}t} = \frac{3\,n\,R_E^2\,J_2}{4\,p^2}\,\left(4 - 5\,\sin^2 i\right) \tag{2.57}$$

Finally, the secular rate of change for the mean anomaly, independent of the mean motion n, is given by Equation (2.58). The other secular contribution is caused by the mean motion, which depends on the semi-major axis (Equation (2.59)).

$$\frac{\mathrm{d}M_{sec}}{\mathrm{d}t} = -\frac{3\,n\,R_E^2\,J_2\,\sqrt{1-e^2}}{4\,p^2}\,\left(3\,\sin^2 i - 2\right) \tag{2.58}$$

J_2 does not contribute to any secular or long-periodic motion in a because $\mathrm{d}a/\mathrm{d}t$ depends only on terms containing M. The eccentricity e is not affected as well.

2.3.5 Complete set of equations

The equation of the mean anomaly, used to describe the motion of the satellite along the orbital path, needs to take into account the component relative to the mean motion of the satellite. Therefore, the input equation of M in the mathematical model, including

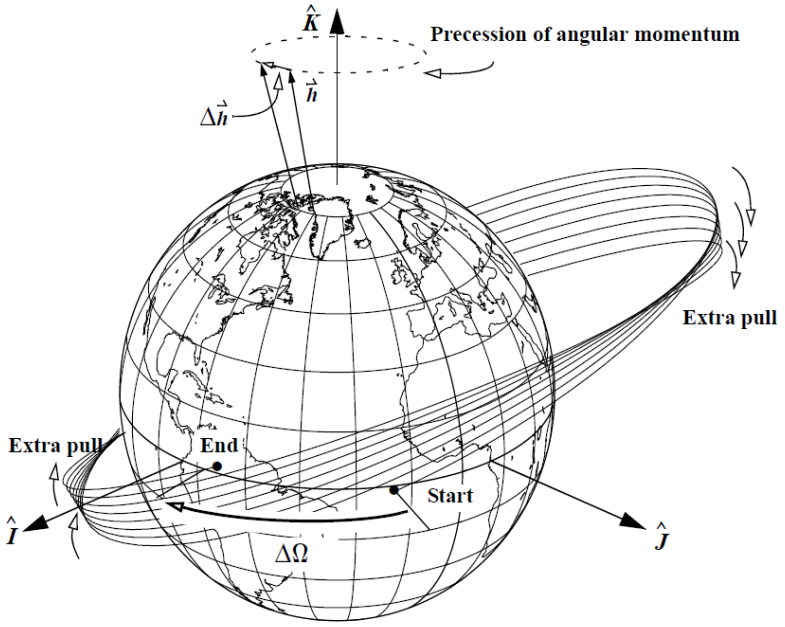

(a) Nodal regression

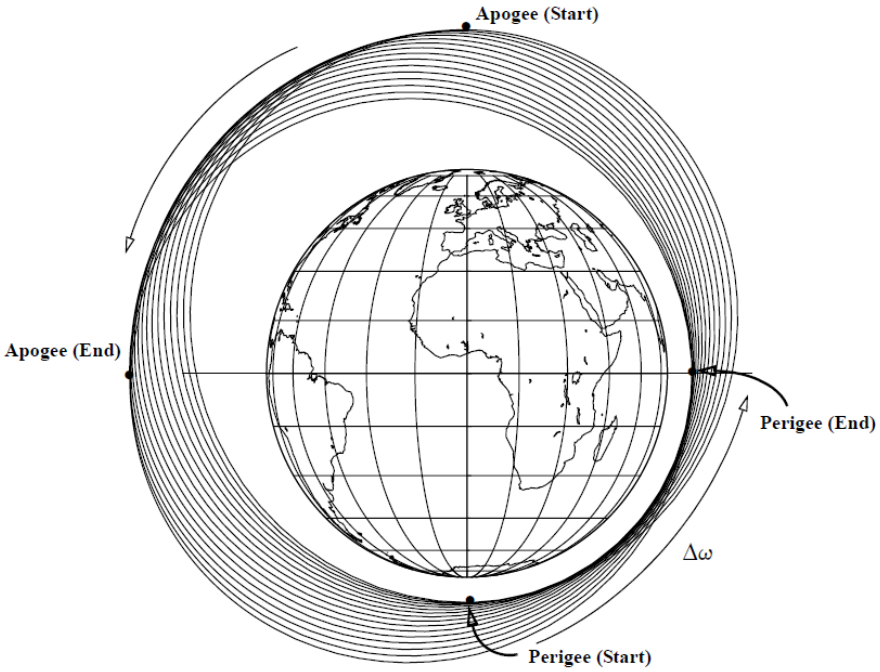

(b) Apsidal motion

Figure 2.7: Secular effect from zonal harmonic J_2. Source: Vallado [2013].

the atmospheric drag and the J_2 gravitational perturbation, is

$$\frac{\mathrm{d}M}{\mathrm{d}t} = n - \frac{3\,n\,R_E^2\,J_2\,\sqrt{1-e^2}}{4\,p^2}\left(3\,\sin^2 i - 2\right) \tag{2.59}$$

The last missing equation is the one providing the variation of the orbital inclination i. Since neither the drag, nor the Earth's oblateness affect the inclination, its derivative is set to zero (Equation (2.60)).

$$\frac{\mathrm{d}i}{\mathrm{d}t} = 0 \tag{2.60}$$

Concluding and summarising, the physical model is described by the following set of equations[2]

$$\begin{cases} \dfrac{\mathrm{d}a}{\mathrm{d}t} = -k_a\,\exp\{(-c)\}\,[\mathbf{e}^T\,\mathbf{K}_a^l\,\mathbf{I}] \\ \dfrac{\mathrm{d}e}{\mathrm{d}t} = -k_e\,\exp\{(-c)\}\,[\mathbf{e}^T\,\mathbf{K}_e^l\,\mathbf{I}] \\ \dfrac{\mathrm{d}i}{\mathrm{d}t} = 0 \\ \dfrac{\mathrm{d}\Omega}{\mathrm{d}t} = -\dfrac{3\,n\,R_E^2\,J_2}{2\,p^2}\,\cos i \\ \dfrac{\mathrm{d}\omega}{\mathrm{d}t} = \dfrac{3\,n\,R_E^2\,J_2}{4\,p^2}\left(4 - 5\,\sin^2 i\right) \\ \dfrac{\mathrm{d}M}{\mathrm{d}t} = n - \dfrac{3\,n\,R_E^2\,J_2\,\sqrt{1-e^2}}{4\,p^2}\left(3\,\sin^2 i - 2\right) \end{cases} \tag{2.61}$$

2.4 Integration of satellite dynamics

The satellite dynamics is described through a set of explicit Ordinary Differential Equations (ODEs). Several methods for the numerical approximation of an ODE solution exist, a complete and exhaustive description is available in Quarteroni et al. [2006]. For the scopes of the present thesis, only a brief introduction of the problem is given. The re-entry problem, within the differential algebra environment, requires the development of an ODEs solver able to deal with DA variables, therefore, the coding of a numerical integrator has been part of the present thesis work.

The introduction of numerical approximation of ODEs solution is provided in Section 2.4.1, the integrator used is presented in Section 2.4.2 and, finally, the implementation of the ODE integrator is discussed in Section 2.4.3.

[2] Just as an example, the equations of a and e are the ones relative to the case $e < e_b$.

2.4.1 Numerical approximation of ODEs solution

The Cauchy problem (also known as the initial-value problem), consists of finding the solution of an ODE, in the scalar case a real-valued function $x \in C^1(I)$, where I denotes an interval of $\mathbb{R}$ containing the point t_0, given suitable initial conditions.

$$\begin{cases} \dfrac{\mathrm{d}x(t)}{\mathrm{d}t} = f(t, x(t)) & t \in I \\ x(t_0) = x_0 \end{cases} \tag{2.62}$$

where $f(t, x)$ is a given real-valued function. The numerical approximation of the Cauchy problem is addressed through numerical methods. The Euler method is the most basic scheme for numerical integration, it is a first-order numerical procedure for solving ordinary differential equations with a given initial value. Two macro categories are linear multi-step methods (MS) and one-step methods, as Runge-Kutta (RK) methods. A numerical method is defined as one-step method if $\forall\, n \geq 0$, the solution u_{n+1} depends only on u_n, so the solution calculated in the previous step. Otherwise, the scheme is called a multi-step method. MS schemes are linear with respect to both u_n and $f_n = f(t_n, u_n)$, they require only one function evaluation at each time step, and their accuracy can be increased at the expense of increasing the number of steps. On the other hand, RK methods maintain the structure of one-step methods, and improve their accuracy at the price of an increase of function evaluation at each time level, thus sacrificing linearity.
In the most general form, an RK method can be written as

$$u_{n+1} = u_n + h\, F(t_n, u_n, h; f) \qquad n \geq 0 \tag{2.63}$$

where F is the increment function defined as follows

$$F(t_n, u_n, h; f) = \sum_{i=1}^{s} b_i\, K_i \tag{2.64}$$

$$K_i = f(t_n + c_i\, h, u_n + h \sum_{j=1}^{s} a_{i\,j}\, K_j) \qquad i = 1,2,\ldots,s \tag{2.65}$$

s denotes the number of stages of the method. The coefficients $\{a_{i\,j}\}$, $\{c_i\}$, and $\{b_i\}$ fully characterise an RK method, and are usually collected in the so-called Butcher array (Quarteroni et al. [2006])

$$\begin{array}{c|cccc} c_1 & a_{11} & a_{12} & \ldots & a_{1s} \\ c_2 & a_{11} & a_{12} & & a_{1s} \\ \vdots & \vdots & & \ddots & \vdots \\ c_s & a_{s1} & a_{s2} & \ldots & a_{ss} \\ \hline & b_1 & b_2 & \ldots & b_s \end{array} \qquad \text{or} \qquad \begin{array}{c|c} \mathbf{c} & A \\ \hline & \mathbf{b}^T \end{array}$$

where $A = (a_{ij}) \in \mathbb{R}^{s \times s}$, $\mathbf{b} = (b_1, \ldots, b_s)^T \in \mathbb{R}^s$, and $\mathbf{c} = (c_1, \ldots, c_s)^T \in R^s$.
Another dichotomy distinguishes between explicit and implicit schemes. Explicit methods calculate the state of a system u_{n+1} from the state of the system at the current time, u_n, while implicit methods find the solution u_{n+1} by solving an equation involving both the current state u_n and the later state of the system u_{n+1} itself. If the coefficients a_{ij} in A are equal to zero for $j \geq i$, with $i = 1, 2, \ldots, s$, then each K_i can be explicitly computed in terms of the $i-1$ coefficients $K_1, \ldots, K_{i-1}$ that have already been determined. In such a case the RK method is explicit. Otherwise, it is implicit, and solving a nonlinear system of size s is necessary for computing the coefficients K_i. The equations describing the spacecraft dynamics are explicit, therefore, only those methods are further investigated.
RK schemes are one-step methods, and they are well-suited to adapting the step-size h, provided that an efficient estimator of the local error is available. The error estimation can be constructed in two ways, the first consists in using the same RK method with two different step-sizes, while the second uses two RK methods of different order, but with the same number s of stages. The latter method does not require extra functional evaluations. The two RK methods, of order p and $p+1$, respectively, share the same set of values K_i. These methods are synthetically represented by the modified Butcher array

$\mathbf{c}$	A
	$\mathbf{b}^T$
	$\hat{\mathbf{b}}^T$
	$\hat{\mathbf{E}}^T$

where the method of order p is identified by the coefficients $\mathbf{c}$, A and $\mathbf{b}$, while that of order $p+1$ is identified by $\mathbf{c}$, A and $\hat{\mathbf{b}}$, and where $\mathbf{E} = \mathbf{b} - \hat{\mathbf{b}}$. Taking the difference between the approximate solutions at $t_n + 1$ produced by the two methods, provides an estimate of the local truncation error for the scheme of lower order. On the other hand, since the coefficients K_i coincide, this difference is given by $h \sum_{i=1}^{s} E_i K_i$ and thus it does not require extra function evaluations.

2.4.2 Dormand-Prince method

The chosen integrator is the Dormand-Prince method, which is a member of the explicit Runge–Kutta family (Dormand and Prince [1980]).
This method uses six function evaluations per iteration and seven stages. The algorithm includes the calculation of two solutions per step, of fourth- and fifth-order accuracy,

therefore adapting the step-size by means of two RK methods of different order. The 5^{th}-order accurate algorithm is propagated, whereas the 4^{th}-order algorithm is used for step-size control purposes (Cellier and Kofman [2013]). The Butcher tableau of the Dormand-Prince pair is reported below and taken from Dormand and Prince [1980].

0							
$\frac{1}{5}$	$\frac{1}{5}$						
$\frac{3}{10}$	$\frac{3}{40}$	$\frac{9}{40}$					
$\frac{4}{5}$	$\frac{44}{45}$	$-\frac{56}{15}$	$\frac{32}{9}$				
$\frac{8}{9}$	$\frac{19372}{6561}$	$-\frac{25360}{2187}$	$\frac{64448}{6561}$	$-\frac{212}{729}$			
1	$\frac{9017}{3168}$	$-\frac{355}{33}$	$\frac{46732}{52247}$	$\frac{49}{176}$	$-\frac{5103}{18656}$		
1	$\frac{35}{384}$	0	$\frac{500}{1113}$	$\frac{125}{192}$	$-\frac{2187}{6784}$	$\frac{11}{84}$	
	$\frac{35}{384}$	0	$\frac{500}{1113}$	$\frac{125}{192}$	$-\frac{2187}{6784}$	$\frac{11}{84}$	0
	$\frac{5179}{57600}$	0	$\frac{7571}{16695}$	$\frac{393}{640}$	$-\frac{92097}{339200}$	$\frac{187}{2100}$	$\frac{1}{40}$

Algorithm 1 provides the general formulation of the Dormand-Prince method, and its and its salient features.

2.4.3 ODEs integrator implementation

The integrator has been developed in the C++ environment. In the Dormand-Prince algorithm here provided, it is particularly stressed the importance of setting a lower boundary for the step size, the reason concerns its application to the re-entry problem. The deorbiting phase is extremely demanding for an integrator as the one described above. In particular, it has been proven with several failed integrations that before reaching 100 km altitude, the orbital propagation interrupts, since the step size is reduced below the lower limit allowed.

For this reason, the integrator has been modified to successfully integrate up to the desired re-entry altitude. Each portion of the newly developed code is based on `Matlab ode45` function[3]. This also guarantees a complete match between the double precision results obtained within the two software environments, in terms of integration variables, time and step size. The perfect match requires to change the `ode45` refinement from 4 (default) to 1 (no refinement).

[3] Algorithms, *ode45*: `https://www.mathworks.com/help/matlab/ref/ode45.html`, accessed: 14/02/2020.

Algorithm 1: Algorithm of the Dormand-Prince method.

Data: $f(t, x(t))$, initial and final time t_0 and t_f, initial conditions x_0, absolute tolerance, relative tolerance, parameters.
Result: Final condition $x(t_f)$.

initialisation;
define A, b, $\hat{b}$ and d;
define initial step size h;
evaluate $f(t_0, x_0)$;
while *final time is not exceeded* **do**
  check if final time is exceeded by step size, if so $h = t_f - t_n$;
  define $h_{min} = 16 \cdot eps(t)$;
  set $X_1 = x_n$;
  set $f_1 = f(t_n, x_n)$;
  for $i = 2 \ldots 7$ **do**
    calculate $X_i = x_n + h \sum_{j=1}^{i-1} a_{i,j} f_i$;
    evaluate $f_i = f(t_n + c_i h, X_i)$;
  end
  set $\hat{x}_{n+1} = X_7$;
  set $f(t_{n+1}, \hat{x}_{n+1}) = f_7$;
  calculate $e_{n+1} = h \cdot \sum_{i=1}^{7} d_i f_i$;
  if *the step is accepted* **then**
    update step size;
    set $x_{n+1} = \hat{x}_{n+1}$;
    calculate $t_{n+1} = t_n + h$;
  else
    update the failed step, by reducing the step size;
  end
  set $h = \hat{h}$;
  if $h \leq h_{min}$ **then**
    return $x(t)$, as the step size is below the minimum allowed;
  end
  return $x(t_f)$;
end

In Figure 2.8 the tested orbit has a re-entry time of about 400 years, the choice is made to confirm the match between `ode45` and the integrator coded for the scope of this thesis work, in this frame named rkdp45. Figure 2.8a shows the integration step-size, while Figure 2.8b the step size adaption, both are perfectly equal to the `ode45` result.

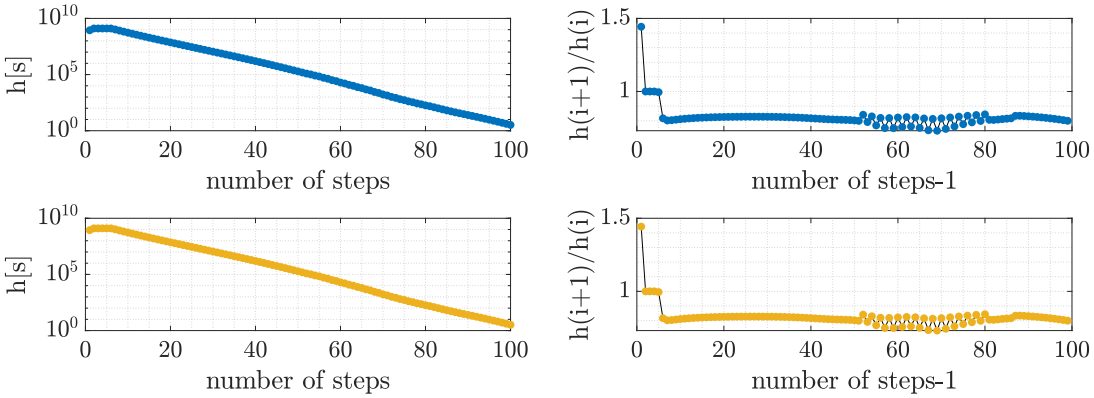

(a) Step-size throughout the integration.

(b) Step adaption throughout the integration.

Figure 2.8: Comparison between Matlab ode45 and the integrator developed in this work.

2.5 Automatic domain splitting in DA

Orbital mechanics equations, along with the implemented density model, are highly non-linear, since the Keplerian elements experience fast and major variations during the de-orbiting, due to the increased action of the atmospheric drag.
While differential algebra is a powerful tool, it requires the equations to be as smooth as possible, since non-linearities would prohibit good convergence of the Taylor expansion in one or more DA variable directions, especially when high orders are used. In fact, several numerical issues arise when differential algebra is applied to the re-entry problem defined in Section 2.3. Non-linearities tend to sharply increase the size of the expansion coefficients, and the evaluation and inversion of the polynomials can cause the code to fail. Numerical issues are deeply analysed in Section 3.3.1. The automatic domain splitting routine, developed by Wittig et al. [2015], solves the issue by splitting the polynomial expansion of the current state in two polynomials, whenever its accuracy is below an accepted tolerance. Thus, with a strategy sometimes referred as divide and conquer, the algorithm is stopped when the expansion accuracy becomes too low and, after the split, the integration continues on the two separate domains. The procedure is applied until each subdomain re-enters. The final result is indeed a list of final state polynomials, each describing the evolution of some automatically determined subset of the initial condition, tackling the non-linearities issue. In the following Section 2.5.1, the mathematical formulation is relying on the description provided by Wittig et al. [2015].

2.5.1 Mathematical formulation

Given an $n+1$ times differentiable function $f \in C^{n+1}$, and a Taylor expansion P_f of order n taken around the origin, the approximation error is bounded due to Taylor's theorem Equation (2.66) for a constant C.

$$|f(\delta x) - P_f(\delta x)| \leq C\, \delta x^{n+1} \tag{2.66}$$

It is possible to define e_r as the maximum error of P_f on a domain B_r of radius $r > 0$ around the centre of the expansion, as in Equation (2.67).

$$|f(\delta x) - P_f(\delta x)| \leq C\, \delta x^{n+1} \leq C\, r^{n+1} \leq e_r \tag{2.67}$$

Thus, if the radius r is divided by a factor 2, the error on the sphere $B_{r/2}$ will decrease by a factor $1/2^{n+1}$, as in Equation (2.68).

$$|f(\delta x) - P_f(\delta x)| \leq C\, \delta x^{n+1} \leq C \left(\frac{r}{2}\right)^{n+1} \leq \frac{e_r}{2^{n+1}} \tag{2.68}$$

As a consequence, when large expansion orders are used, for example 9 or greater, splitting the variable domain in two parts can decrease the maximum error by a factor $\frac{1}{2^{10}} \approx 10^{-4}$. The two resulting polynomial expansions improve their accuracy, while still covering the whole domain when considered together. As an example, given a flow $\Phi(t_i, \delta\boldsymbol{x})$ and its polynomial approximation $P(\delta\boldsymbol{x})$ at time t_i on the domain $\delta\boldsymbol{x} \in [-1,1]^k$, the domain split along direction j is defined as in Equation (2.69) and Equation (2.70). The two resulting polynomials P_1 and P_2, are still defined on $\delta\boldsymbol{x} \in [-1,1]^k$, but their evaluation covers the j dimension on $[-1,0]$ and $[0,1]$, respectively. It is important to note that, while being arbitrary, the parametrisation of the domain bounds allows the automatic extension of the split propagation in any DA variable direction. Moreover, it offers great numerical benefits, since the coefficients becomes dimensionless and their sizes comparable.

$$P_1(\boldsymbol{\delta x}) = P(\delta x_1, .., \delta x_{j-1}, \frac{1}{2}\delta x_j - \frac{1}{2}, \delta x_{j+1}, ..., \delta x_k) \tag{2.69}$$

$$P_2(\boldsymbol{\delta x}) = P(\delta x_1, .., \delta x_{j-1}, \frac{1}{2}\delta x_j + \frac{1}{2}, \delta x_{j+1}, ..., \delta x_k) \tag{2.70}$$

The mathematical formulation of the splitting procedure must be adapted to the re-entry problem. The main routine is defined in Algorithm 2. During the integration the initial domain is split to guarantee the expansion convergence, the routine is iterated until each subdomain is re-entered. In the present section, the DA variables are assumed to be representative of uncertainties expressed in Keplerian elements. Nevertheless, this choice is not maintained throughout the thesis, since DA variables are expressed in other sets of elements according to the need. In fact, the number of DA variables can be higher or

Algorithm 2: Main iterative procedure of the domain splitting.

Data: Initial condition $\mathbf{X}_0$, initial uncertainty, $\boldsymbol{\sigma}$.
Result: Final state expansions of all the domains $\mathbf{X}(t_f, \delta\mathbf{x})$.

```
DACE initialisation, expansion order n;
set maximum number of splits n_max;
while true do
    for each d-subdomain do
        if d is not reentered then
            if splits of d < n_max then
                integrate X_d(t, δx) until h_re−entry or Algorithm 3 returns;
            else
                integrate X_d(t, δx) until h_re−entry;
            end
            calculate the final altitude h_f;
            if h_f < h_reentry then
                save the final condition X_d(t_f, δx);
            else
                for each i-state expansion do
                    split X_{d,i}(δx) along direction I, Equation (2.81a) and
                     Equation (2.81b);
                end
                update the number of domains;
            end
        end
    end
    if all the domains are re-entered, set false;
end
```

lower than the number of expansion variables. It is sufficient to define the initial state in the desired coordinates, apply the uncertainties and transform those DA objects into the state expansion in Keplerian elements.
The initial satellite state in Keplerian elements is

$$\mathbf{X}_0 = \begin{pmatrix} a_0 & e_0 & i_0 & \Omega_0 & \omega_0 & M_0 \end{pmatrix} \tag{2.71}$$

While the initial set of uncertainties is named $\boldsymbol{\sigma}$, and contains the uncertainty domain interval

$$\boldsymbol{\sigma} = \begin{pmatrix} \sigma_a & \sigma_e & \sigma_i & \sigma_\Omega & \sigma_\omega & \sigma_M \end{pmatrix} \tag{2.72}$$

Each DA variable represents a variation of the initial condition of a Keplerian element

$$\delta\mathbf{x} = \begin{pmatrix} \delta a & \delta e & \delta i & \delta\Omega & \delta\omega & \delta M \end{pmatrix} \tag{2.73}$$

They are parametrised with respect to the initial uncertainty $\boldsymbol{\sigma}$, so that they have unitary bounds, $\delta x_i \in [-1,1] \, \forall \, i$. This choice is arbitrary, but it simplifies the calculations. The initial state is transformed in a DA object, named $\mathbf{X}(t_0, \delta\mathbf{x})$. It represents the vector of state expansions

$$X_i(t_0, \delta\boldsymbol{x}) = X_{0,i} + \sigma_i \cdot \delta x_i \qquad \text{for } i = 1, 2, \ldots, 6 \tag{2.74}$$

Thus, $X_i(t_0, \delta\mathbf{x})$ is the expansion state of the Keplerian element i at the initial time t_0 as a function of all the DA variables. Initially, the only non-zero coefficient is the one relative to δx_i.

Once initialised the DA environment of order n, and determined the initial condition, the satellite trajectory is propagated within the ODE solver.

In particular, given the vector of unknown orbital parameters and their dependencies on each DA variable, two criteria are defined. The first consists in establishing whether the domain needs to be split, identifying the state expansion which converges less. The second allows to determine the direction of the split. The non-converging DA polynomial, found in the previous step, is used to define which DA variable affects the expansion more. Once the direction of the splitting is chosen, the integration is stopped, and the initial polynomial is split into two. The two sets of state expansions are therefore propagated until the re-entry of all the polynomials.

Each iteration is checked two times, as described in Algorithm 3. The first arrests the integration when the final altitude is below the re-entry altitude. The second involves the domain splitting. In the latter case, the estimated norm of a state expansion is compared with a tolerance ϵ, which can potentially be different for each flow variable under evaluation. If at least one polynomial experiences an estimated truncation error which exceeds the tolerance, the integration is stopped, since the expected accuracy is not guaranteed anymore. If more than one state expansion is not converging within the desired limit, the domain is then split according to the DA variable that converges less.

An important choice regards the accepted tolerance ϵ for the truncation error. The ideal tolerance for the splitting precision depends both on the dynamics, as more splits lead to more accumulation of approximation errors, and the integration time. It has to be chosen heuristically to ensure the final result satisfies the accuracy requirements of the application, without losing computational time.

Concerning the decision whether the splitting is necessary, refer to Algorithm 4. Each y-state expansion is factored as

$$X_y(\delta\boldsymbol{x}) = \sum_{\alpha} a_\alpha \, \delta\boldsymbol{x}^\alpha \tag{2.75}$$

Using multi-indexing notation for polynomial orders, the coefficient order sizes S_j for each y-state expansion are computed as

$$S_j = \sum_{|\alpha|=j} |a_\alpha| \qquad \text{for } j = 0, 1, ..., n \tag{2.76}$$

S_j are exponentially fitted to the polynomial orders

$$f(j) = A\, e^{B\, j} \tag{2.77}$$

where $f(j)$ is approximated to S_j in a least square sense. The fit is used to estimate size S_{n+1}

$$S_{n+1} = f(n+1) \tag{2.78}$$

If S_{n+1} exceeds the tolerance, the desired accuracy is not guaranteed anymore, therefore a split is required.

The polynomial characterised by the maximum S_{n+1}, is identified with the index Y, and it is analysed to select the splitting direction, as Algorithm 5 illustrates.

$X_Y(\delta \boldsymbol{x})$ is factorised as

$$X_Y(\delta \boldsymbol{x}) = \sum_{j=0}^{n} \delta x_i^j \, q_{i,j}(\delta x_1, ..., \delta x_{i-1}, \delta x_{i+1}, \delta x_6) \tag{2.79}$$

for each DA variable δx_i.

Then, coefficient order sizes $\tilde{S}_j$ are computed as the sum of the absolute values of all the coefficients in $q_{i,j}(\delta x_1, ..., \delta x_{i-1}, \delta x_{i+1}, \delta x_6)$. Those are exponentially fitted to the polynomial orders using least squares, as

$$\tilde{f}(j) = A\, e^{B\, j} \tag{2.80}$$

The fit is used to estimate size $\tilde{S}_{n+1}$.

The splitting direction is chosen as the DA variable corresponding to the maximum $\tilde{S}_{n+1}$, which is referred as I.

Once determined the direction of the split, each y-state expansion, where $y = 1, 2, \ldots 6$, is split according to the direction I

$$X_y^+(\delta \boldsymbol{x}) = X_y(\delta x_1, .., \delta x_{I-1}, \frac{1}{2}\delta x_I + \frac{1}{2}, \delta x_{I+1}, ..., \delta x_6) \tag{2.81a}$$

$$X_y^-(\delta \boldsymbol{x}) = X_y(\delta x_1, .., \delta x_{I-1}, \frac{1}{2}\delta x_I - \frac{1}{2}, \delta x_{I+1}, ..., \delta x_6) \tag{2.81b}$$

As a final remark, an alternative criterion to decide whether the splitting is necessary, involves the computation of a DA object derived from a combination of DA expansions, for example the altitude h, or the perigee altitude h_p. Therefore, only the norm estimate of the quantity of interest is compared with the accepted tolerance ϵ, reducing the for loop in Algorithm 4 to a single evaluation.

Algorithm 3: Domain splitting procedure within the ODE solver.

Data: State expansion $\mathbf{X}(\delta\mathbf{x})$ of order n.
Result: State $\mathbf{X}(\delta\mathbf{x})$ if the domain splitting is required.
calculate the maximum residual R through Algorithm 4;
if $R > 0$ **then**
    calculate the splitting direction I by means of Algorithm 5;
    return $\mathbf{X}(\delta\mathbf{x})$ and I;
end

Algorithm 4: Domain splitting decision.

Data: State expansion $\mathbf{X}(\mathbf{x})$ of order n, tolerance vector $\boldsymbol{\epsilon}$.
Result: Maximum residual R.
for *each y-state variable* **do**
    factor $X_y(\delta\mathbf{x})$, as in Equation (2.75);
    calculate the coefficient order sizes S_j;
    exponentially fit S_j;
    estimate S_{n+1};
end
calculate $R = max(S_{y,n+1} - \epsilon_y)$;
return R;

2.5.2 Domain splitting illustration

The domain splitting has the benefit of maintaining the accuracy of high orders while ensuring the convergence of the expansion. Monte Carlo methods are efficient, but computational intensive. An example of the impact distribution over the Earth's surface generated through a Monte Carlo simulation is in Figure 2.9a. The red square represents the impact location of the nominal initial state, marked as central point.
Differential algebra has been already proven to be an efficient compromise by replacing thousands of point-wise integrations of Monte Carlo runs with the fast evaluation of the arbitrary order Taylor expansions of the flow of the dynamics. Nevertheless, Monte Carlo methods are often the only option available to deal with actual large uncertainty sets. In Figure 2.9b, it is shown the result obtained with a single differential algebra expansion. The final state polynomial is not able to represent all the displaced points belonging to the initial cloud of points. In fact, only a portion of the actual uncertainty interval is well represented, while the missing points are not converging as they should. The domain splitting has the power of replacing the brute-force approach of Monte Carlo methods, while keeping the differential algebra advantage of replacing point-wise integration with polynomial evaluations. The impact distribution obtained for the same initial state and

Algorithm 5: Splitting direction selection.

Data: State expansion $\mathbf{X}(\mathbf{x})$ of order n.
Result: Splitting direction I.
for *each DA variable* δx_i **do**
    factor $X_Y(\mathbf{x})$, as in Equation (2.79);
    calculate coefficient order sizes $\tilde{S}_j$;
    exponentially fit $\tilde{S}_j$;
    estimate $\tilde{S}_{n+1}$;
end
calculate $max(\tilde{S}_{i,n+1})$, and the corresponding index I;
return I;

uncertainties of the previous figure, but using the domain splitting, is provided in Figure 2.9c. Red crosses represent the central points of the generated polynomials. The propagation exploiting the domain splitting technique is characterised by an higher computational time compared with the single polynomial expansion, but it has the advantage of representing the complete uncertainty set with an higher accuracy.
The DA variables included within the present simulation are relative to the semi-major axis a and the eccentricity e. Figure 2.10 provides the initial 2D uncertainty domain, in the a and e variables, and the final distribution of the subdomains. Each rectangle is a subdomain, which identifies the validity region of a certain set of polynomials. Clearly, most of the splits occur in a-direction, which, in this case, is the variable which influences the expansion more.
A polynomial is in general split as a result of the presence of nonlinearities, since the re-entry phase is highly non-linear, it is not surprising that the number of splits increases as the spacecraft approaches the Earth's atmosphere. In Figure 2.11, it is shown how the number of domains increases along with the integration time, eventually reaching the re-entry altitude.
Regarding the computational time, as previously stated, the domain splitting causes the computational time of a differential algebra simulation to increase, compared with the classic implementation of a DA propagation. However, what is interesting is to compare the computational time of the numerical Monte Carlo with the differential algebra, when the domain splitting is implemented. The domain splitting is proven to be able to reduce the computational time when propagating the trajectory of celestial bodies in orbit around the Sun, as done by Wittig et al. [2015], in the case of the (99942) Apophis post-encounter motion. In the re-entry phase, a first result is provided in Figure 2.12. The computational time of the differential algebra simulation, in red, starts from 100 s since it is the time required to propagate all the split polynomial to the re-entry altitude. Then,

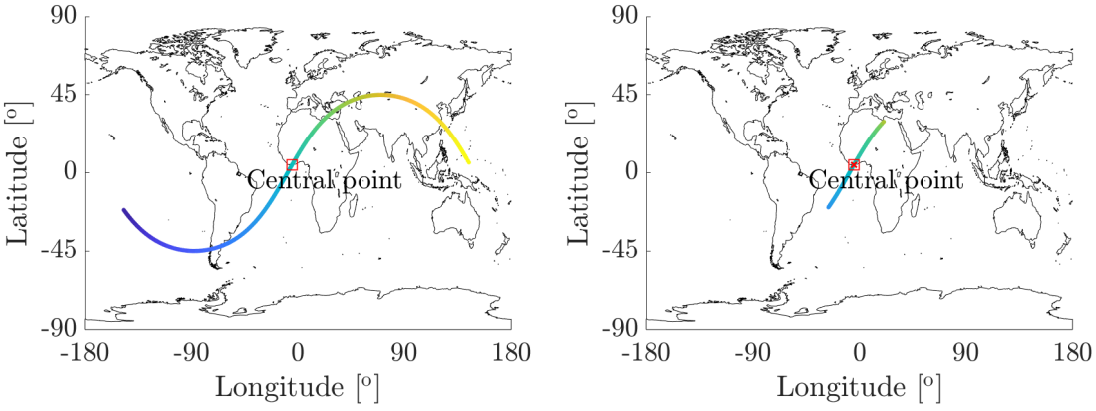

(a) Numerical Monte Carlo

(b) DA, without the domain splitting

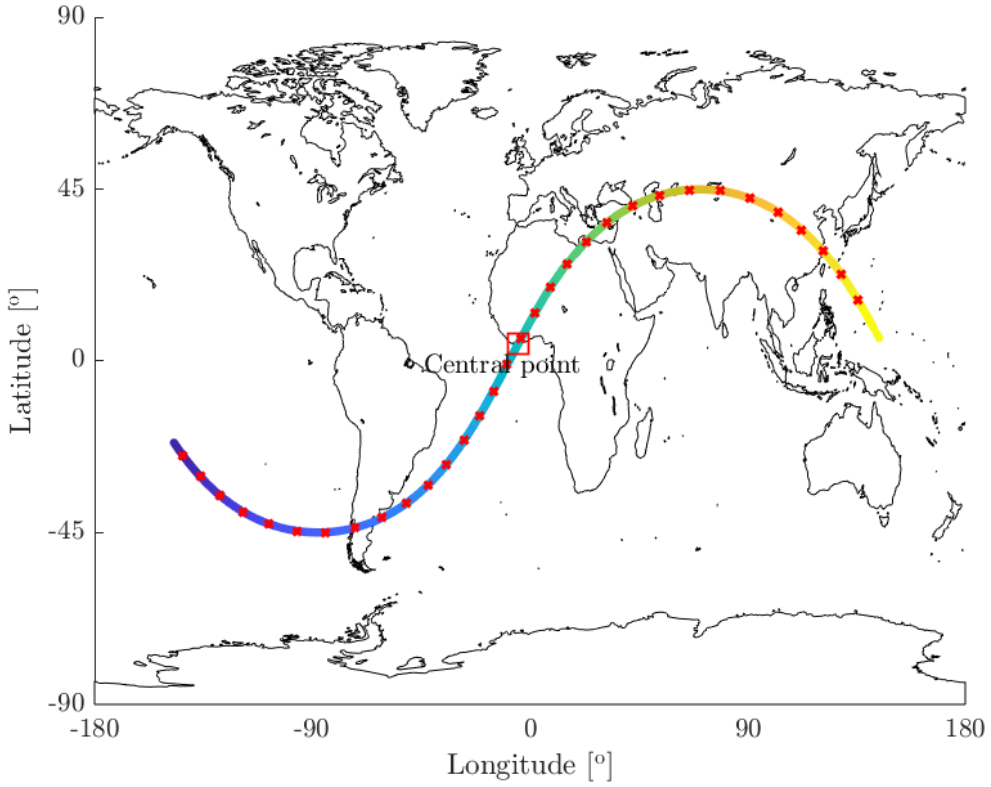

(c) DA, including the domain splitting

Figure 2.9: Comparison of the ground map risk in three different simulation environments.

the evaluation of the polynomial occurs through the constraint satisfaction, which is a technique implemented for the scope of the present thesis work and described in Section

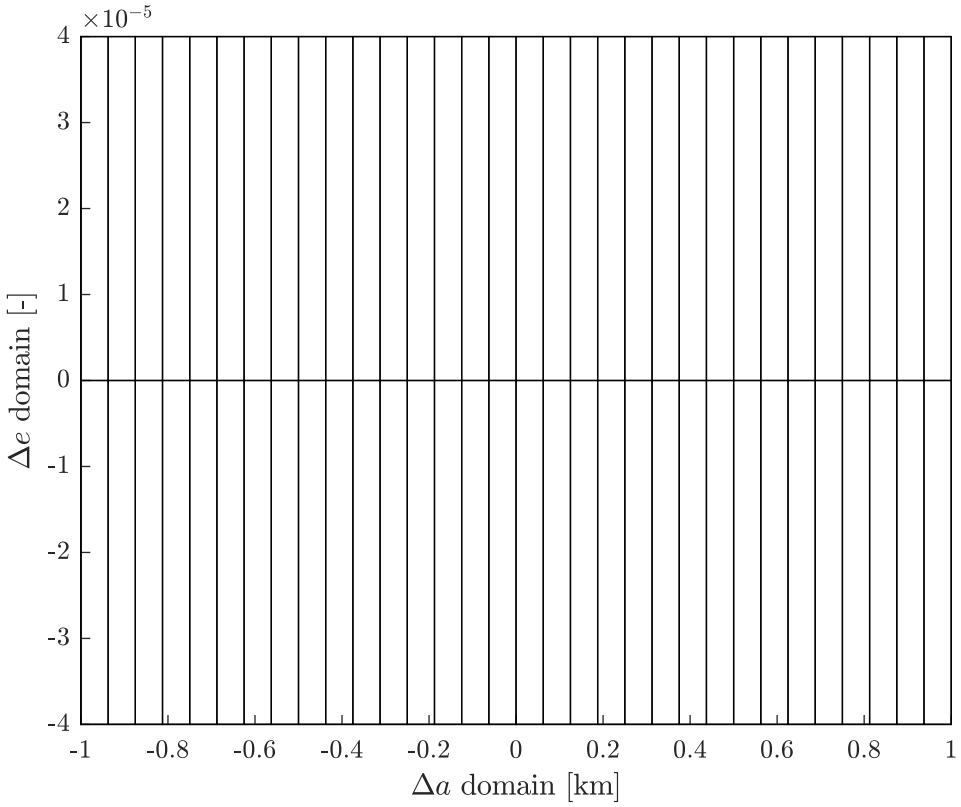

Figure 2.10: Final subdomains of the initial domain in the a, e-plane.

2.6. The numerical Monte Carlo computational time increases linearly with the number of evaluations, since it is a point-wise method. Provided that the number of desired evaluations is kept above the break-even point, namely the intersection of the two curves, the domain splitting constitutes a powerful tool that can save precious computational time.

2.6 Constraint satisfaction

This section is based on the notes kindly provided by Dr. Alexander Wittig. The Constraint Satisfaction (CS) is the tool that allows the differential algebra to be related and successfully applied to re-entry problem. Before going into the details of its mathematical formulation, it is important to provide some insights on what the constraint satisfaction allows. It is based on the introduction of an additional DA variable, representing the time. Given initial conditions in the Keplerian elements and the re-entry altitude, the central point of the expansion is propagated until the eventual re-entry. The result, in the

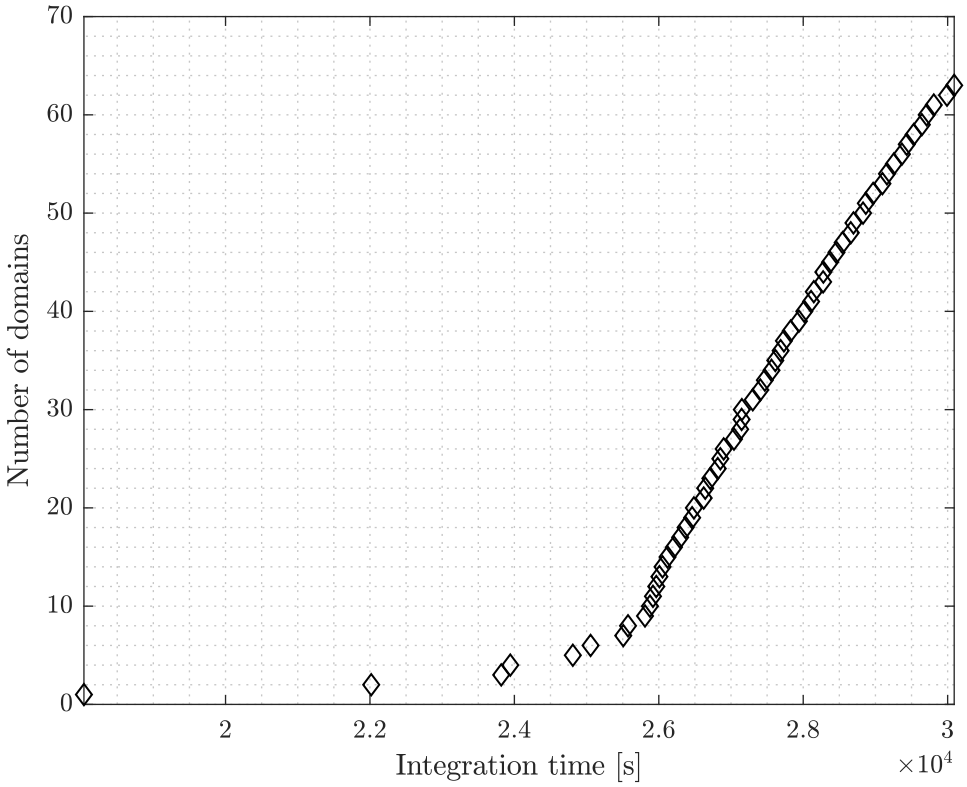

Figure 2.11: Integration time versus the number of splits required by the automatic domain splitting algorithm.

DA environment, is a Taylor series expansion in six DA variables, one for each Keplerian element (δa, δe, δi, $\delta\Omega$, $\delta\omega$, δM). As for the domain splitting routine, the mathematical formulation is provided with uncertainties in Keplerian elements, even if the DA variables used can differ, opting for any desired set.

The final polynomial expansions can be evaluated for certain displacements, in the initial conditions, of the same DA variables. Provided that the displaced point lies inside the domain of convergence, the resulting output of the evaluation is a vector containing the final configuration, in terms of Keplerian elements, of the displaced initial condition, at the final time. With the expression final time it is meant the time for which the reference point has reentered, condition that stops the propagation in the ODE integrator. Through the constraint satisfaction, it is possible to find the δt_f for which the evaluated point, instead of being in a random position, lies on the re-entry sphere of radius equal to the chosen re-entry altitude. In practice, all the evaluated points are shifted, and their

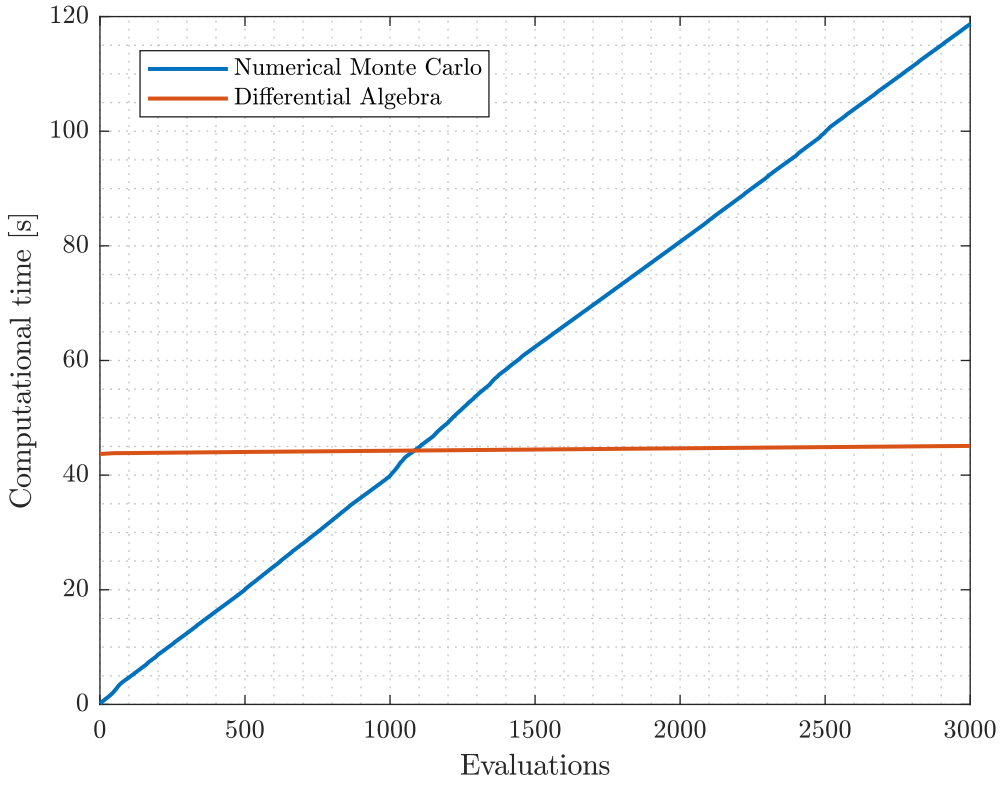

Figure 2.12: Evaluations versus computational time, comparison between the numerical Monte Carlo and the differential algebra, in the presence of the domain splitting.

re-entry location and time can be successfully retrieved. Concluding, for each point characterised by a displacement in the initial condition, the constraint satisfaction allows to find exactly the re-entry position, in both space and time.

2.6.1 Mathematical formulation

This section provides the complete mathematical framework to build the constraint satisfaction. The first step is the definition of a function $\phi(t, \mathbf{x}_f) : \mathbb{R}^7 \to \mathbb{R}^6$ such that

$$\phi(0, \mathbf{x}_f) = \mathbf{x}_f \tag{2.82a}$$

$$\frac{\mathrm{d}\phi(t, \mathbf{x}_f)}{\mathrm{d}t} = \mathbf{f}(\phi(t, \mathbf{x}_f)) \tag{2.82b}$$

where $\mathbf{x}_f$ is the final state, namely the final condition that characterises the re-entry of the reference point. For simplicity $t = 0$ is the re-entry time, that more rigorously should

be named t_f. Since in this formulation the re-entry time is assumed to be the initial condition, the resulting output of the constraint satisfaction, which is in effect a $\delta\, t_f$, is simply a time, which is named t^*. $\mathbf{f}$ is constituted by the equations listed in Equation (2.61), which represent the right hand side of the ODE integrated.

$$\phi(t, \mathbf{x}_f) = \mathbf{x}(t=0) + \int_0^{\tilde{t}} f(\mathbf{x}(t))\, \mathrm{d}t \tag{2.83}$$

Equation (2.83) is therefore iterated, each time $\mathbf{x}$ becomes a time expansion of one additional order. Through this integration, time becomes an additional variable, the DA variable number 7. Thus, the result is an expansion in spatial, DA variables from 1 to 6, and temporal variables. The time component is a DA variable around the re-entry time. The second step consists in computing in which time instant the displaced point under evaluation reenters. For the re-entry, the constraint that has to be satisfied is

$$h(t^*) = h_{re-entry} \tag{2.84}$$

in Keplerian elements this is translated into

$$\frac{a\,(1-e^2)}{1+e\,\cos\theta} - R_{Earth} = h_{re-entry} \tag{2.85}$$

To fulfill this condition, the additional function $\mathbf{F}$ is introduced. $\mathbf{F} : \mathbb{R}^7 \rightarrow \mathbb{R}^7$ is a function of all the DA variables, both spatial and temporal

$$\mathbf{F}\begin{pmatrix} \delta a \\ \delta e \\ \delta i \\ \delta\Omega \\ \delta\omega \\ \delta M \\ t \end{pmatrix} = \begin{pmatrix} \delta a \\ \delta e \\ \delta i \\ \delta\Omega \\ \delta\omega \\ \delta M \\ h - h_{re-entry} \end{pmatrix} \tag{2.86}$$

In order to enforce the perfect satisfaction of the constraint in Equation (2.85), thus when the point effectively reenters the Earth, the expression $h - h_{re-entry}$ is supposed known and equal to zero. The right hand side becomes fully defined, leading to the last step, which consists in the inversion of function $\mathbf{F}$, as

$$\mathbf{F}^{-1}\left(\mathbf{F}\begin{pmatrix} \delta a \\ \delta e \\ \delta i \\ \delta\Omega \\ \delta\omega \\ \delta M \\ t^* \end{pmatrix}\right) = \begin{pmatrix} \delta a \\ \delta e \\ \delta i \\ \delta\Omega \\ \delta\omega \\ \delta M \\ t^* \end{pmatrix} = \mathbf{F}^{-1}\begin{pmatrix} \delta a \\ \delta e \\ \delta i \\ \delta\Omega \\ \delta\omega \\ \delta M \\ 0 \end{pmatrix} \tag{2.87}$$

Finally, from the last component of $\mathbf{F}^{-1}$, t^* is

$$t^* = F_7^{-1} \begin{pmatrix} \delta a \\ \delta e \\ \delta i \\ \delta \Omega \\ \delta \omega \\ \delta M \\ 0 \end{pmatrix} \tag{2.88}$$

By means of this inversion, it is possible to compute the time t^*, which is exactly the desired time variation which satisfies the re-entry condition. Once t^* is known, it is possible to compute the state $x(t^*)$ from Equation (2.83).
This procedure allows to evaluate the re-entry condition of any point characterised by a reasonable displacement with respect to the initial state of the reference point.

2.6.2 Constraint satisfaction illustration

After the formal description of the constraint satisfaction, it is interesting to provide some graphical information, in order to exactly show its application.
Figure 2.13 gives an insight on how the constraint satisfaction acts. Expansion evaluation points, in blue, are computed evaluating the DA expansion of the reference points with a variation applied in the semi-major axis. Before the CS, at time $t = t_{f,\,central}$, expansion evaluation points are located at altitudes different from the re-entry altitude of the central point. The constraint satisfaction allows to shift those points on the spherical surface with radius equal to the central point re-entry radius. The central point, obviously, constitutes the interception between the expansion evaluation and the constraint satisfaction. The sphere represented in the figure has a radius equal to the re-entry altitude. The x, y, z coordinates in Figure 2.13 do not represents the space coordinates of the Earth inertial reference system (X, Y, Z). In fact, the procedure adopted involves a scaling with respect to the radius of the Earth to better visualise the concept. Starting from the cartesian coordinates in (X, Y, Z), a conversion in spherical coordinates has been performed, then the radius ρ has been scaled, subtracting to it the Earth radius. Finally, a second conversion from spherical coordinates to coordinates (x, y, z) has been applied. This means that the angles (θ, ψ) are properly represented, and only the radius is in reality a non-physical variable.
Figure 2.14 explains the CS from the temporal viewpoint. It shows two points, in blue and yellow, characterised by a negative and positive displacement, respectively. On the x axis there is the δt_f, which is the time difference with respect to the re-entry time of

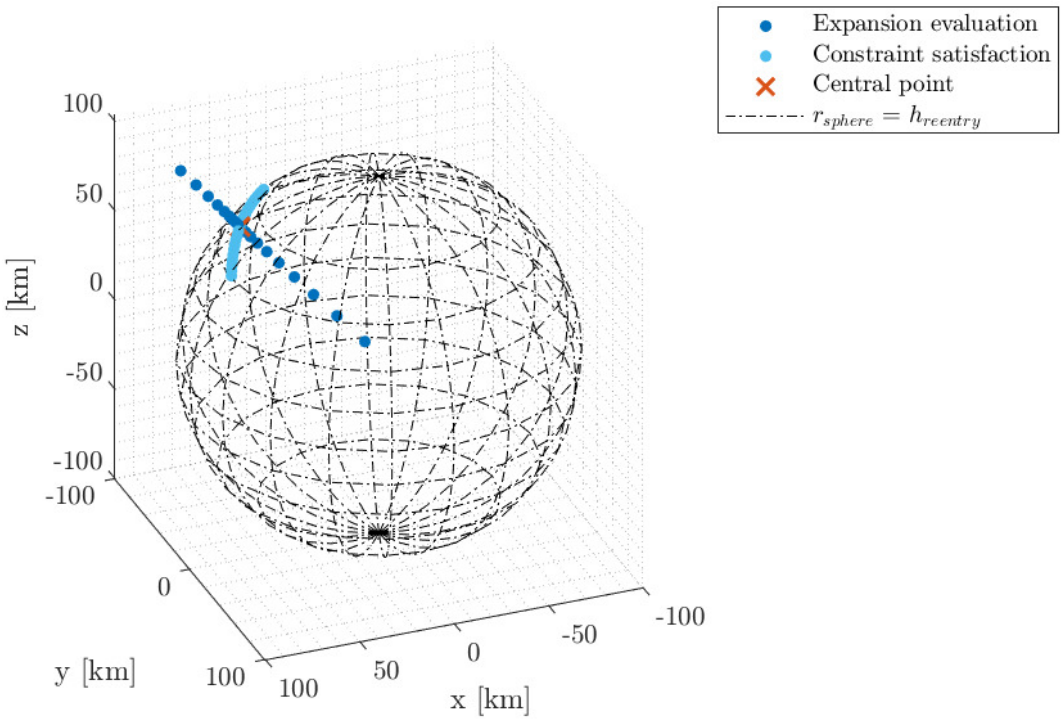

Figure 2.13: Constraint satisfaction, working principle.

the central point (it represents the variable that in the previous section is named t^*). The y axis shows the altitude reached, h. The reference point of the DA expansion is characterised by a $\delta t_f = 0$ s (and $\delta a = 0$ km), since the temporal variable δt_f is a displaced condition, which reference value is the one of the central point, and by $h < 80$ km, namely the re-entry condition. The constraint satisfaction acts by shifting the displaced points from the vertical axis centred in $\delta t_f = 0$, to the horizontal axis passing through $h = h_{re-entry}$. It is interesting to note that a negative displacement causes the point to be below the re-entry altitude at time t_f, in such a way that once the CS is applied, the same point is characterised by a negative δt_f. On the other hand, points with a positive displacement are above the re-entry altitude at the time when the central point reenters, meaning that the CS output time is in the positive half-plane of δt_f.
Another interesting way to illustrate the constraint satisfaction is provided in Figure 2.15. In this case the output of the constraint satisfaction is compared with the result of a Monte Carlo simulation, which points are provided with the same displacements in the initial conditions.

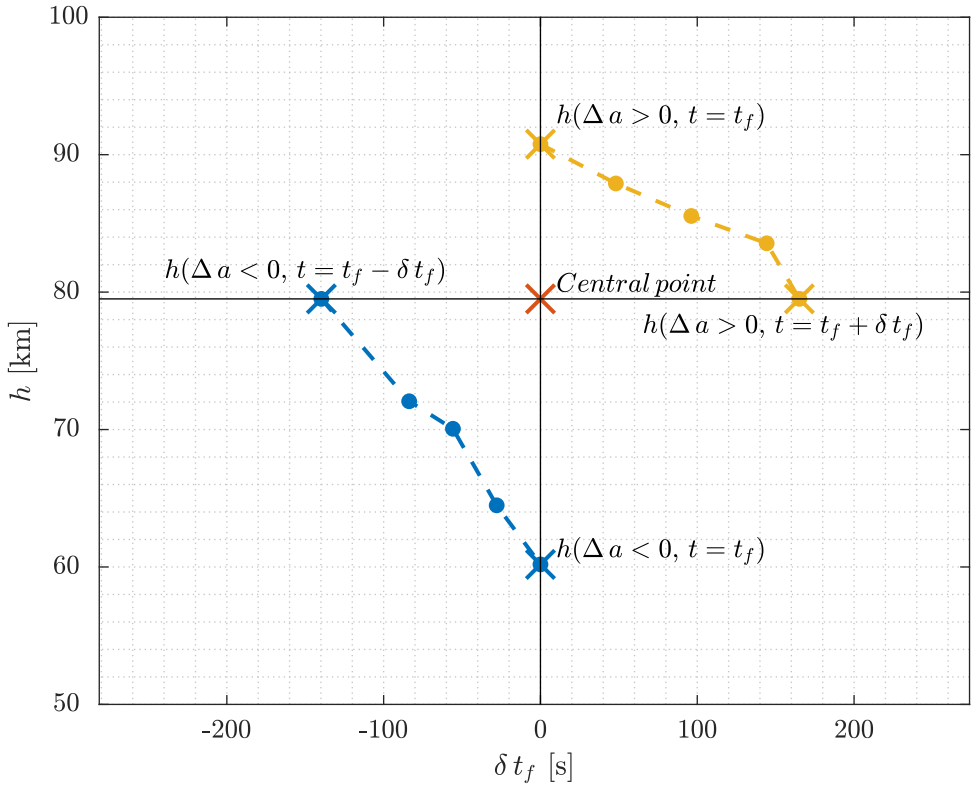

Figure 2.14: Constraint satisfaction, initial and final values with intermediate steps.

Figure 2.15 gives an example of how reentered points are usually distributed: the central point is in the centre, since the initial displacement is applied in both direction. The curve lays on the orbital ground track, or at least in its vicinity. The colour of the points indicate the re-entry time, the darker points are characterised by an earlier re-entry, compared with the lighter ones. There is a complete match between the solution calculated with the numerical Monte Carlo and the constraint satisfaction. This result is the basis for a final consideration on the constraint satisfaction. The DA expansions can suffer from nonlinearities which cause the polynomials to be inaccurate in the limits of the domain. Moreover, the constraint satisfaction requires the inversion of the expansion, which can cause the procedure to diverge. Therefore, in the following analysis, the constraint satisfaction success is measured according to different criteria, which are described where needed. Alternatively, if the displacements used do not exceed the radius of convergence of the DA expansion, not only the constraint satisfaction is able to assure that all the points successfully reenter the Earth's atmosphere at the same desired altitude, it is also

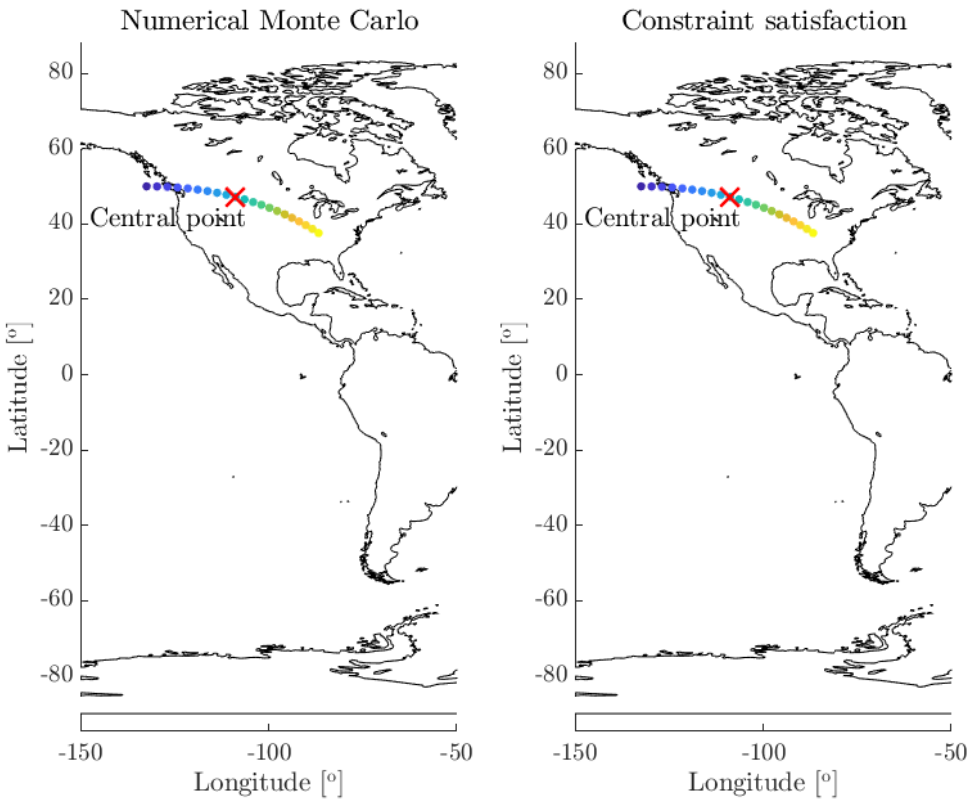

Figure 2.15: Re-entry region, with numerical Monte Carlo and constraint satisfaction.

able to provide a state accurate enough to be compared with the solution given by a numerical Monte Carlo simulation. Thanks to the application of the constraint satisfaction, the differential algebra is an extremely powerful tool, able to perform re-entry simulation campaigns.

Chapter 3

Model validation

This chapter describes some features of the simulation environment created with the DA-based methodology. In Section 3.1, the influence of the DA variables on the DA expansion of each Keplerian element is evaluated. Section 3.2 considers the role played by the DA expansion order on the accuracy and the convergence of the results. In Section 3.3, a detailed analysis of the DA expansion coefficients is provided, which magnitude is proven to be completely dependent on the order of the corresponding expansion. Section 3.4 deals with the effect of the initial semi-major axis and eccentricity on the numerical integration, to define which are the most suitable orbital characteristics to be analysed by the model proposed. Section 3.5 concerns the computational time. Section 3.6 illustrates the automatic domain splitting implementation, involving the influence of the DA order, the maximum number of splits allowed, and the accepted tolerance. Finally, Section 3.7 refers to the study of the uncertainties on the flight path angle, the velocity magnitude, and the azimuth angle.

3.1 DA variables influence

From the current section to Section 3.5, the domain splitting routine is not applied, in order to focus on a single DA integration, and to study the overall behaviour of one polynomial expansion when uncertainties are present.
The DA expansion evaluation has a small region of convergence, where the accuracy with respect to the numerical Monte Carlo is guaranteed. For the following analysis, both the expansion and DA variables are expressed in Keplerian elements. As a first step, the effect of an uncertainty on each element $\{a, e, i, \Omega, \omega, M\}$ is considered separately. Table 3.1 provides a summary of the influence of each DA variable on the DA expansion of the reference point. Note that all the entries marked with a check-mark (✓) are influenced

by the corresponding parameter, the dash (-) characterises all the entries which are not influenced by the DA variable under evaluation, and, finally, the asterisk (*) is used in case the Keplerian element expansion shows a dependence on its own DA variable, but only in the first order term, and the coefficient is the identity 1.

Table 3.1: Influence of DA variables on the resulting expansion.

	δa	δe	δi	$\delta \Omega$	$\delta \omega$	δM
a	✓	✓	-	-	-	-
e	✓	✓	-	-	-	-
i	-	-	*	-	-	-
Ω	✓	✓	✓	*	-	-
ω	✓	✓	✓	-	*	-
M	✓	✓	✓	-	-	*

The inclination i has no influence on the other elements, and vice versa, since it is constant throughout the integration. The reason, as already pointed out, is that drag and Earth's oblateness do not cause any variation of the orbital inclination. Regarding the right ascension of the ascending node Ω, the argument of perigee ω, and the mean anomaly M, they are influenced by the semi-major axis and the eccentricity, but in return they do not have any influence on a and e. Moreover, the variation of the three angles is not caused by the drag, which is the responsible effect of the satellite re-entry. Their variation, as illustrated in Chapter 2, is due to the gravitational perturbation generated by the J_2 effect. Therefore, the semi-major axis and the eccentricity are the only parameters that are worth to analyse deeply.

3.1.1 Simulations to test the influence of δa and δe

The eccentricity and the semi-major axis are both heavily affected by drag, which causes the orbit to circularise while decaying, constantly reducing its altitude. Since slight variations in the eccentricity do not cause major changes in the orbital altitude, a displacement in the semi-major axis is expected to affect the results, and the DA convergence radius, more than a variation in the eccentricity.
Two different numerical experiments have been performed to analyse the model dependency on those variables. Firstly, Figure 3.1 shows the maximum displacement in a and e that guarantees the convergence for different initial values of altitude h_0 and eccentricity

e_0. The side bar provides the displacements applied in a and e, in percentage of the initial value, in order to compare Figure 3.1a and Figure 3.1b. The magnitude of the numbers involved clearly shows that a displacement in the semi-major axis is more restrictive, since the maximum Δa allowed is only 0.01% of a_0, and the minimum is 10^{-6}%. Instead, considering Figure 3.1b, the maximum Δe that can be applied is 10% of e_0, which is three orders of magnitude higher than the same entry in previous case, and the minimum is the 0.0001%.
For the second test, the initial orbital state is given Table 3.2. In Figure 3.2, fixed dis-

Table 3.2: Initial state for the validation of the model.

h_0 [km]	e_0 [-]	i_0 [°]	Ω_0 [°]	ω_0 [°]	M_0 [°]
150	0.001	45	0	0	0

placements are considered, ranging from 10^{-6} to 0.01% of the initial a_0 and e_0. They are applied separately to show how the resulting δt_f from the constraint satisfaction, diverges earlier in the case of a variation applied on a (blue curve), compared with the same displacement applied on the eccentricity e (yellow curve). Circles in red show the points for which the constraint satisfaction was not able to provide an accurate estimation of the re-entered point. The scale of the plot is logarithmic on both axes.
Concluding, the major finding is that the influence given by the semi-major axis is more relevant than the one in the eccentricity. For this reason, in the following sections only uncertainties in a will be considered.

3.2 Expansion order analysis

Differential algebra is an approximation of functions through Taylor series. Therefore, an higher DA order should correspond to a more precise representation of the real variables. Unfortunately, within the present work, the DA expansion do not behave as expected. Since the first simulations, it has been clear that for higher orders the DA expansion was completely inaccurate, while lower orders not only were able to better represent the exact solution, but they even guaranteed the use of higher displacements in the initial condition. A possible reason behind this peculiar and unforeseeable behaviour is presented in Section 3.3.

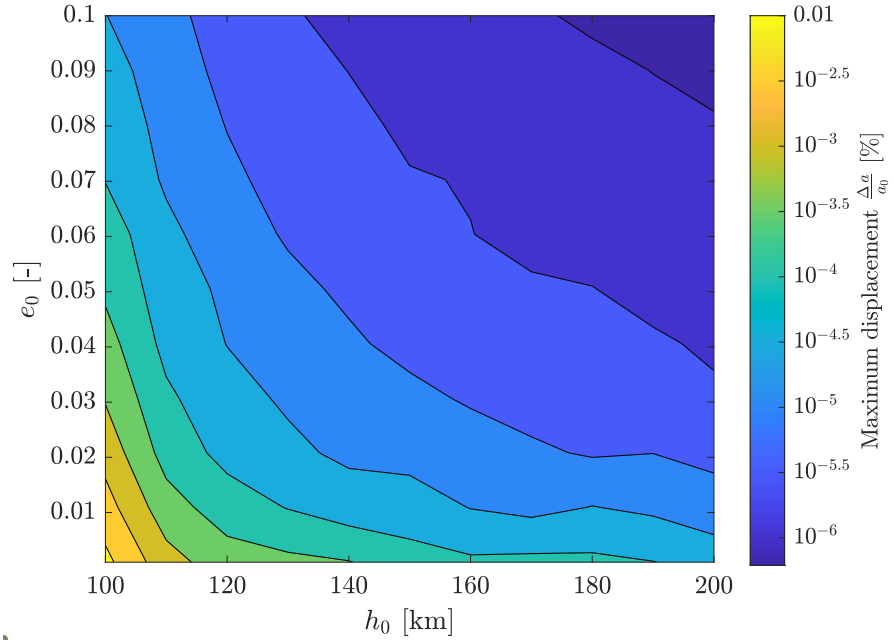

(a) Influence of the parameter a

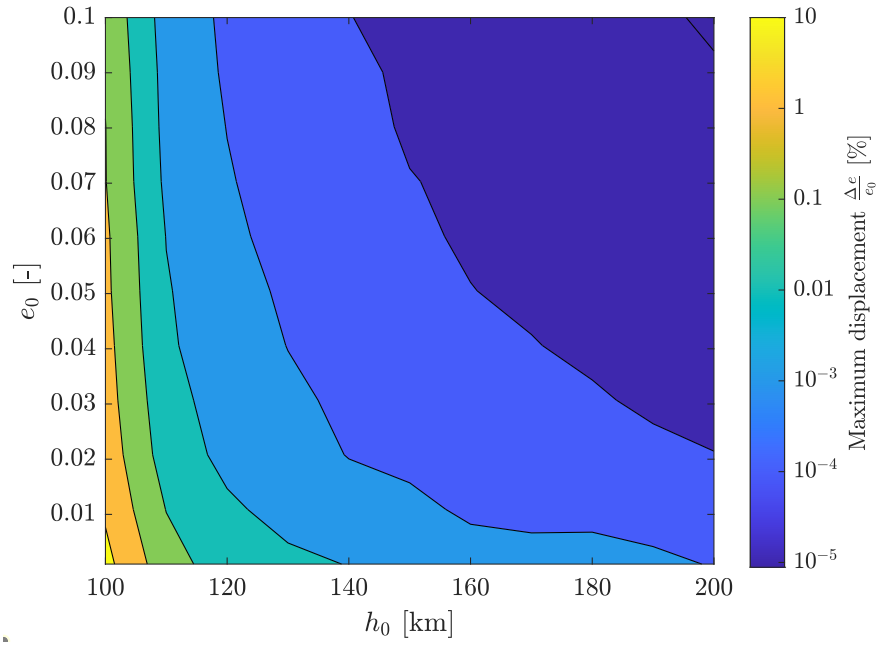

(b) Influence of the parameter e

Figure 3.1: Maximum displacement in a and e to guarantee the expansion convergence.

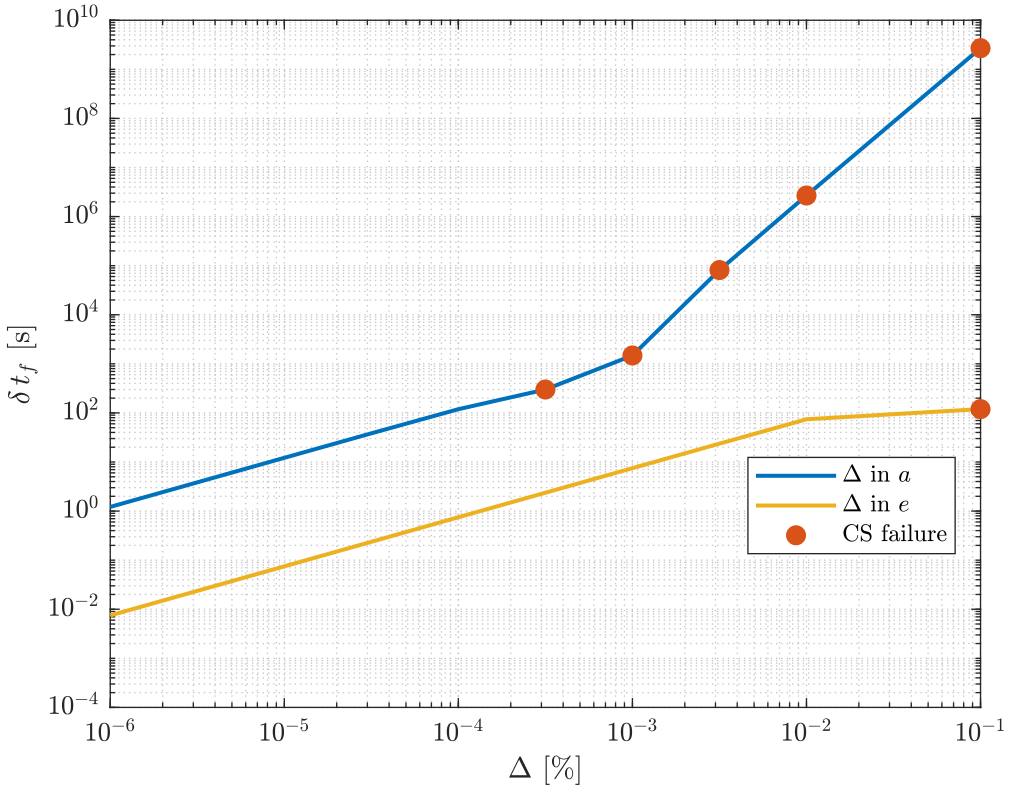

Figure 3.2: Influence of the same Δ [%] in a and e on the $\delta\, t_f$.

3.2.1 Results on the DA order analysis

Concerning the DA expansion, a first analysis consists in the comparison of the DA orders over different re-entry altitudes. The quantity used for the comparative study is the maximum displacement allowed. The scope consists in proving in which way low and high orders behave differently.

The final altitude range is chosen between 80 km and 120 km. Initial conditions are provided in Table 3.2. The expansion is assumed to converge when the maximum difference between the re-entry altitude of the central point and the output altitude from the application on the CS, is below 5 km

$$\Delta\, h_f = |h_{CS} - h_{central\,point}| < 5\,\text{km} \tag{3.1}$$

Figure 3.3 shows that the maximum Δa that can be applied is almost perfectly symmetric for negative and positive displacements. For high altitudes, as 120 km, the polynomial expansion converges for a displacement of about 1000 m. Although, as the altitude reduces, higher orders are characterised by an important tightening of the allowed displacement,

amounting, for order 6, to only 1 m at a final altitude of 80 km. Lower orders are less affected by the re-entry.
A second analysis consists in the study of the spatial position error and the maximum

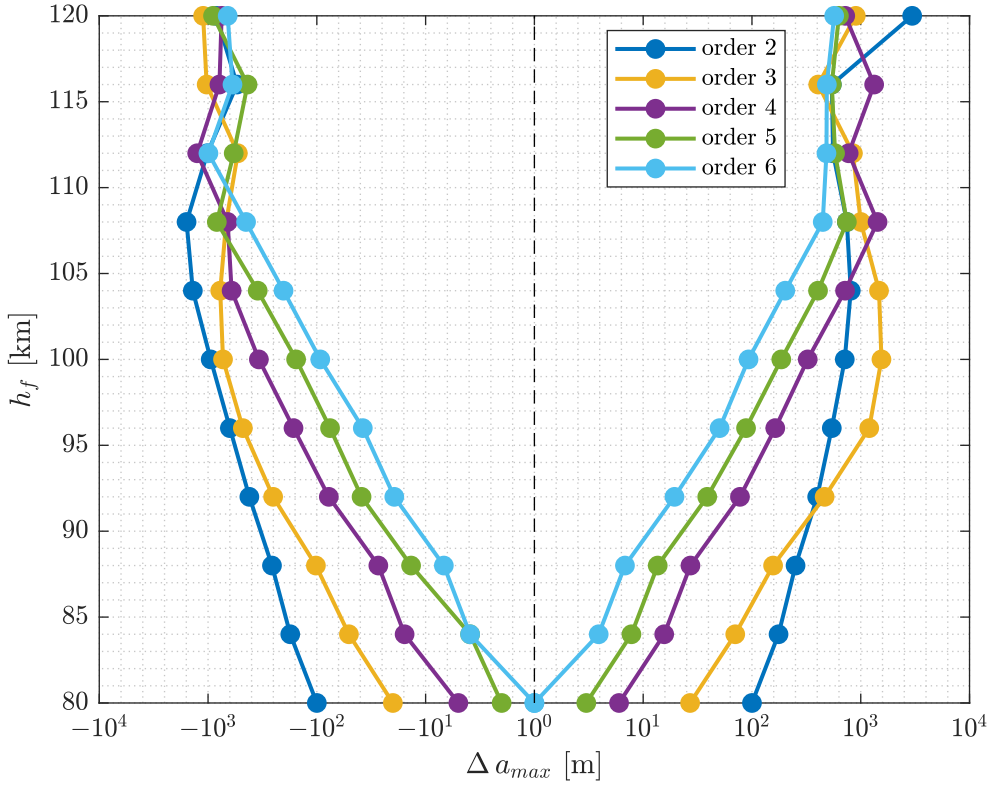

Figure 3.3: Maximum Δa needed for the CS convergence, for different orders and h_f.

displacement allowed by all the orders from 2 to 6, with respect to various final altitudes. The initial state is in Table 3.2. Considering Figure 3.4, the red line represents the maximum displacement which is determined by the less converging DA expansion, depending on the altitude. Clearly, as the altitude reduces, the Δa_{max} reduces as well. The figure provides the trend of the spatial position error, expressed in meters, versus the re-entry altitudes from 80 km to 120 km, for the DA orders 2, 3, 4, 5, and 6. Figure 3.4a and Figure 3.4b refer to negative and positive displacements in the semi-major axis, respectively. The two results are roughly symmetric. In fact, it is noticeable how the absolute value of the maximum Δa applicable is almost the same in the two cases. For high altitudes the error of orders 6 and 5 is the lowest, while order 2 experiences the highest error. This is consistent with what expected, since higher orders are supposed to provide a better approximation. Although, for lower altitudes, from 110 km to 80 km, higher orders are

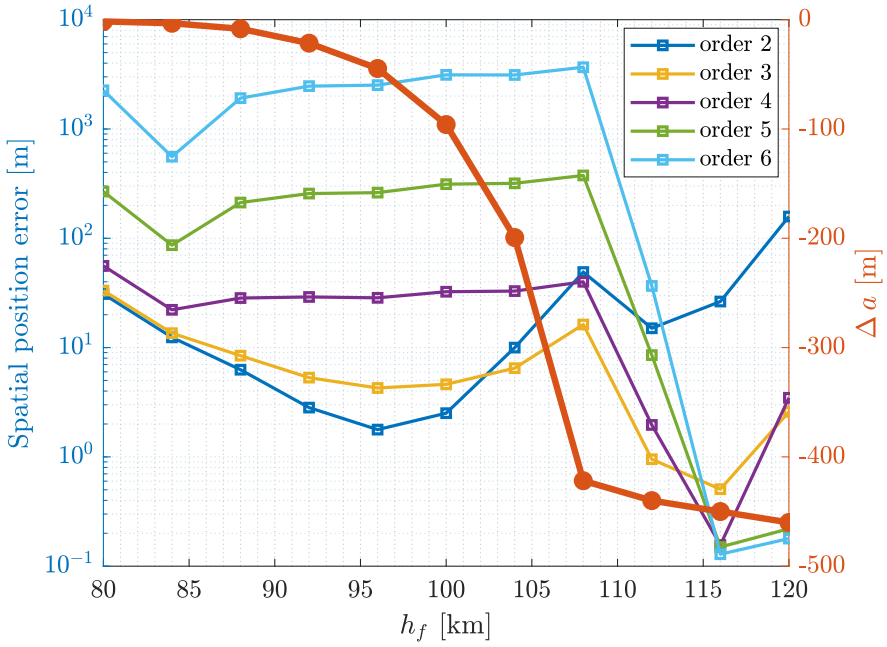

(a) $\Delta a < 0$

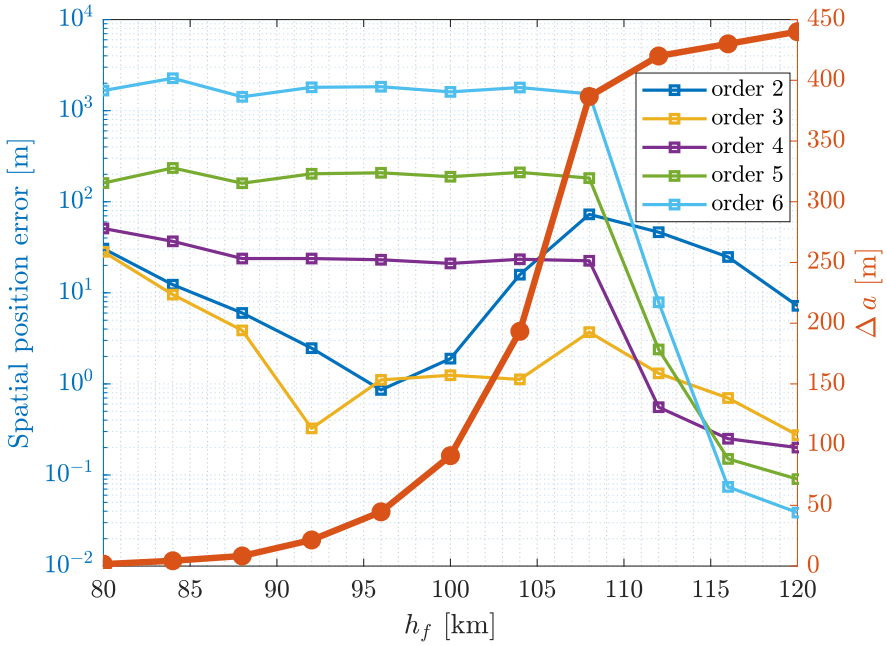

(b) $\Delta a > 0$

Figure 3.4: Spatial position error and Δa for different final altitudes, from order 2 to 6.

penalised, while order 2 and order 3 are more accurate.

3.3 DA expansion coefficients

To understand the reasons behind the distinctive behaviour of the DA expansion as the order varies, an analysis of the expansion itself is required. The study considers the evolution of the coefficients throughout the integration. The coefficients of the four angles, i, Ω, ω and M do not diverge during the integration. On the contrary, the expansions of a and e are particularly interesting, since the order of magnitude of the high order coefficients, especially for the semi-major axis a, are enormous, exceeding 10^{40}. This effect is predictable, as it is caused by the fact that, as the propagation proceeds, the polynomial is not able to cover all the uncertainty domain with enough accuracy. Therefore, the implementation of the domain splitting technique will be proven fundamental to properly propagate an initial orbital state up to the re-entry within the atmosphere.
Although the domain splitting procedure is able to avoid the issue, some tests have been performed to describe why numerical nonlinearities affect the propagation so deeply. A first hypothesis, which has been proven wrong lately, was that the reason behind the divergence of high order expansions was caused by a reduction in the eccentricity, which approaches zero when the spacecraft is close to the re-entry altitude. In fact, $e = 0$ is a singularity condition for the mathematical model used. For this reason, circular orbits cannot be considered in the present work as they would require the use of different orbital elements. This possibility is discussed in Chapter 5.

3.3.1 Analysis of the evolution of the coefficients

To explain the divergence of the DA expansion using high orders at low altitudes, the starting point has been to study three simple cases. For the tests, only the expansion of the semi-major axis a has been taken into account, since it is the variable that usually diverges first. For all the orders, only the coefficients relative to δa are reported, since no variation is applied to the other DA variables.
Table 3.3 provides the initial conditions, in terms of h_0 and e_0, the final altitudes h_f, and the final propagation times t_f, for the three cases.
In Figure 3.5, the dotted red line represents the value of the highest coefficient throughout the integration. In the beginning, coefficient magnitudes scale with the inverse of order, order one being the highest. During the integration, the coefficients follow an exponential growth and at a given point their values become proportional to the DA order, thus diverging.

Consider Figure 3.5a and Figure 3.5b, the initial altitude is the same ($h_0 = 150$ km), but the eccentricities differ of two orders of magnitude. For Case 2, the coefficients of the semi-major axis a are higher than the expansion coefficients of Case 1, despite the eccentricity is much higher in the former. This disproves the initial hypothesis, for which the eccentricity should have been the responsible variable causing the DA expansion to diverge.

Another valid hypothesis is that the divergence is induced by longer integration times, as it occurs in the test comparison between Case 1 and Case 2.

Therefore, another comparison considers Case 1 and Case 3, as provided in Figure 3.5a and Figure 3.5c. The coefficients in Case 3 are several order of magnitude lower than the coefficients of Case 1, which exceed 10^{20} at the peak, rebutting also the last hypothesis.

The first three cases confuted the hypothesis formulated to explain the behaviour of the

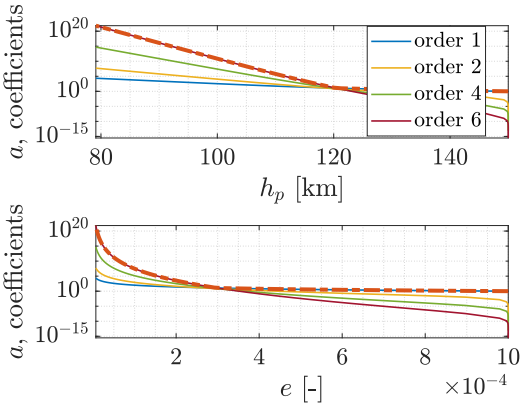

(a) Case 1

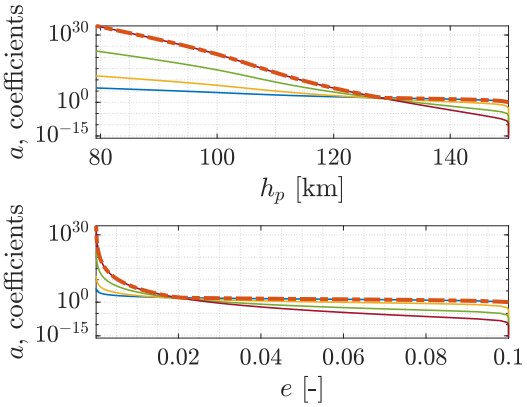

(b) Case 2

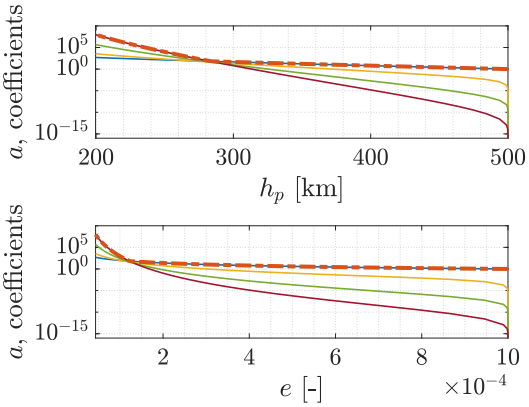

(c) Case 3

Figure 3.5: Expansion coefficients of a with respect to h_p and e, for the three cases.

expansion coefficients. Another test is based on the orbit which initial conditions are

Table 3.3: Initial conditions (h_0, e_0), and final altitude and time (h_f, t_f).

	h_0 [km]	e_0 [-]	h_f [km]	t_f
Case 1	150	0.001	80	16.32 *hours*
Case 2	150	0.1	80	127 *days*
Case 3	500	0.001	200	16 *years*

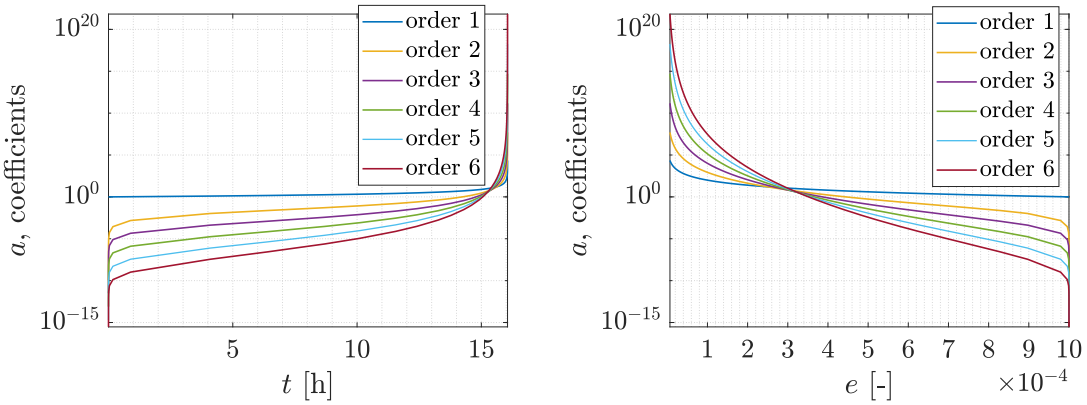

(a) With respect to time

(b) With respect to the eccentricity

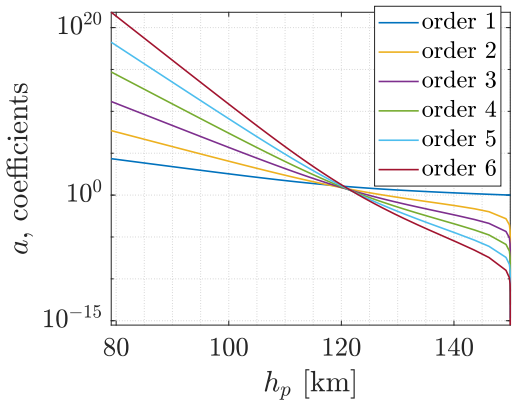

(c) With respect to the altitude of perigee

Figure 3.6: Expansion coefficients of a according to different features of the integration.

provided in Table 3.2. The idea is to study the trend of the coefficients with respect to some relevant features of the propagation, which include the integration time, the eccentricity, and the altitude of perigee. Results are in Figure 3.6. The three figures are semi-logarithmic plots with respect to the y axis.

Considering the coefficients evolution with respect to time (Figure 3.6a) and with respect to the eccentricity (Figure 3.6b), no relevant trend is recognised.
However, Figure 3.6c shows that the increase of the DA expansion coefficients with respect to the altitude of perigee is almost linear in the logarithmic scale. The portion close to 150 km, where the higher order coefficients are gradually generated, is excluded, since it is the nominal creation of higher order terms. This growth can be the key to understand the cause behind the coefficients divergence. In fact, in Figure 3.7, it is shown how the linear trend between the altitude of perigee and the DA expansion coefficients of a does not appear anymore when the density ρ is a double-precision quantity, instead of a DA object. The trends for the coefficients of order 5 and order 6 are not visible because the two coefficients are constantly equal to zero. The density model, provided in Equation (2.33), is exponential, and this explains the linear trend in the semi-logarithmic scale.
Concluding, the divergence of the coefficients seems to be caused by the nonlinear density model used. This explains why for Case 1 and Case 2 the altitude, at which the coefficient of order 6 starts to rapidly increase, is almost the same (between 120 and 130 km), and also why the order of magnitude of the coefficients in Case 3 is limited. Indeed, the altitude of perigee is higher, and consequently the density is smaller, playing a less relevant role.
As a final illustration, Figure 3.8 proposes the same figure as in Section 3.2 (Figure 3.3),

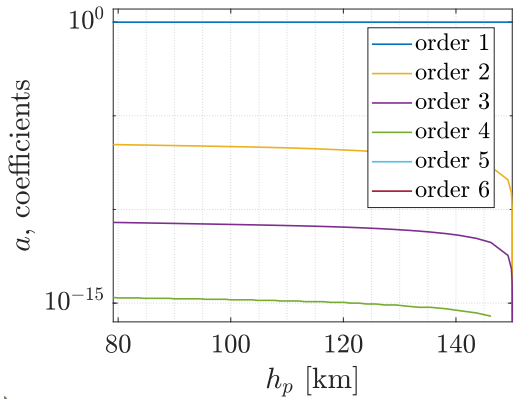

Figure 3.7: Expansion coefficients of a when ρ is a double precision variable.

with the addition of the side bar providing the order of magnitude of the highest expansion coefficient of a, for different final altitudes h_f and DA orders. Clearly, an higher coefficient is associated with a smaller Δa. The gap between the order of magnitude of the DA coefficients for high re-entry altitudes and for low re-entry altitude is huge, especially when considering order 6. In this case, indeed, the highest coefficient grows from 10^2 to 10^{20}, with a difference of 18 orders of magnitude.

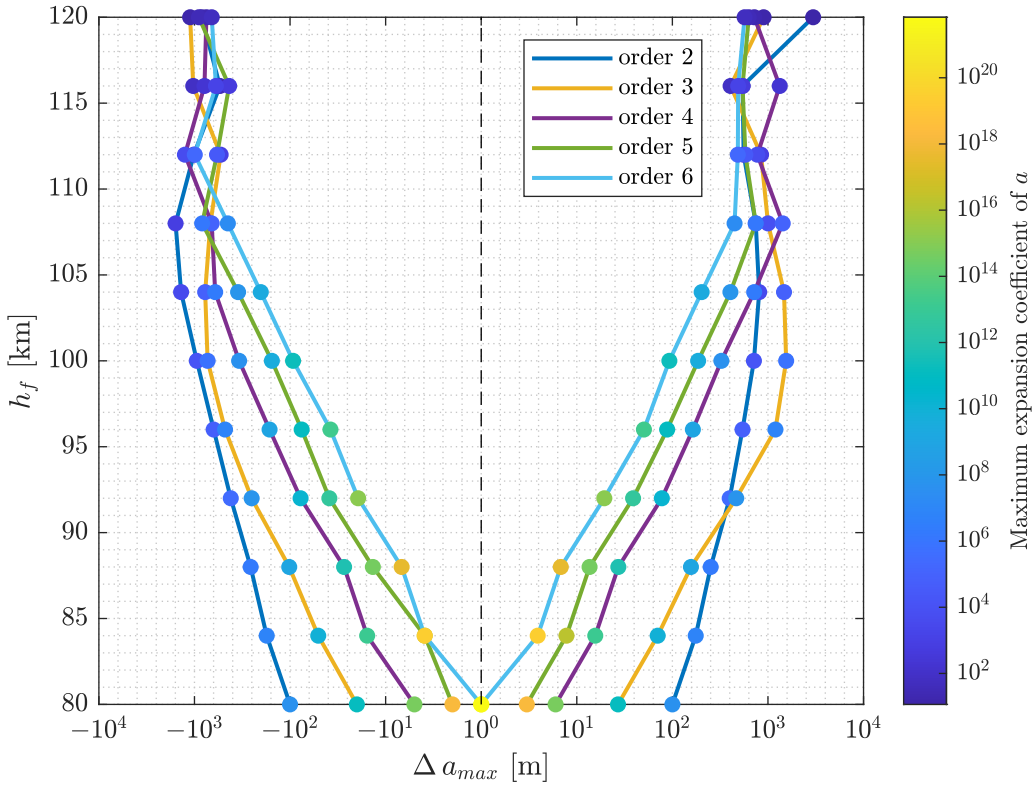

Figure 3.8: Figure 3.3 with side bar related to the expansion coefficient.

3.4 Orbit characteristics

The principal aim of this section is to provide some indications concerning which would be the most appropriate class of catalogued objects to validate the DA-based methodology proposed. The expression orbital characteristics refers to the ranges of initial conditions which would be able to provide a good convergence of the method, with reasonable values of the displacements used. The two variables that will be investigated are the initial altitude h_0 and the initial eccentricity e_0, since, as already discussed, the other elements are not influencing the results in a relevant way. For this reason, pairs of (h_0, e_0) are tested with the scope of comparing the maximum displacement that can be applied.

3.4.1 Comments on the numerical Monte Carlo framework

The Monte Carlo method requires a full integration to propagate each displaced state. Its solution is thus considered as the exact one, and used as the reference to test the

accuracy of the DA-based methodology.
In order to compare the two solutions, the numerical Monte Carlo integrator must be supplied with a stopping condition. In Figure 3.9, two versions of the criterion used in the numerical Monte Carlo analysis are presented, one is based on the re-entry altitude (Figure 3.9a), which requires the implementation of an event function, the other on the re-entry time (Figure 3.9b). Both are valid and provide the same results.

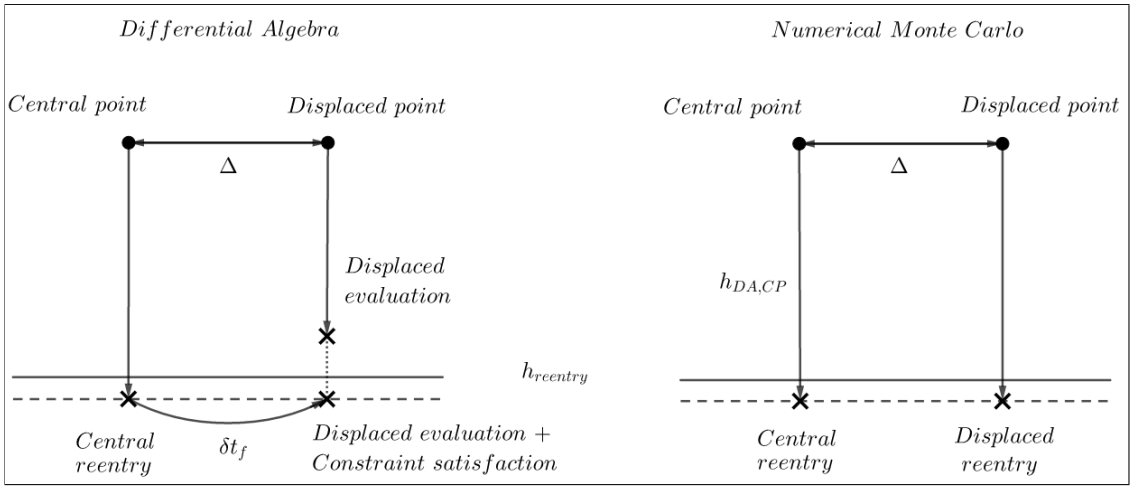

(a) Re-entry altitude condition

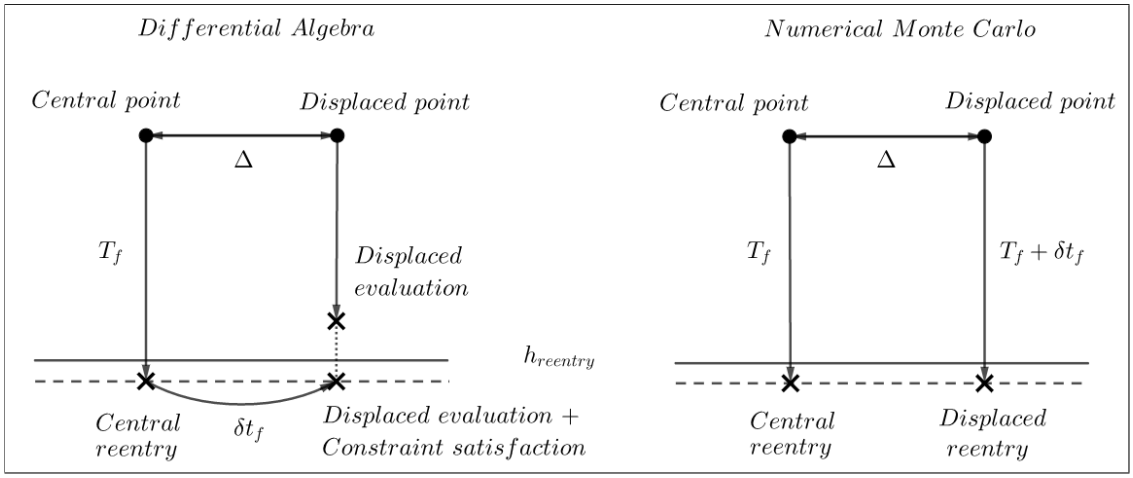

(b) Re-entry time condition

Figure 3.9: Numerical Monte Carlo stopping criteria.

3.4.2 Analysis based on pairs of h_0, e_0

The analysis is performed using a DA order equal to 4. The trade-off behind the choice regards the expected accuracy and the maximum Δa used. In fact, higher orders require

a displacement of the order of 1 m, while lower orders are not reliable enough, especially because their region of accuracy is small. The nominal re-entry altitude is 80 km.
The procedure to compute the results for each pair (h_0, e_0) is iterative, and shown in

Table 3.4: Data for the contour plot on the initial values h_0 and e_0.

$h_{0,max}$ [km]	$h_{0,min}$ [km]	$e_{0,max}$ [-]	$e_{0,min}$ [-]
200	100	0.1	0.001

Algorithm 6. The algorithm increases the Δa in case of convergence, and halves it if the condition in Equation (3.2) is not satisfied.

$$10\,\text{km} < h_{CS} - h_{central\,point} < 5\,\text{km} \tag{3.2}$$

Figure 3.10, shows the results obtained using data in Table 3.4. The two side bars pro-

Algorithm 6: Algorithm for the iterative procedure in Section section 3.4.

Data: Inverse function from the constraint satisfaction $\mathbf{F}^{-1}$, final condition of the central point $x_{f,CP}$, and its final re-entry altitude $h_{central\,point}$.
Result: Maximum displacement allowed, Δa_{max}.

```
initialisation;
define the maximum number of iterations it_max;
define initial Δ a_0;
while maximum number of iterations is not exceed and maximum Δa is not found do
    calculate δ t_f;
    calculate the state of the displaced point x_{f,CS};
    calculate the displaced point altitude h_CS;
    if the threshold in Equation (3.2) is not exceeded then
        update Δ a_{n+1} = Δ a_n · 1.5;
    else
        update Δ a_{n+1} = Δ a_n/2;
        update the number of failed iterations;
    end
    return Δ a_max;
end
```

vide the maximum displacement, obtained with positive (Figure 3.10b), and negative Δa (Figure 3.10a). Low initial altitudes and low eccentricities allow for displacements up to 350 m in both directions, while high h_0 and high e_0 are the most disadvantageous, since

the maximum Δa applicable is less than 1 m.
Concluding, orbits characterised by low initial altitude and low eccentricity are the most suitable. Nevertheless, to impose a reasonable displacement in the initial condition, the implementation of the domain splitting procedure is absolutely necessary.

3.5 Computational time

Differential algebra allows to reduce the running time of a simulation campaign. The Monte Carlo approach is often referred as a brute-force methodology, although, it is usually the only possible instrument to proceed with the propagation of the uncertainties involved in the re-entry problem. For the study of the running time a HP laptop 8GHz Intel Core i7 is used.
In the differential algebra framework, due to the number of terms involved, the computational time of higher orders is moderately greater than the one of lower orders. The running time of the DA propagation is the major contribution. The evaluation of the final expansion for the displaced states is of minimal importance, since it consists in a simple polynomial evaluation. The numerical Monte Carlo, instead, requires the complete integration of each set of displacements. In this section, the break even point according to certain initial and/or final conditions is provided, for different DA orders. It can be anticipated that the break even point increases with the order, since the integration of the reference point requires more time as the DA order increases.

$$t_{MC} = \bar{t}_{MC} \cdot n \tag{3.3}$$

$$t_{DA,\,fixed} = t_{CP} + t_{CS,\,fixed} \tag{3.4a}$$

$$t_{DA,\,variable} = \bar{t}_{CS,\,variable} \cdot n \tag{3.4b}$$

$$B/E = \frac{t_{DA,\,fixed}}{\bar{t}_{MC} - \bar{t}_{DA,\,variable}} \tag{3.5}$$

Equation (3.3) defines the numerical Monte Carlo computational time, which is given by the average time for one integration multiplied by the number of points propagated. Equation (3.4a) is used to compute the fixed time of the DA propagation. It includes the integration time of the reference condition, plus the fixed contribution of the constraint satisfaction routine. The variable component of the DA propagation (Equation (3.4b)) only considers the evaluation of the polynomial, with respect to the displacement imposed. The formula for the break-even point is in Equation (3.5).

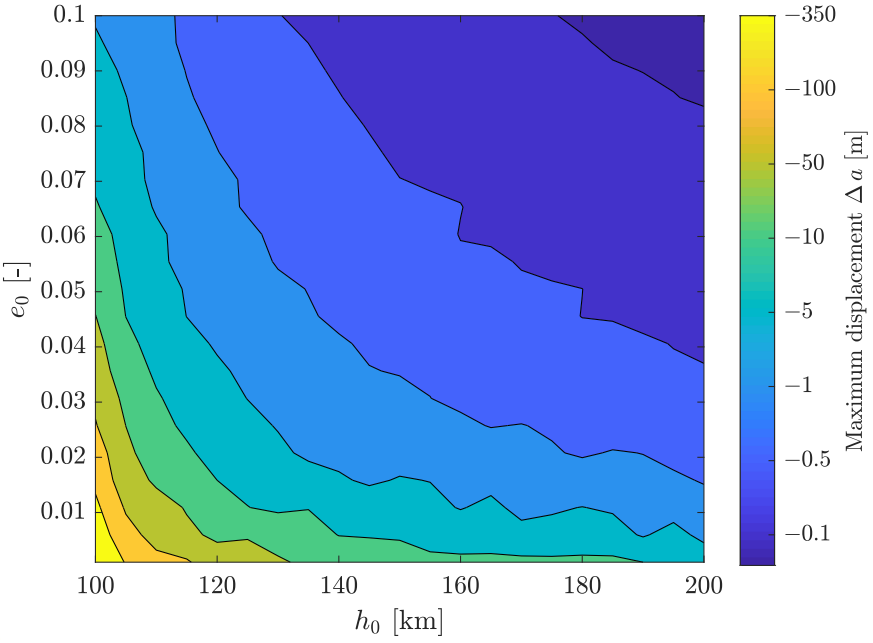

(a) $\Delta a < 0$

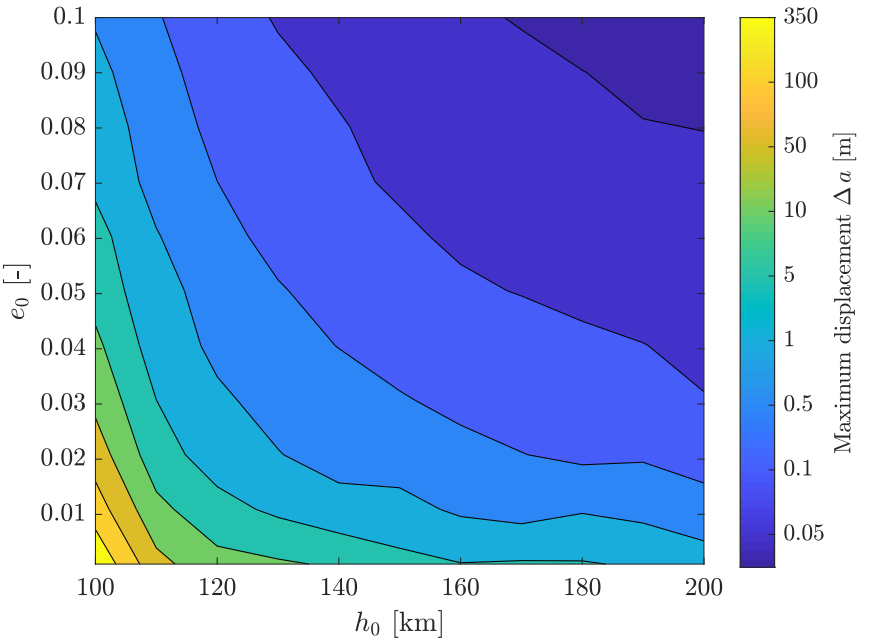

(b) $\Delta a > 0$

Figure 3.10: Contour plot for each pair of h_0, e_0.

3.5.1 Running time analysis

The computational time analysis here provided studies how the break even point evolves according to the DA order. The initial conditions are in Table 3.2, and are fixed throughout the analysis, the re-entry altitude is set to 80 km. Considering Figure 3.11, the Monte Carlo running time is represented by the dotted line in red, it crosses the curves of the DA orders at different numbers of evaluations. In the upper figure, the break even point is highlighted for each DA order.
As expected, the break-even point shifts right as the DA order increases. Even with or-

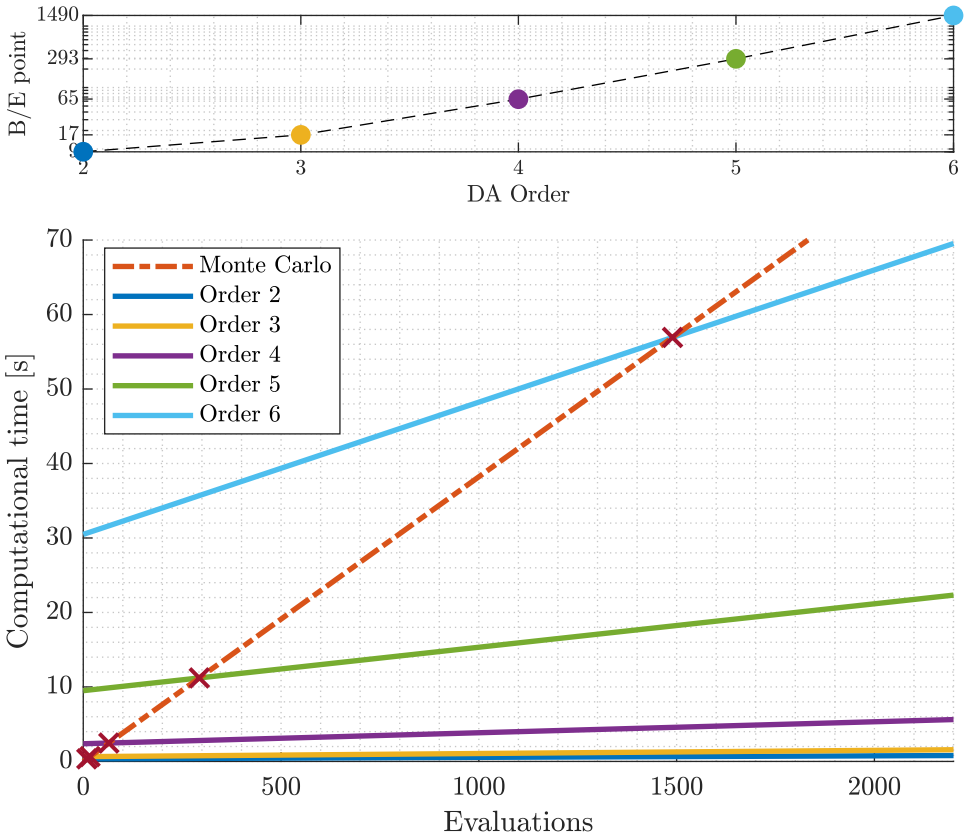

Figure 3.11: Break-even point and computational time.

der 6, the advantage given by the DA over a classical Monte Carlo simulation is clear. Provided that the range of the uncertainties is small enough to have a good convergence of the DA, when the number of simulations to be completed is about 1500, the DA successfully allows to reduce the computational time.

3.6 Automatic domain splitting implementation

The automatic domain splitting procedure mitigates the effect of nonlinearities in the dynamics. The present section deals with the implementation of the technique in the model developed for the thesis. Firstly, it is discussed how the automatic domain splitting can be applied to the re-entry problem, and which are the main challenges. Then, the influence of the key parameters, namely the DA order, the maximum number of splits allowed, and the accepted tolerance, is presented.

3.6.1 Application to the re-entry problem

The re-entry problem is particularly demanding in terms of computational efforts. The main reason is that during the re-entry, the spacecraft experiences a rapid transition from the orbital equilibrium phase to a chaotic dynamics, which cannot be considered anymore as an orbital trajectory. During this phase, the equations of motion are particularly sensitive, and the spacecraft altitude is substantially reduced in an extremely short time.
The Taylor expansion of the DA variables are heavily affected by the nonlinearities arising during the re-entry. In fact, the expansion coefficients magnitude increases as an exponential. The reason is discussed in Section 3.3, and it lies in the mathematical formulation of the atmospheric profile, which is described by means of a summation of exponential functions. When the spacecraft reaches altitudes below 100 km, the density sharply increases, causing the coefficients to explode. The domain splitting technique is beneficial in the re-entry problem, since nonlinearities are better approximated dividing the expansion when the desired accuracy is lost.
Although, the re-entry phase is so critical that the domain splitting procedure is continuously applied, resulting in thousands of polynomials, each valid in a subdomain which is an infinitesimal fraction of the original uncertainty interval. Figure 3.12 provides a visual aid to explain what happens during the integration of the propagation of an object re-entering the Earth. Both figures are relative to the first domain. The choice is arbitrary, but without loss of generality. The estimated norm results from the exponential fit based on the summation of the coefficients relatively to each DA order. The norm is the approximated value of the coefficients of order $n + 1$, where n is the chosen expansion order. The evolution of the norm, in the semi-logarithmic scale, and the mean altitude are represented with respect to the integration time. At each iteration, the estimated norm is compared with the value of an accepted tolerance, when it is exceeded, a split occurs, and the norm reduces. A detailed discussion concerning the splitting procedure is provided in Section 2.5. The small jumps in the mean altitude are inevitably caused by the change from one set of orbital parameters to another. In fact, at each split, the

reference condition of the current expansion is displaced.
Figure 3.12a provides the trends of the estimated norm and mean altitude for an orbit propagated from 120 km to 80 km. At around 100 km altitude, few seconds before the re-entry at 80 km, the split rate is too high to distinguish each curve.
Therefore, the upper part of Figure 3.12b provides a zoom on the phase between 100 and 80 km. While the lower part shows the results for a propagation from 100 to 80 km. The two, are named Case 1 and Case 2. Table 3.5, provides the initial states for the two cases. The object used is the Phobos Grunt spacecraft, which re-entered the Earth's atmosphere on January 15$^{\text{th}}$, 2013, after a failure in the propulsion system[1]. The two initial states provided are not retrieved from existing TLEs, but they result from a propagation of a certain TLE state up to the desired altitudes, 120 and 100 km, respectively.
In Table 3.6, the results of the numerical integration of Case 1 and Case 2 are shown. In

Table 3.5: Initial state for the study of the domain splitting applied to the re-entry problem.

	a [km]	e [-]	i [°]	Ω [°]	ω [°]	M [°]
Case 1	6495	0.000490	51.41	351.37	309.46	203
Case 2	6478	0.000120	51.41	351.30	309.51	274.2

the present analysis, no limit on the size of the subdomain is imposed, and the splitting is never interrupted. This results in almost 30,000 splits for Case 1, while for Case 2 the number reached is 99. It is also remarkable that the spacecraft takes 21 minutes to re-enter from an altitude of 120 km, while from an initial altitude of 100 km it only needs 64 seconds. Together with the figures, those results prove the severity of the re-entry problem for the mathematical integration.
Figure 3.12b, illustrates that the norm increases linearly in the semi-logarithmic scale. As

Table 3.6: Propagation results for the domain splitting implementation.

	N. of domains	Re-entry time (domain 1)
Case 1	28995	21 min
Case 2	99	1 min

[1]NASA website, *Solar system exploration*: `https://solarsystem.nasa.gov/missions/phobos-grunt/in-depth/`, accessed: 13/05/2020.

the spacecraft re-enters, the norm reduces less after each split, and the split rate accelerates. The slope of the segments is expressed in decibel (dB) per second, and the slope evolution for the two cases is provided in Figure 3.13. Throughout the re-entry, the slopes sharply increase, resulting in a raise of the number of splits. For the rest of the analysis, the maximum number of splits is limited, therefore, a minimum size of the subdomain is imposed.

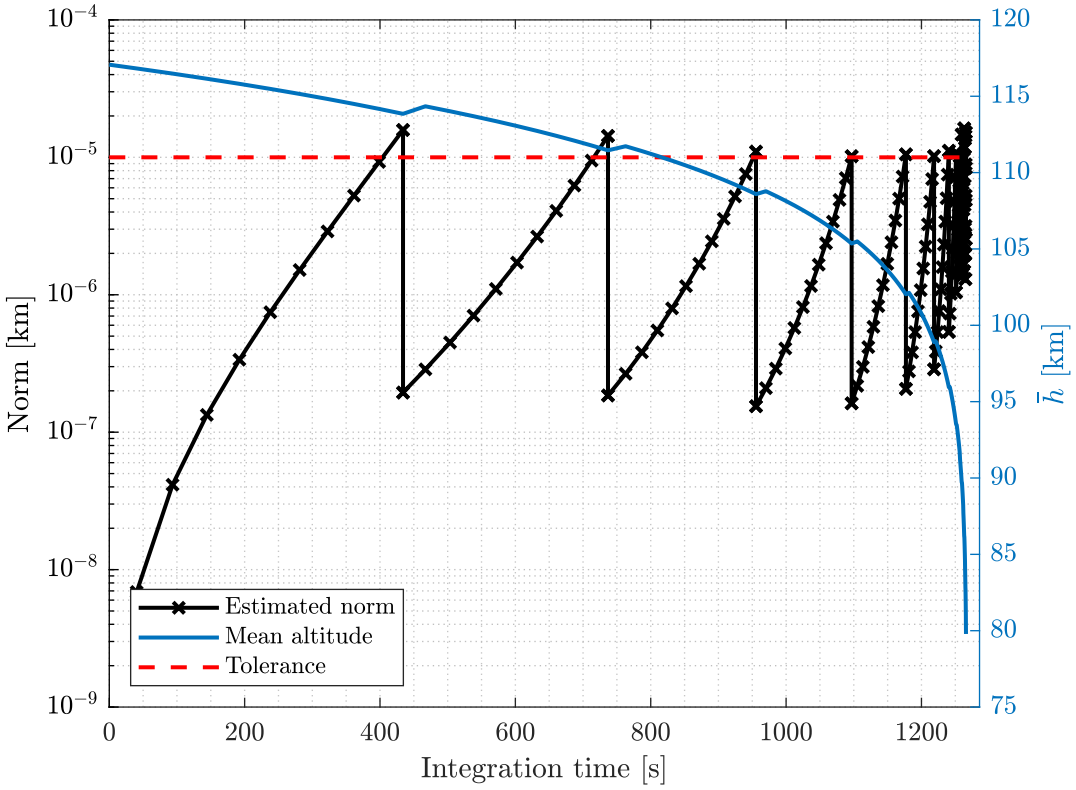

(a) From 120 to 80 km

Figure 3.12

3.6.2 Influence of the key parameters

The following paragraphs deal with the influence of the domain splitting algorithm parameters. For the discussion, two real re-entered objects are used. The initial states are retrieved from the publicly available TLEs, and re-entry is expected between few hours to few days, depending on the uncertainties applied. The scope is to test the model proposed for low and highly eccentric orbits. The two spacecrafts are the Chinese space

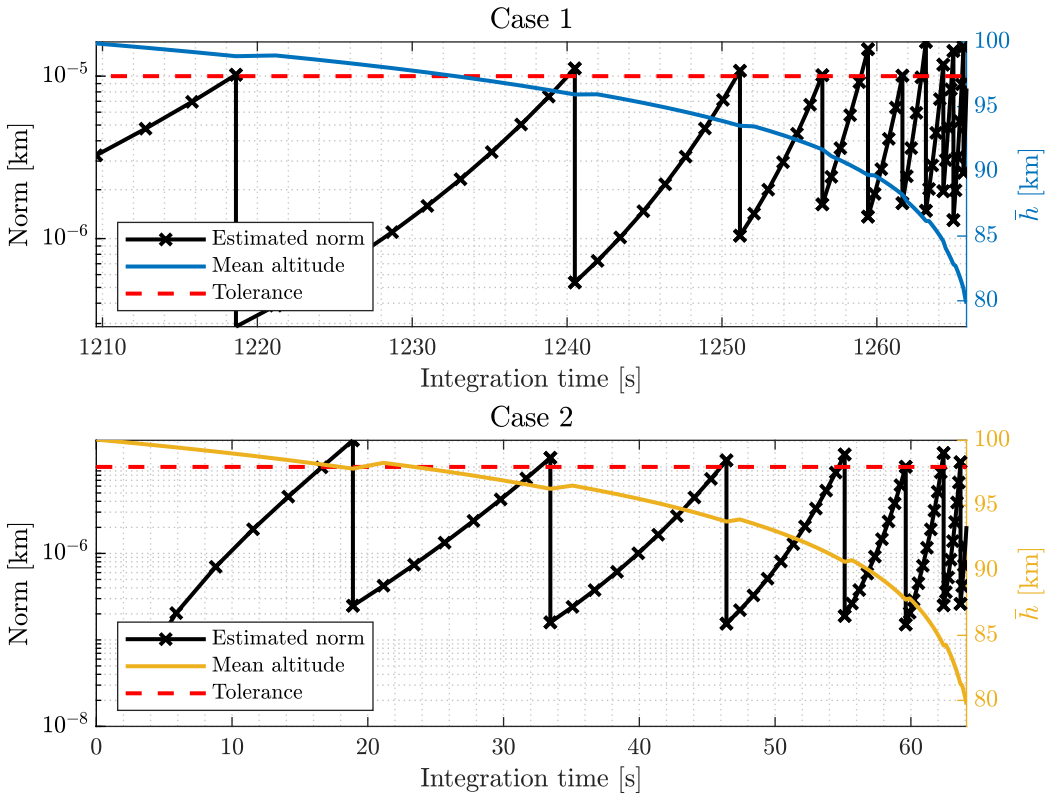

(b) From 100 to 80 km

Figure 3.12: Norm evolution during the integration, for different starting altitudes.

station Tiangong-1, and a spent rocket stage in GTO orbit, GSLV R/B. Table 3.7 provides the initial states and epochs for the two spacecrafts.

The Tiangong-1 (NORAD 37820) was launched the 29$^{\text{th}}$ September 2011 in an almost circular orbit in LEO, the control of the station was lost in 2016, and the gradual decay lasted until the 2$^{\text{nd}}$ April 2018, when it reentered the Earth's atmosphere over the South Pacific Ocean. A more detailed analysis about the Tiangong-1 re-entry is provided in Chapter 4.

Geostationary Transfer Orbits (GTOs) are mostly occupied by spent rocket bodies, which exhausted their propellant tanks to transfer satellites from Low Earth Orbits (LEOs) to geostationary orbits (r_{GEO} = 42,168 km). The re-entry of rocket stages can potentially constitute a risk for the population, due to their mass and the materials used for the tanks, which can survive the re-entry within the atmosphere. The chosen object, GSLV R/B (NORAD 39499), is taken from a list of GTO spacecrafts provided by Gondelach et al. [2016], where it is used to validate the tool developed to predict the re-entry of

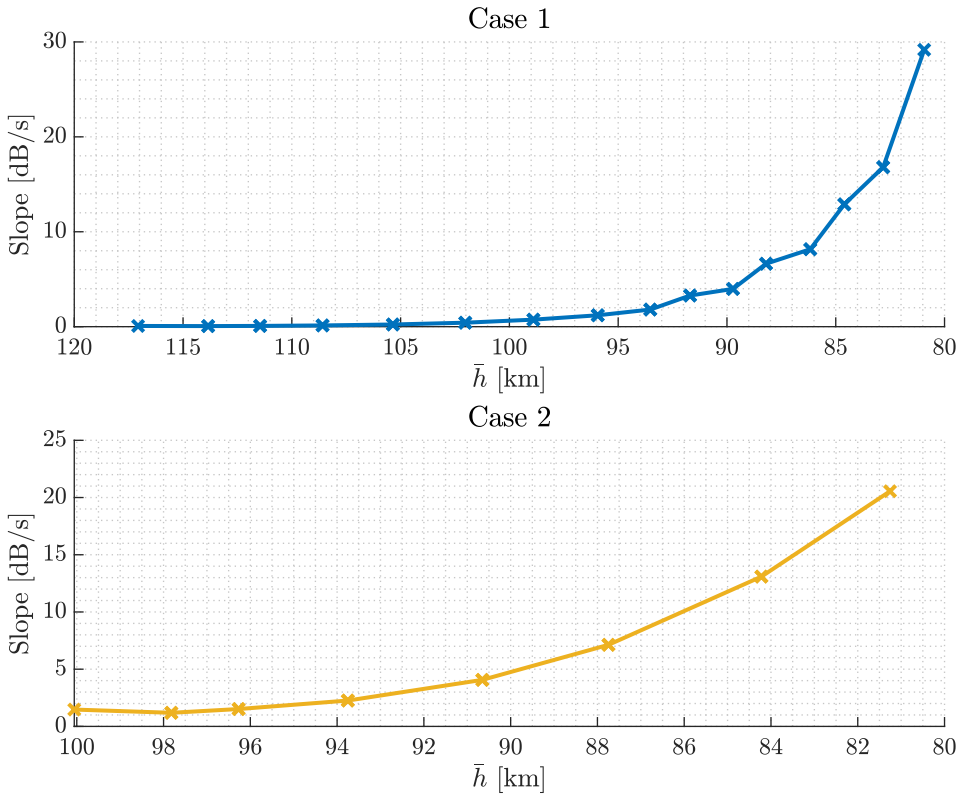

Figure 3.13: Slopes of the norm evolution with respect to the mean altitude.

GTO spacecrafts. It is the upper stage of the Indian geosynchronous satellite launch vehicle, GSLV-D5, which inserted the satellite GSAT-14 into a GTO on January 5$^{\text{th}}$, 2014 (Fletcher J and Sharma [2014]).
The implementation of the automatic domain splitting technique does not guarantee the

Table 3.7: Initial state and epoch for the Tiangong-1 and the GSLV R/B spacecrafts.

Spacecraft	TLE epoch	a [km]	e [-]	i [°]	Ω [°]	ω [°]	M [°]
Tiangong-1	01-04-2018	6543.92	0.000747	42.74	200.60	347.81	12.97
GSLV R/B	07-06-2014	7309.96	0.1151519	19.11	114.03	357.50	248.83

accuracy and the convergence of the final evaluation of the points belonging to the uncertainty cloud. This is particularly true when dealing with the re-entry problem, due to the high nonlinearities involved. The results depend on the DA order used, the maximum number of splits allowed for each domain, and the tolerance considered for the splitting

criterion. The uncertainties are applied only on the semi-major axis and the eccentricity, since they are the variables which have the greatest influence, and the only elements that affect the re-entry time. The criterion for the splitting decision is applied by considering the additional DA expansion of the perigee altitude h_p. It is a meaningful parameter to monitor because it includes both the expansions of a and e, and it allows to set a single tolerance.

The uncertainties in the initial state for the Tiangong-1 and the GSLV R/B are in Table 3.8, and they are kept constant for the whole analysis. Excessive uncertainties may terminate the propagation. The failure usually occurs during the splitting of a polynomial into two. The two polynomials are created, but, one of them or both, can be characterised by an eccentricity lower than zero, which is not physical. When the integrator propagates that condition, the right-hand-side diverges and the integration breaks. For this reason, the uncertainties are maintained limited to avoid any possible failure. Although, since the scope is to test how the domain splitting parameters influence the results and their accuracy compared with the numerical Monte Carlo, the uncertainties selected cause a spread of the initial cloud into few orbits, which is a severe condition for the mathematical DA formulation.

In order to clearly identify the influence of the three different parameters, each of them

Table 3.8: Uncertainties in the initial state, Tiangong-1 and GSLV R/B.

Spacecraft	σ_a [km]	σ_e [-]	σ_i [°]	σ_Ω [°]	σ_ω [°]	σ_M [°]
Tiangong-1	± 2	± 0.00001	-	-	-	-
GSLV R/B	± 3	± 0.0005	-	-	-	-

is analysed by maintaining constant the other two. The maximum number of evaluations is 10,000 points. The DA parameters used for the influence analysis are reported in Table 3.9.

Table 3.9: DA parameters for the domain splitting analysis.

DA order	Max. number of splits	Tolerance on h_p	Max. number of evaluations
5	8	10^{-4}	10,000

DA order

The results provided by the methodology proposed, which include the domain splitting, are influenced by the DA order used. Indeed, the DA order determines the coefficients magnitudes and the tendency of the polynomial to diverge close to the domain bounds,

where higher orders are more prone to be inaccurate. Therefore, the choice regulates the splits frequency.

The analysis here described deals with the comparison of the mean spatial error, the computational time, and the constraint satisfaction success for four DA orders, 4, 6, 8, and 10.

Figure 3.14a provides the trends of the mean spatial error for the different DA orders, corresponding to the Tiangong-1 in yellow, and the GSLV R/B in blue. As expected, higher orders are more accurate, and in both cases the minimum mean error is accomplished when using order 10. Moreover, for highly eccentric orbits, the error is several times higher compared with the low eccentricity case. The error is calculated by comparing the results obtained with numerical Monte Carlo campaign of the same cloud of initial conditions.

The constraint satisfaction does not always converge, due to the magnitude of the coefficients involved. From the numerical point of view, for a given sample, the constraint satisfaction is assumed to succeed if the resulting eccentricity is positive, the semi-major axis is greater than the radius of the Earth, and smaller than the initial a. Overall, the percentage of the constraint satisfaction success is measured by dividing the number of points for which the procedure was able to give an acceptable result, and the total number of initial samples. In Figure 3.14b, the percentage of the constraint satisfaction success with respect to the DA order used is shown, for both the Tiangong-1 (in yellow) and GSLV R/B (in blue). Higher orders are penalised, for order 10, for instance, only few points are effectively evaluated. Moreover, the convergence in the case of low eccentric orbits is better, reaching a difference of more than 50% for DA order 4.

Overall, the methodology performs better for low eccentricities, since they guarantee a

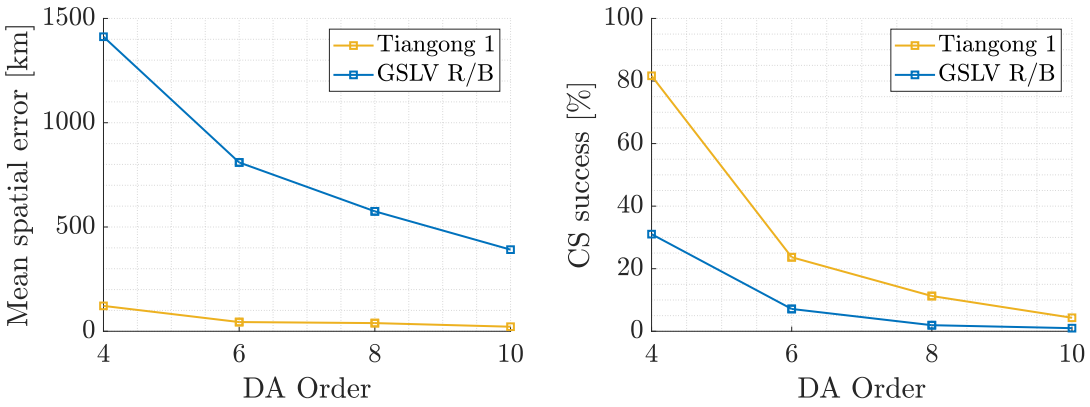

(a) Mean spatial error

(b) Constraint satisfaction success

Figure 3.14: Effect of the DA order on the mean spatial error and the CS convergence.

good convergence of the constraint satisfaction by experiencing lower mean spatial errors. Concerning the computational cost, the results are presented in Table 3.10. In order to compare the computational time of the DA propagation and the numerical Monte Carlo, it is important to stress that the numerical simulation only propagates the points for which the constraint satisfaction was able to give an output. Therefore, the computational time of the numerical Monte Carlo is not constant for each DA order used, but it varies according to the effective number of evaluations completed in the DA environment. Clearly, due to the lower convergence of the constraint satisfaction in the case of the GTO orbit, the DA propagation is never computationally efficient. While for the low eccentric orbit, with DA order 4, the DA propagation is three times faster. As the constraint satisfaction success decreases, the DA propagation becomes less efficient compared with the classical numerical Monte Carlo.

Table 3.10: Computational time in seconds according to the DA order.

DA order	Tiangong-1		GSLV R/B	
	Differential Algebra	Monte Carlo	Differential Algebra	Monte Carlo
4	196.60	644.08	1227.70	425.35
6	509.91	206.63	1596.44	75.96
8	1001.61	101.69	3114.76	26.69
10	2957.05	42.75	8426.77	10.10

The mean spatial error and the constraint satisfaction success are illustrated in Figure 3.15, by representing the impact locations over the Earth's surface, for each DA order. Since it is the most problematic case, only the GTO spacecraft is considered. The numerical Monte Carlo solution is in red, and it is only visible where the DA propagation is not able to accurately match the actual re-entry site. Coloured points are the output of the DA propagation, the ones in blue reentered earlier in time, compared with the points in yellow. As the order increases, the distribution of the impact locations is less and less accurate, until, for order 10, only few points are available.

Maximum number of splits per domain

Without imposing any limitation, the number of domains generated by the domain splitting procedure can easily reach several thousands. This results in an unreasonable computational time. To reduce the propagation cost while keeping the benefits of implementing the domain splitting procedure, a maximum number of splits is imposed. In the analysis, the maximum number varies between 0, 4, 6, 8, 10 and 13 splits. The performances are compared by looking at the mean spatial error and the constraint satisfaction success.

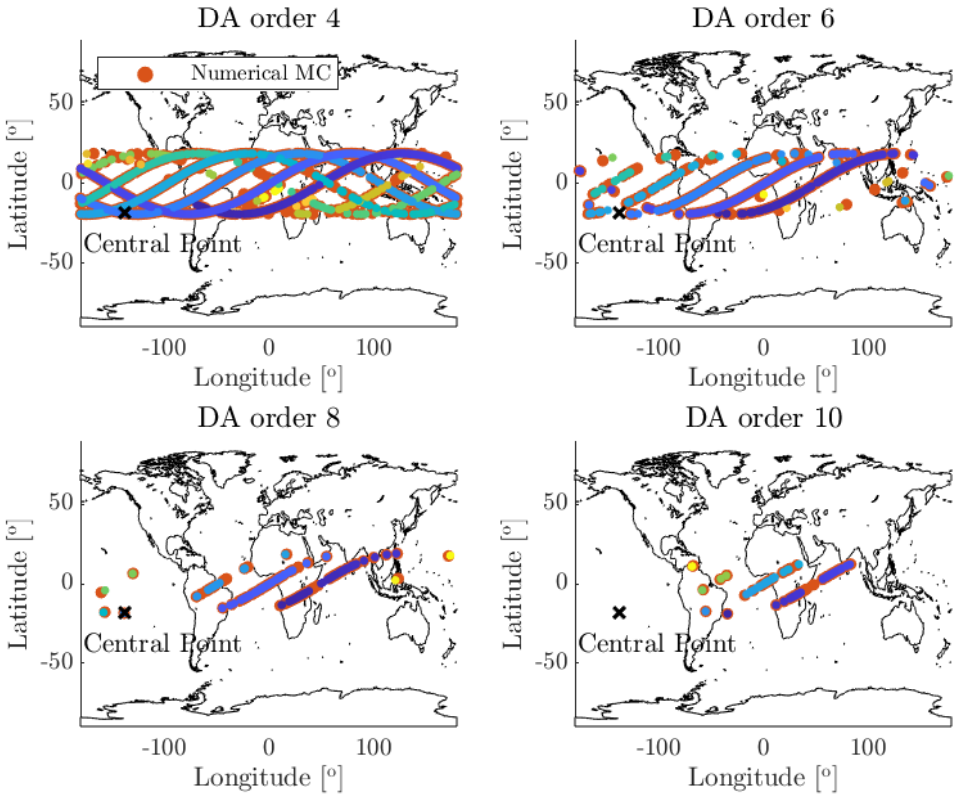

Figure 3.15: Impact locations distributions of GSLV R/B with respect to DA orders 4, 6, 8, and 10.

Figure 3.16a shows the trends representing the mean spatial error versus the maximum number of splits for the Tiangong-1, in yellow, and the GSLV R/B, in blue. The very first point of the GSSL R/B curve, is due to the fact that the constraint satisfaction only works in one point. Apart from that point, it is clear that the spatial error decreases as the maximum number of splits increases. The result is easily justified by considering that increasing the number of splits allows to reduce the effects of the nonlinearities.
The constraint satisfaction success with respect to the maximum number of splits is provided in Figure 3.16b. The Tiangong-1 performs better, reaching 100% in the last condition.
Figure 3.17 shows the impact locations of the station Tiangong-1 with respect to the maximum number of splits. When no split is allowed, only the central point and its immediate neighbourhood are approximated, while with 13 splits per domain, the whole impact distribution corresponding to the initial uncertainties selected is well represented by the methodology.

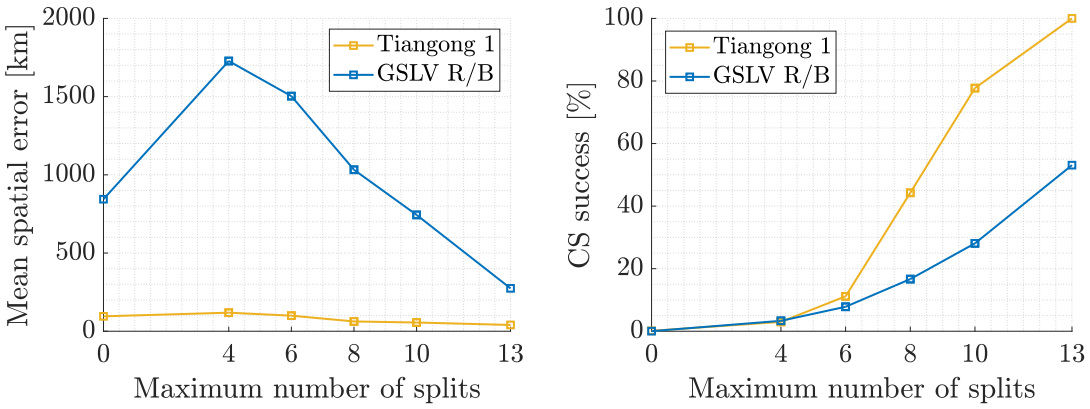

(a) Mean spatial error

(b) Constraint satisfaction success

Figure 3.16: Effect of the maximum number of splits on the mean spatial error and the CS convergence.

Accepted tolerance

During the propagation, the splitting occurs when the estimated norm of the perigee altitude exceeds an accepted tolerance. The tolerance affects the results, by influencing the rate of the splits. The tested values for the tolerance are 0.05, 0.01, 0.0001, 10^{-6} km. Figure 3.18a, shows the mean spatial error as function of the h_p expansion tolerance. The two curves refer to the Tiangong-1 (in yellow) and the GSLV R/B (in blue), respectively. For both cases, the mean spatial error reduces as the tolerance reduces as well. The actual reduction is not continuous, but after reaching a certain value it experiences a sort of plateau.

The constraint satisfaction success is almost constant as the tolerance varies, but the percentage is overall higher for the Tiangong-1, compared with the GSVL R/B.

Conclusive comments about the domain splitting parameters

Firstly, it is important to mention that the two cases are not directly comparable, since their initial satellite state and re-entry time differ significantly. In fact, while the Tiagong-1 TLEs are taken about one day prior to the impact, the propagation of the high eccentricity orbit for the same period fails to converge for the same uncertainty range, the initial epoch chosen is only few hours before the actual re-entry. Thus, despite the different conditions, it is possible to draw some conclusive comments. From the analysis above, for highly eccentric orbits the error is several times higher compared with the low eccentricity case. Also, the computational time is usually higher for the GTO objects, and the constraint

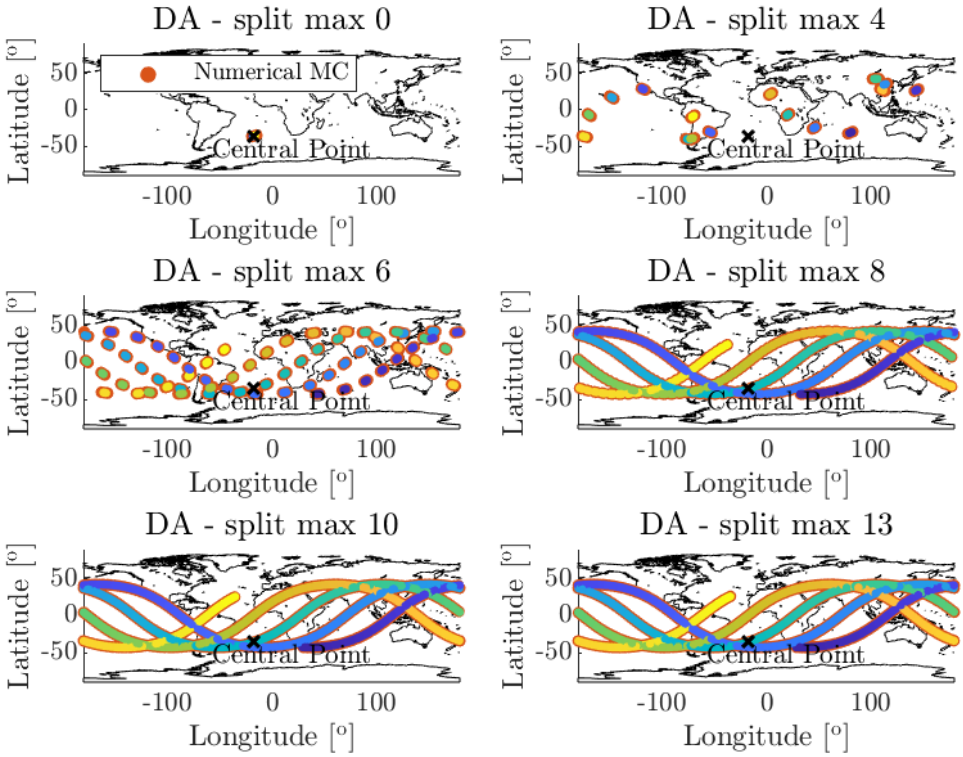

Figure 3.17: Impact locations distributions of Tiangong-1 with respect to the maximum number of splits.

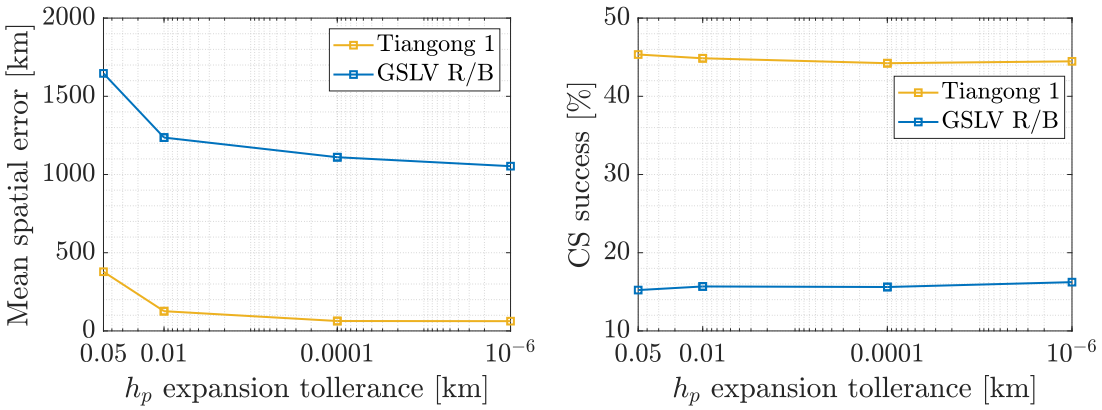

(a) Mean spatial error

(b) Constraint satisfaction success

Figure 3.18: Effect of the accepted tolerance on h_p on the mean spatial error and the CS convergence.

satisfaction works better when the eccentricity is limited. Overall, the whole methodology works better for objects characterised by a low eccentricity, as it was already proven in Section 3.4.
One possible hypothesis to interpret those results is based on the following consideration. An object in a highly eccentric orbit is subjected to large altitude and atmospheric density variations. Hence, the semi-analytical equations must take into account a wider change in the drag effect, and, in conclusion, the polynomial expansion fails in representing the increased nonlinearities.
The explanation proposed is not mathematically proven, and it is just retrieved from an observation of the numerical experiments.

3.7 Velocity uncertainty analysis

Initial state uncertainties and their magnitude determine the spread of the re-entry impact points over the Earth' surface. In the previous sections, uncertainties have been expressed in terms of Keplerian elements, and only displacements in a and e were considered. Although, an exhaustive discussion concerning the initial state uncertainties would require to consider the uncertainties in the six Keplerian elements, increasing the computational burden. Alternatively, it is possible to express the velocity uncertainties in terms of flight path angle, velocity magnitude, and azimuth. The three parameters completely define the velocity vector, in module and space orientation. This is done because uncertainties in re-entry predictions are often addressed by means of those elements, especially in space debris re-entry campaigns. Therefore, the satellite state is given in terms of flight elements, but the expansion variables are still Keplerian elements. The parameters for the uncertainty analysis are provided in Table 3.11.
The section describes the results concerning the effects of a variation in the flight path

Table 3.11: Parameters for the velocity uncertainty analysis.

DA order	Max. number of splits	Accepted tolerance	Max. number of evaluations
5	7	0.001	2000

angle, the velocity magnitude, and the azimuth angle. The cumulative effects are not included.

Flight path angle effect
A variation in the Flight Path Angle (FPA) does not affect the velocity magnitude, but it only causes a rotation of the velocity vector in the orbital plane. Figure 3.19 shows the

effect induced by a variation in the flight path angle ϕ_{fpa} on nearly circular and highly eccentric orbits. In the low eccentricity case, the spacecraft is close to the perigee, as it occurs to the Tiangong-1 at the TLE epoch reported in Table 3.12. While the object in the high eccentricity orbit is moving from the apogee to the perigee, as the GTO rocket stage GSLV R/B. The original orbit is in red, a positive variation characterises the orbit in yellow, and the orbit in blue is generated by a negative variation of the FPA. The variations of the FPA applied are 100 times the maximum variation in Table 3.12, in order to distinguish the three orbits and to better describe the effect.
Table 3.12 provides the set of tested uncertainties on the FPA. Despite the two orbits are

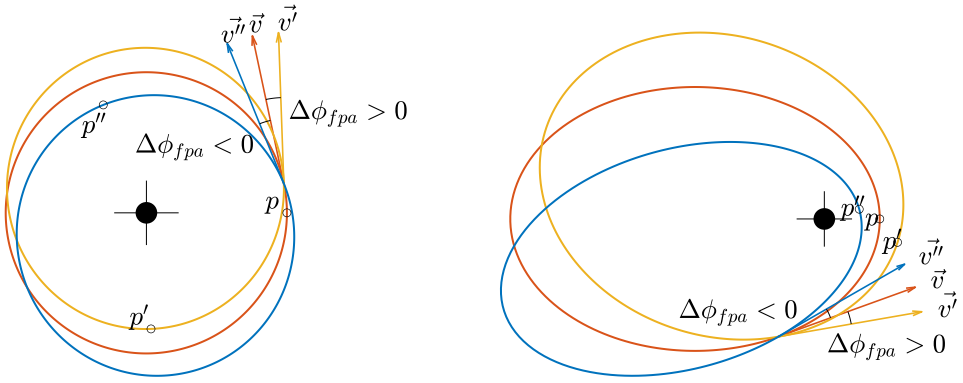

(a) Nearly circular orbit

(b) Highly eccentric orbit

Figure 3.19: Effects induced by a variation in the flight path angle ϕ_{fpa}.

extremely different, the magnitude of the uncertainties are the same, since the scope is to compare how the response of the methodology changes under different orbital conditions. A variation of the FPA affects the orbital eccentricity, the effect depends on where the

Table 3.12: Set of tested uncertainties on the flight path angle.

$\sigma_{\phi_{fpa}}$	$\pm 0.01°$	$\pm 0.02°$	$\pm 0.05°$	$\pm 0.1°$

uncertainties are applied (i.e. close to the apogee or to the perigee), since the original value of the flight path angle plays a role, and on the initial value of the eccentricity. Figure 3.20 shows the variation of the eccentricity induced by a planar rotation of the velocity vector of a quantity equal to $\Delta\phi_{fpa}$. The initial eccentricity is the red horizontal dotted line, the Monte Carlo variation is in yellow, while the differential algebra approximation is provided according to different DA orders.
Figure 3.20a describes how a variation in the FPA affects the eccentricity in the case

of a low eccentric orbit. The original eccentricity is extremely small, and the flight path angle in a circular orbit is close to 0°. Therefore, even a small FPA variation produces a change in the eccentricity, which can even double. The DA cannot approximate the extreme change in the eccentricity with good accuracy, especially for higher orders, see as reference the line in light blue. Higher order expansions are more accurate close to the central point, but they loose their accuracy as the variation is increased. Lower order, instead, are able to represent more accurately the limits of the uncertainty interval. In order to precisely represent the initial Keplerian elements displacement, only in the case under discussion, the DA order used is lowered from 5 to 3. The curve is not symmetric with respect to a zero variation because the initial flight path angle is not zero, but positive. This means that, when applying a negative variation in the FPA, at a certain point the FPA becomes zero, and then the eccentricity starts to increase in the other direction. The effect is a rotation of 180° of the perigee position. This only occurs in the case of the Tiangong-1 because its orbit is almost circular. For the GTO orbit, a FPA variation does not cause extreme variations in the eccentricity magnitude, see Figure 3.20b. The trend is linear and all the DA orders are able to approximate the numerical curve. A positive FPA variation causes the eccentricity to decrease because the orbit is shrunk, while a negative variation causes the eccentricity to increase because the orbit is expanded. This can be easily seen in Figure 3.23, because the blue orbit is more circular compared with the original, and the yellow one is more eccentric than the initial.
The re-entry window is affected by a variation in the FPA, by a quantity that depends

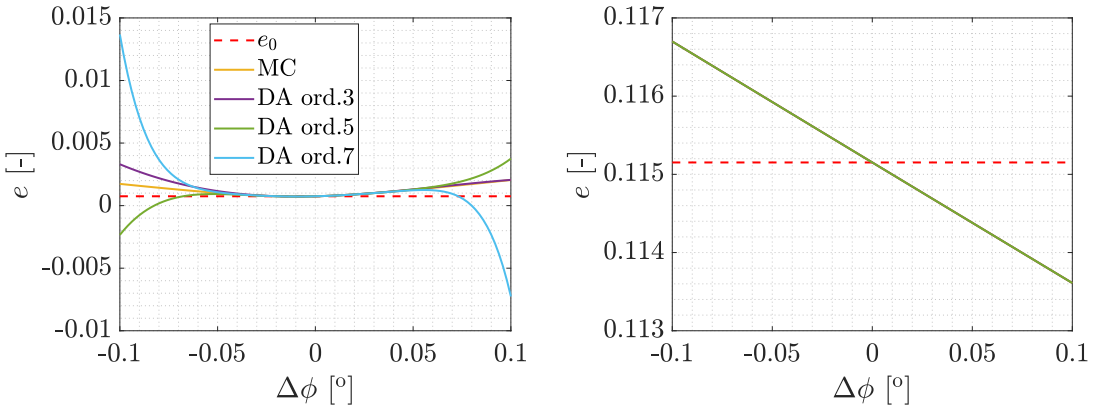

(a) Tiangong-1

(b) GSLV R/B

Figure 3.20: Eccentricity as a function of the flight path angle ϕ_{fpa}.

on the magnitude of the variation itself. A small variation does not strongly affect the re-entry time, while a large variation can even postpone the re-entry of few days.

Figure 3.21 provides the re-entry time bounds as a function of the variation in the FPA. The re-entry of the central point is in red. The numerical Monte Carlo bounds are in yellow, while the approximations found with the methodology proposed are in black.
Figure 3.21a refers to the Tiangong-1. The upper bound almost completely coincides with the nominal re-entry, while the lower bound is well approximated by the DA only in the first three tests. In the largest uncertainty domain tested the numerical solution diverges from the exact one.
For high eccentric orbits, in Figure 3.21b, the re-entry window increases from few hours, to almost two days for the maximum FPA variation. The DA approximation is close enough to the exact solution.
The re-entry time distribution as function of the eccentricity, for the maximum flight

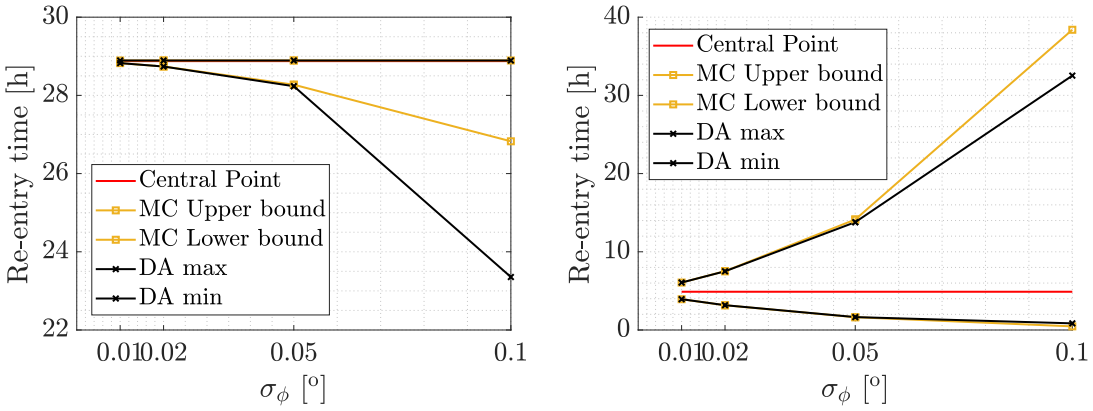

(a) Tiangong-1 (b) GSLV R/B

Figure 3.21: Re-entry time bounds as a function of the flight path angle ϕ_{fpa}.

path angle uncertainty, is shown in Figure 3.22. The numerical Monte Carlo solution is in blue, while the approximation given by the DA is in yellow. For the Tiangong-1, in Figure 3.22a, the positive variations of the FPA are well represented, while the negative variation part is not converging properly. This is justified by considering Figure 3.20a, where it is possible to see that only the positive part is well approximated by an expansion of order 3. In fact, a flight path angle variation in both direction causes an increase in the eccentricity. Therefore the two domain branches, starting from the central point, tend to overlap, but the polynomial expansion fails in representing both sides with the same accuracy. Figure 3.22b, refers to the GSLV R/B spacecraft, the two lines for the DA and the numerical MC are almost completely overlapped, meaning that the methodology proposed is able to accurately predict the re-entry window.
A variation in the flight path angle can affect the accuracy of the spatial position, com-

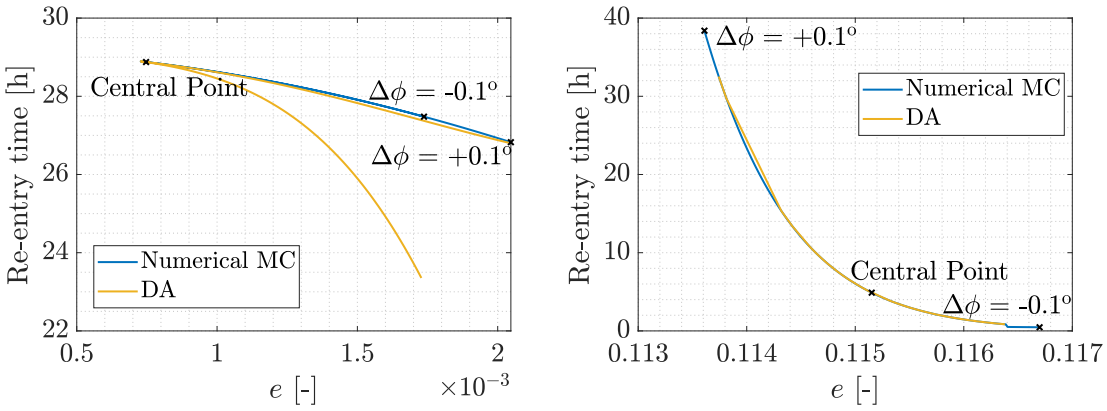

(a) Tiangong-1 (b) GSLV R/B

Figure 3.22: Re-entry time as a function of the eccentricity for the maximum flight path angle uncertainty.

pared with the numerical Monte Carlo approach. Moreover, as the applied variation increases, the DA expansion evaluation converges less, especially at the limits of the domain. Figure 3.24 shows the relation between the flight path angle variation and the mean spatial error, in blue, and the constraint satisfaction success, in yellow. The trends of the Tiangong-1 and the GSLV R/B are both represented. The spatial error increases with the flight path angle uncertainty. Nearly circular orbits are highly penalised, and the error exceeds 3,000 km in the particular case of the Tiangong-1. On the contrary, the constraint satisfaction always works for Tiangong-1, while for the GTO object the convergence reduces with the increase of the FPA variation.

Concerning the re-entry sites over the Earth' surface, Figure 3.24 shows the impact distribution when a variation of the FPA is applied. The numerical Monte Carlo solution is in red, while the DA approximation is coloured according to the side bar, which represents the difference between the exact re-entry time and the approximated one. The central point is highlighted, as well as the points characterised by the lower and upper bounds of the FPA variation. Figure 3.24a refers to the Tiangong-1, which shows a variation of $\pm$ 0.1°. The approximated time is constantly below the re-entry time of the reference point, and the red zones are visible because in those areas the DA solution is characterised by huge spatial errors. The central point is located at one end of the distribution, the effect can be again justified by looking at the relation between the FPA variation and the eccentricity (Figure 3.20a). The impact distribution of the GSLV R/B for a variation of $\pm$0.02° is shown in Figure 3.24b. For higher uncertainties, the distribution is not well-represented. In this case, the central point lies in the middle of the distribution.

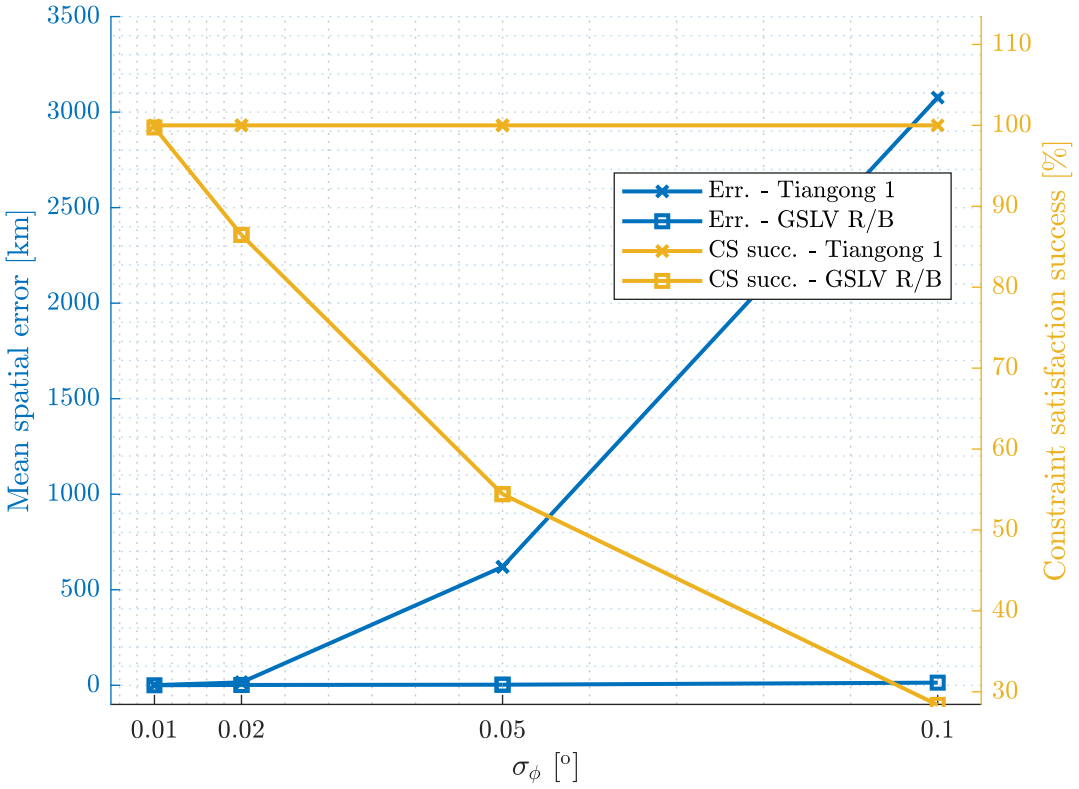

Figure 3.23: Mean spatial error and constraint satisfaction success as a function of the flight path angle ϕ_{fpa}.

Highly eccentric orbits are better approximated in the presence of huge variations in the FPA. The result is not unexpected, because nearly circular orbits are characterised by a flight path angle close to zero, and the variations applied are proportionally large, changing the orbit dramatically. More realistic uncertainties are smaller than the ones discussed in the present section, but the scope here is to test the behaviour of the model in the presence of extreme variations, to prove its reliability.

Velocity magnitude effect

A variation in the velocity magnitude changes both the orbit semi-major axis and eccentricity, affecting the re-entry time. The effect induced by a variation in the velocity magnitude v is shown in Figure 3.25 and it depends on where uncertainties are applied along the orbital path. In the Tiangong-1 case, from Figure 3.25a and Figure 3.26a, it is seen that the semi-major axis a and the eccentricity e are directly proportional to the velocity magnitude variation. The orbit of the GTO stage GSLV R/B experiences an increase of the semi-major axis and a decrease of the eccentricity when a positive Δv is

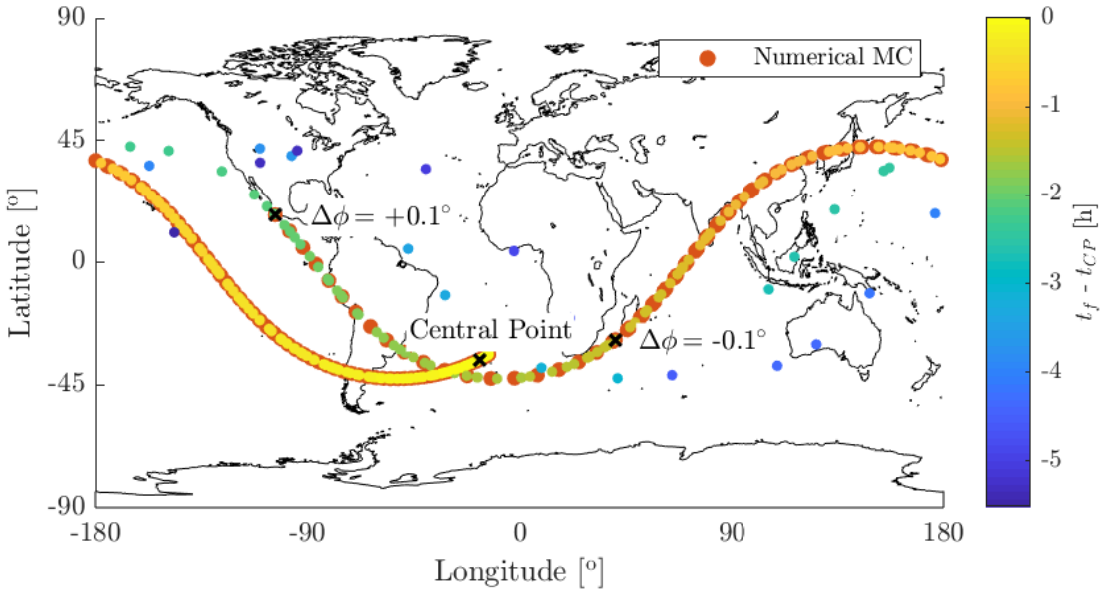

(a) Tiangong-1 - $\sigma_\phi = \pm 0.1^o$

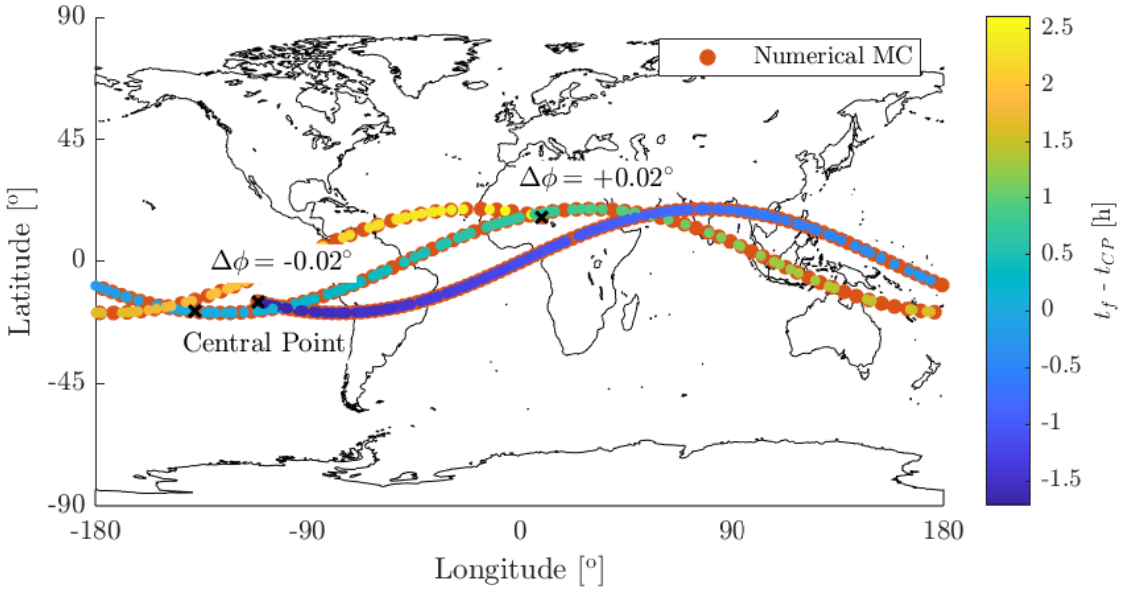

(b) GSLV R/B - $\sigma_\phi = \pm 0.02^o$

Figure 3.24: Impact locations distribution with respect to the flight path angle uncertainties.

given. As provided in Figure 3.25b and Figure 3.26b.

Table 3.13 provides the tested uncertainties on the velocity magnitude.

The methodology proposed is able to approximate with good accuracy the re-entry win-

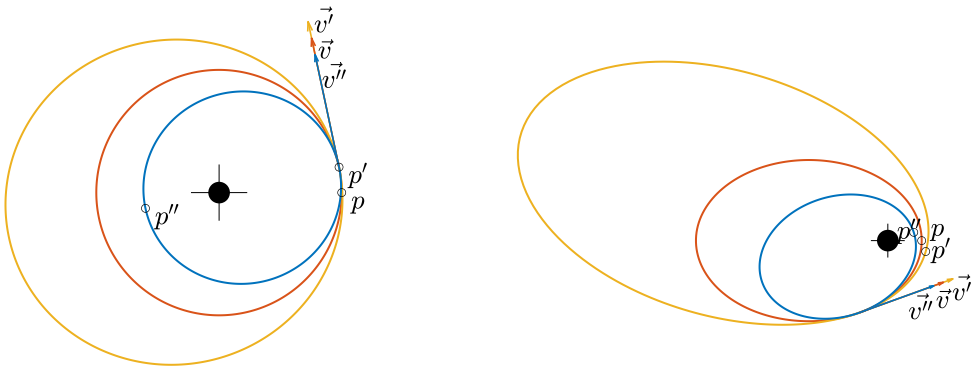

(a) Nearly circular orbit

(b) Highly eccentric orbit

Figure 3.25: Effects induced by a variation in the velocity magnitude v.

Table 3.13: Set of tested uncertainties on the velocity magnitude.

σ_v	± 0.1 [m/s]	± 0.2 [m/s]	± 0.5 [m/s]	± 1 [m/s]

dows calculated with the numerical Monte Carlo, for the Tiangong-1 (Figure 3.27a) and GSLV R/B (Figure 3.27b). In both cases, the re-entry time window becomes wider as the uncertainty in the velocity magnitude increases.

The distribution of the re-entry time when the maximum uncertainty is applied is reported in Figure 3.28. The two spacecrafts re-enter earlier in time, compared to the reference point, for a smaller semi-major axis. On the contrary, the re-entry is postponed when the orbit is characterised by an increased semi-major axis.

Figure 3.29 illustrates the effect of the velocity magnitude uncertainties on the constraint satisfaction success and the mean spatial error. The constraint satisfaction convergence is improved for smaller uncertainties in the velocity magnitude. Moreover, nearly circular orbits, as the one of the Tiangong-1, are characterised by a higher success. The mean spatial error is overall small, but the trend suggests that the higher the σ_v the higher the spatial error. The orbit of the Tiangong-1 is characterised by an higher error, compared with the GTO rocket body GSLV R/B. The difference is possibly due to the longer integration time of the Tiagong-1.

Figure 3.30 shows the impact locations on the Earth's surface for a $\sigma_v = 1$ m/s. The colour bar provides the difference between the re-entry time of each point belonging to the cloud, and the final re-entry time of the central point.

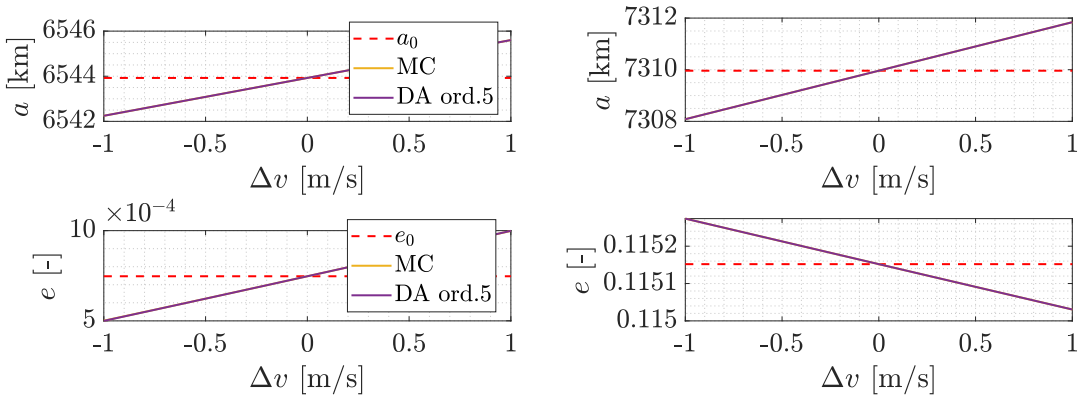

(a) Tiangong-1 (b) GSLV R/B

Figure 3.26: Semi-major axis and eccentricity as a function of the velocity magnitude v.

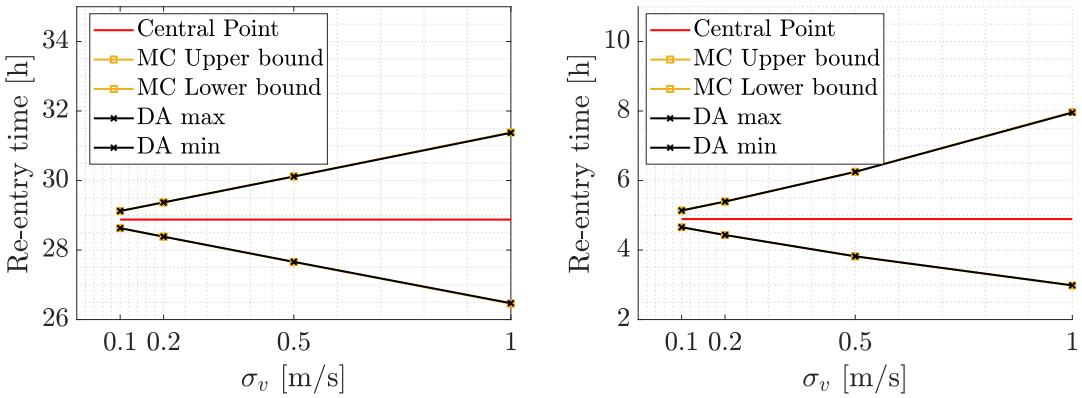

(a) Tiangong-1 (b) GSLV R/B

Figure 3.27: Re-entry time bounds as a function of the velocity magnitude v.

Azimuth angle effect

An azimuth angle variation induces a change in the orbital inclination, as shown in Figure 3.31. The semi-major axis and the eccentricity are not affected.

The tested uncertainties in the azimuth angle are provided in Table 3.14. The maximum variation of $\pm 45°$ is not physically feasible, but it is tested anyway to show that a variation in the azimuth angle does not affect the results in a remarkable way. The physical explanation lies in the fact that a and e are the only elements responsible for the re-entry time, and they are not affected by a variation in the azimuth.

The variations of the inclination and the right ascension of the ascending node as function of the azimuth angle are provided in Figure 3.32 and Figure 3.33. Different DA orders are

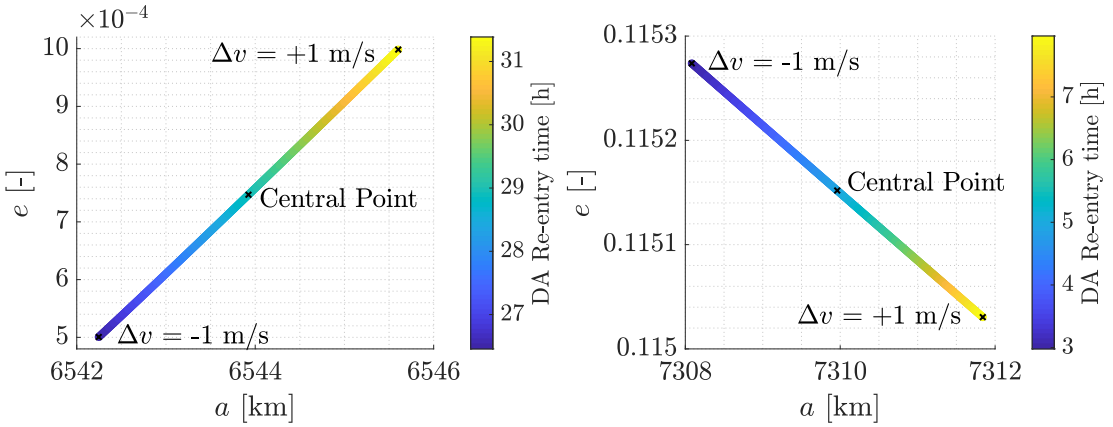

(a) Tiangong-1 (b) GSLV R/B

Figure 3.28: Differential algebra re-entry time distribution as a function of the semi-major axis and eccentricity.

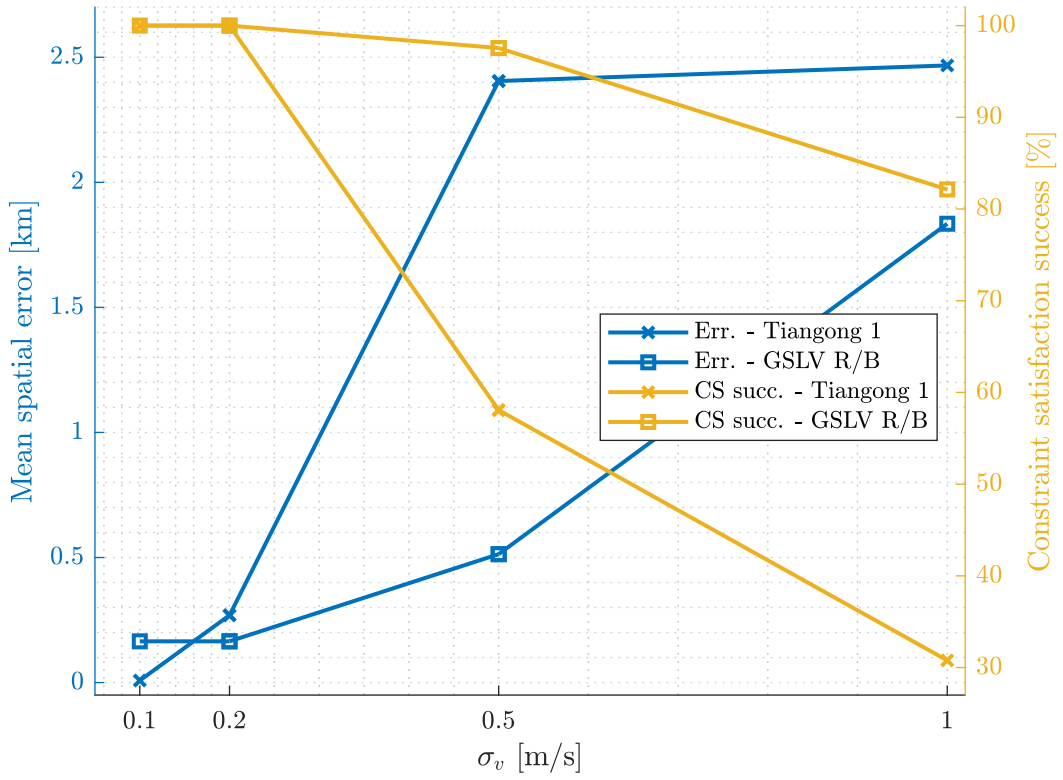

Figure 3.29: Mean spatial error and constraint satisfaction success as a function of the velocity magnitude v.

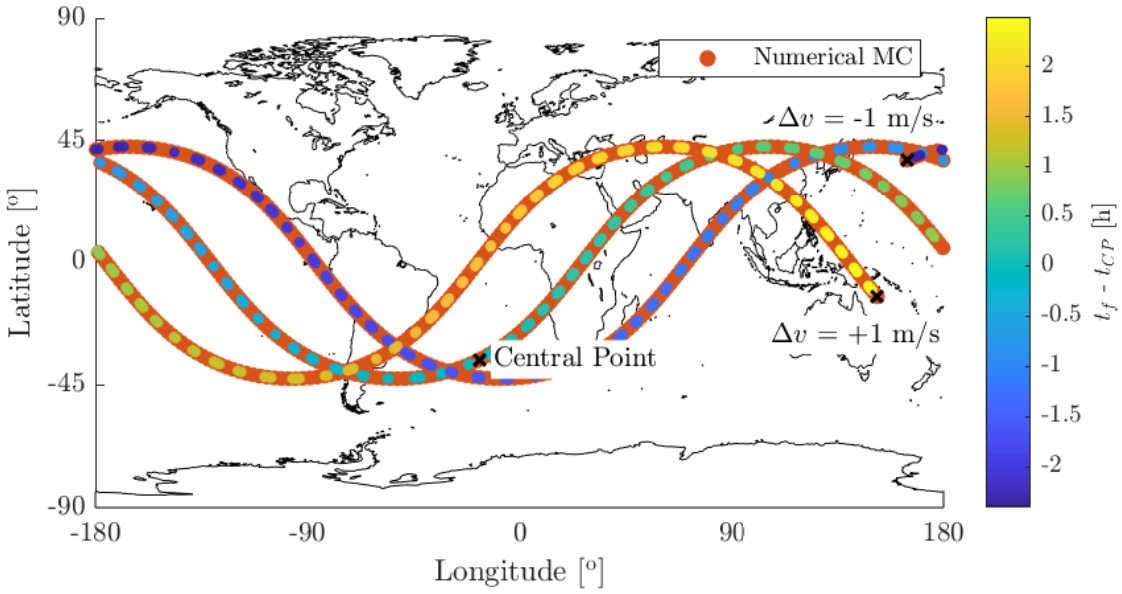

(a) Tiangong-1 - $\sigma_v = \pm 1$ m/s

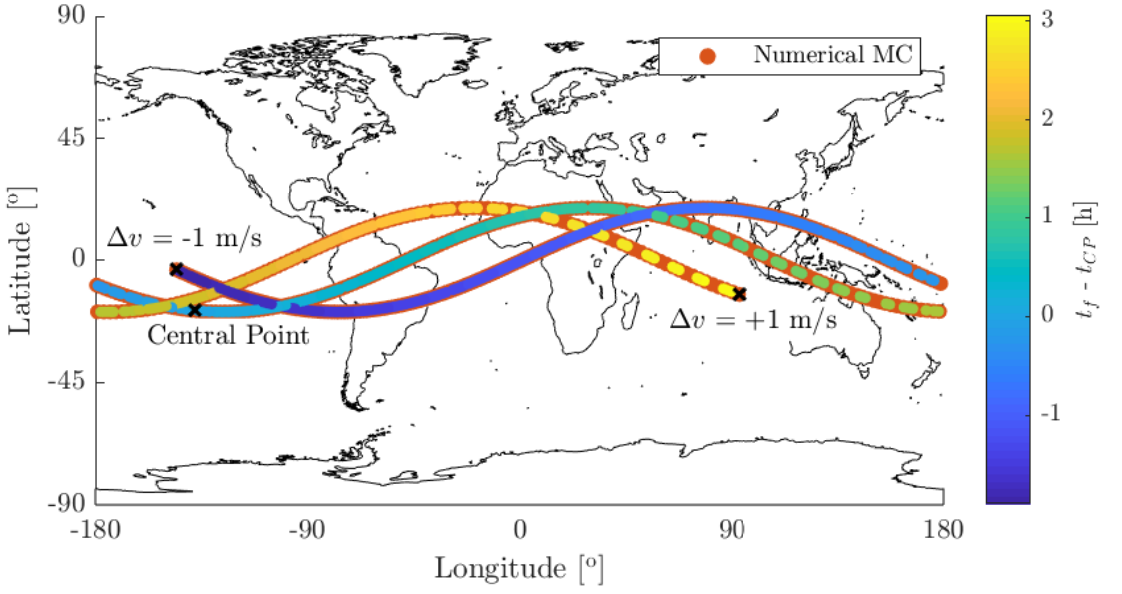

(b) GSLV R/B - $\sigma_v = \pm 1$ m/s

Figure 3.30: Impact locations with respect to the velocity magnitude uncertainties.

compared with the real trend reported in yellow. The Tiagong-1 case shows how higher DA orders tend to better approximate the Ω evolution, while for the GSLV R/B object the convergence domain is reduced increasing the polynomial precision.

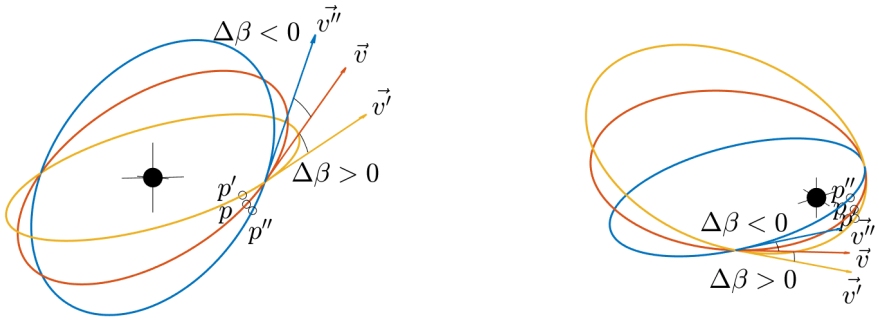

(a) Nearly circular orbit

(b) Highly eccentric orbit

Figure 3.31: Effects induced by a variation in the azimuth angle β.

Table 3.14: Set of tested uncertainties on the azimuth angle.

σ_β	$\pm 4.5°$	$\pm 9°$	$\pm 22.5°$	$\pm 45°$

Figure 3.34 provides the re-entry time bounds as function of the azimuth angle. The simulation proves the theoretical result, indeed, all the points re-enter in a time window of few seconds, even in the presence of enormous variations in the azimuth angle. Overall, nearly circular orbits (Figure 3.34a) seem to be better represented than highly elliptical ones (Figure 3.34b).
Considering Figure 3.35, the constraint satisfaction converges in 100% of the cases, no matter which uncertainty is applied. The error is contained when the uncertainties are small, but for high uncertainties the Tiangong-1 performs better than the GSLV R/B.
The impact distributions are provided in Figure 3.36. For a variation of $\pm 45°$, the Tiangong-1 impact locations are spread over almost $90°$ in latitude (Figure 3.36a). The maximum delta time is 0.6 ms. As seen in Figure 3.36b, the error is much higher in the case of GSLV R/B. In fact, the numerical Monte Carlo solution and the one provided with the differential algebra are not completely overlapped due to the misrepresentation of the initial condition given by the DA expansion.

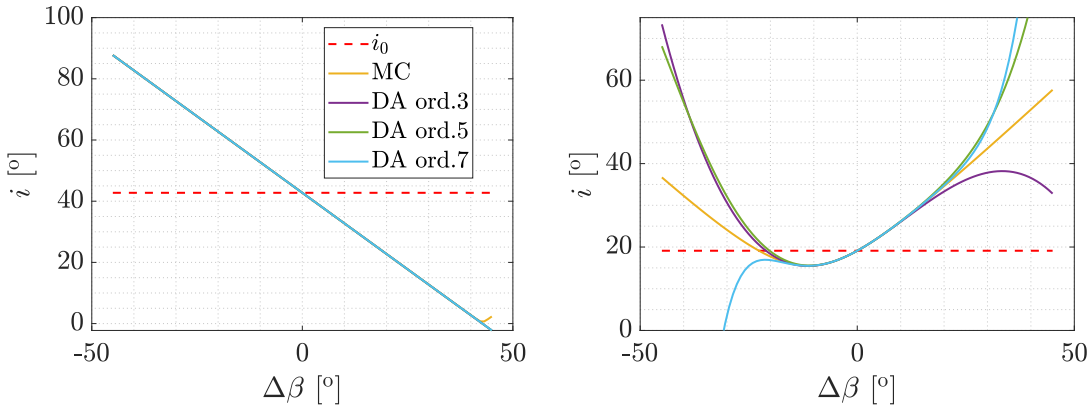

(a) Tiangong-1 (b) GSLV R/B

Figure 3.32: Inclination as a function of the azimuth angle β.

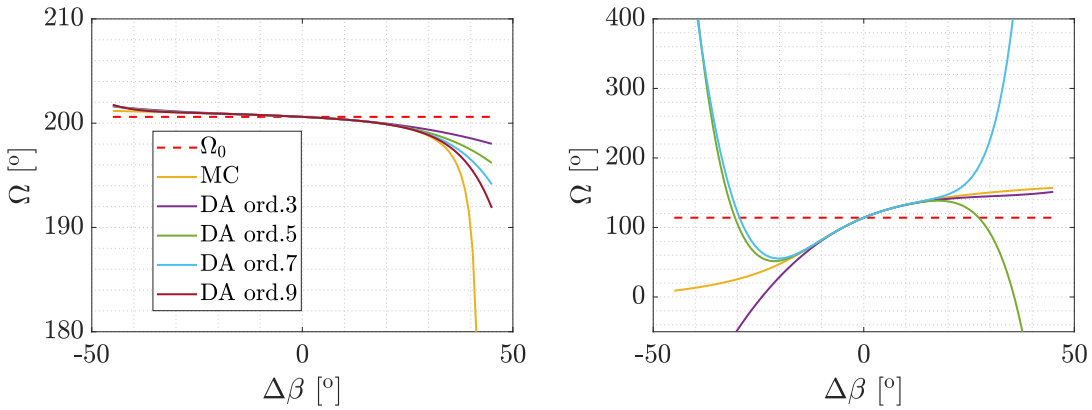

(a) Tiangong-1 (b) GSLV R/B

Figure 3.33: Right ascension of the ascending node as a function of the azimuth angle β.

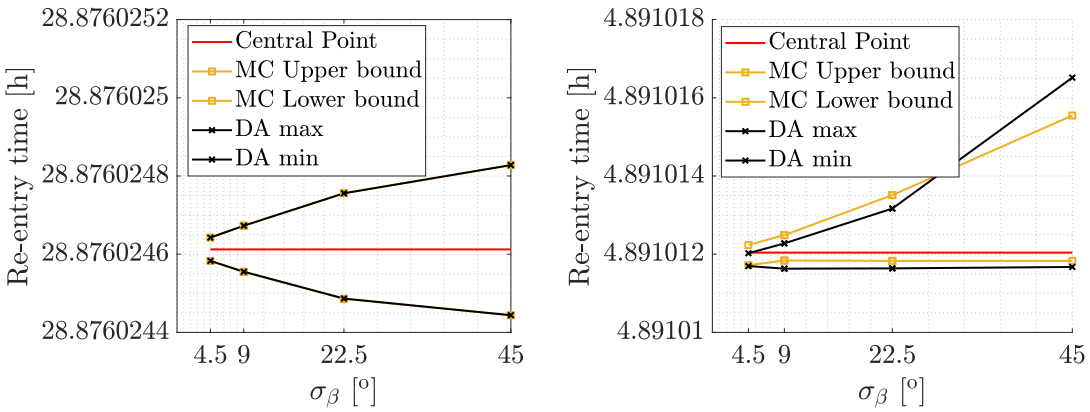

(a) Tiangong-1 (b) GSLV R/B

Figure 3.34: Re-entry time bounds as a function of the azimuth angle β.

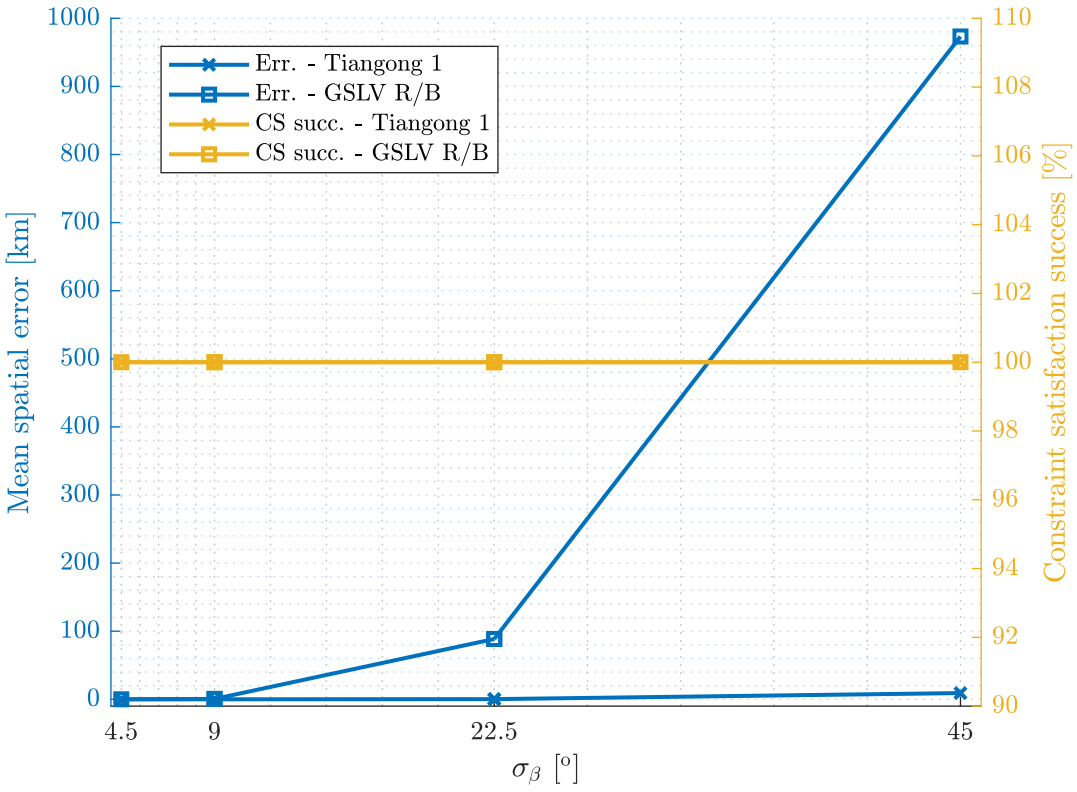

Figure 3.35: Mean spatial error and constraint satisfaction success as a function of the azimuth angle β.

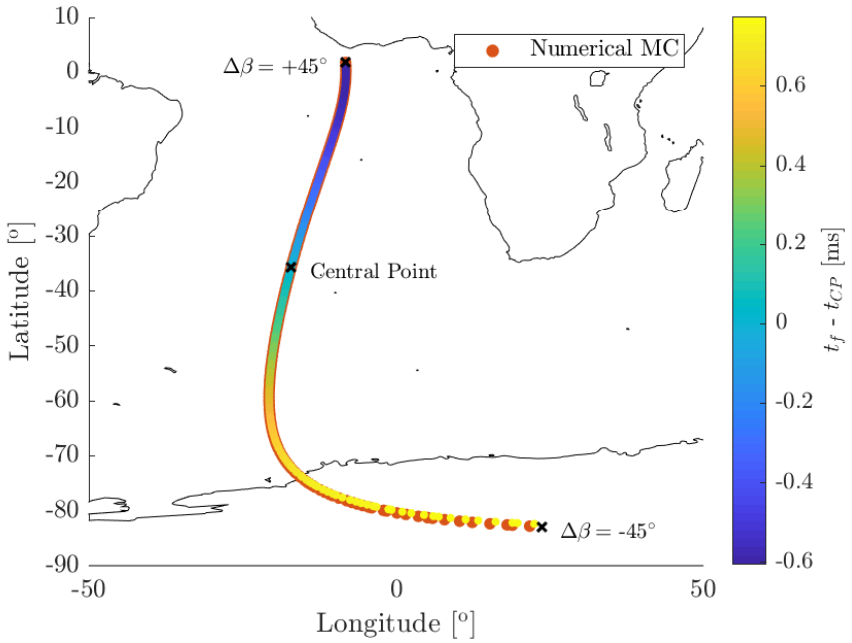

(a) Tiangong-1 - $\sigma_\beta = \pm 45°$

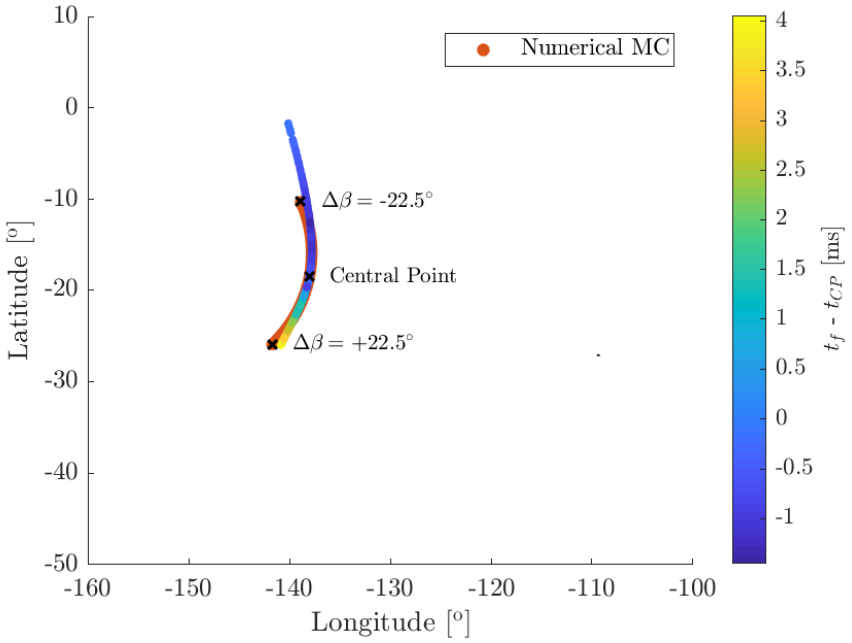

(b) GSLV R/B - $\sigma_\beta = \pm 22.5°$

Figure 3.36: Impact locations distribution with respect to the azimuth angle uncertainties.

Chapter 4

Results

This chapter consists in a description of the major findings of the thesis, to prove the reliability of the methodology proposed. The re-entry of two real objects is here analysed. Section 4.1 is a short overview concerning global sensitivity indices. Section 4.2 provides a brief presentation of the history of the selected re-entered objects studied, the GOCE satellite and the Chinese space station Tiangong-1. Section 4.3 consists in a comparison between the results obtained with the numerical Monte Carlo and the methodology discussed. In particular, the results are provided in terms of re-entry epoch predictions and ground risk map. It also deals with the analysis of the DA integration, including some important features of the methodology proposed. Finally, Section 3.5 provides the study of the global sensitivity analysis of the re-entry problem by means of the numerical Monte Carlo method and the DA-based methodology. In addition, the computational time for the two approaches is discussed.

4.1 Global sensitivity indices

This section provides a brief introduction to global sensitivity analysis, a field of probabilistic mathematics which was largely developed by I.M. Sobol' in the last decades. A summary of his research is in Sobol [2001]. Numerical models are intrinsically deterministic, since they return a set of quantities of interest $\boldsymbol{y} = f(\boldsymbol{x})$, as a function of a set of variables $\boldsymbol{x}$. Nevertheless, due to the uncertainty nature of the inputs, coming from measurements or design pending, it is more and more demanded to provide a sensitivity analysis. Sensitivity is of greatest interest in evaluating result robustness, risk analysis and on a more general approach, in understanding how the model relatively depends on the variables.

A first common deterministic approach to sensitivity is based on taking the partial derivatives $\frac{\partial f}{\partial x_i}|_{\boldsymbol{x}^*}$ with respect to a reference set $\boldsymbol{x}^*$. The resulting indices have therefore only a local validity.
A second intrusive solution for the problem is based on the computation of the derivatives directly within the model. Differential algebra can be considered as part of this category, since polynomial coefficients are the desired indices. Nevertheless, the present work has shown how the expansion can fail to represent the entire variable design space, unless a splitting technique is introduced. Thus, the use of differential algebra on its own, is not able to produce global indices, because partial derivatives are still locally defined.
Global sensitivity, developed by Sobol', has the scope to study the whole model f inside the domain, without specifying a particular input $\boldsymbol{x}^*$, taking into account the variable probabilistic nature. The next paragraph introduces the mathematical formulation of the indices and the numerical approximation, as illustrated in Saltelli et al. [2008]. Given the high number of model evaluation required, the use of differential algebra can significantly reduce the computational time of the coefficients, as it will be demonstrated later in the results.

4.1.1 Estimates of global sensitivity indices

Given a square integrable function $f(\boldsymbol{X})$ over the n-dimensional unitary hypercube I^n of probabilistic variables $\boldsymbol{X}$, it is possible to consider an ANOVA decomposition. ANOVA (Analysis of variance) is a statistical model for inference analysis on a collection of experimental samples[1]. Based on this, Sobol' defined global sensitivity indices.
The first-order index S_i, represents the degree to which the model variance depends on the considered i-variable alone, and thus it estimates how much the variance would decrease if the variable would be considered as deterministic. Moreover, the sum of all first-order indices is less or equal to one. The equality is verified only in the case in which the model has no interaction among the variables. With the same approach it is possible to compute indices for the variable coupled effects $S_{i\,j}$, but the numerical complexity increases with the interaction degree.
Total indices, $S_{T\,i}$, are usually more significant as they sum the independent effect of a variable with all its interactions. For this reason, the total index is always equal or greater than the first-order index, and the overall sum of total indices can be greater than one. S_i and $S_{T\,i}$ coincide only if the variable does not interacts with the others.
The following procedure allows for the numerical approximation of first-order and total

[1]Stanford University, *Monte Carlo theory, methods and examples. Appendix A*: `https://statweb.stanford.edu/~owen/mc/A-anova.pdf`, accessed: 13/05/2020.

sensitivities indices.
First, two matrices A and B of size (N, n) are generated, N being the number of quasi-random samples, for example using Sobol' sequence, and n the variable space dimension. Secondly, a matrix C_i is defined for each variable equal to matrix B except for the i-th column taken from A.
The model outputs are computed from each matrix of samples, their size is thus (N,1).

$$y_A = f(A) \qquad y_B = f(B) \qquad y_{C,i} = f(C_i) \tag{4.1}$$

Finally it is possible to estimate the indices thanks to Equation (4.2) and Equation (4.3).

$$S_i = \frac{(1/N)\ \sum_{j=1}^{N} y_A^{(j)}\, y_{C\,i}^{(j)} - f_0^2}{(1/N)\ \sum_{j=1}^{N} (y_A^{(j)})^2 - f_0^2} \tag{4.2}$$

$$S_{T\,i} = 1 - \frac{(1/N)\ \sum_{j=1}^{N} y_B^{(j)}\, y_{C\,i}^{(j)} - f_0^2}{(1/N)\ \sum_{j=1}^{(j)} (y_A^{(j)})^2 - f_0^2} \tag{4.3}$$

where

$$f_0^2 = \left(\frac{1}{N} \sum_{j=1}^{N} y_A^j \right)^2 \tag{4.4}$$

The two equations consist of approximations, and are based on the fact that the scalar product between two results will randomly associate high and low values of y if the i-variable is non-influential, while the correlation will be increased if the results strongly depends on X_i, increasing the value of the index. The overall computation cost for a single class of sensitivity indices is therefore $N(n + 2)$. Bootstrap re-sampling could be implemented in addition to compute the error estimates on the indices.
The present thesis deals with the satellite re-entry. In this field, the decay time is one of the key information, and thus it has been chosen in the results as the model output. In the differential algebra framework, once the integration is concluded, Sobol' samples are spread in each subdomain, and a search algorithm is required in order to evaluate the correct expansion. Moreover, the constraint satisfaction technique can fail sometimes in providing the correct re-entry solution, hence, when computing sensibilities indices, y values must be saved only in the case in which the routine works for the A, B and C_i samples. The Sobol' indices are also calculated by means of Monte Carlo methods, to compare the two solutions.

4.2 Selected reentered objects

The scope of the thesis is to provide an efficient methodology to study the re-entry of satellites in the Earth's atmosphere. Real re-entered objects are involved to present the

findings of this work. In the last years, few uncontrolled spacecrafts re-entered the Earth atmosphere, causing moderate concerns regarding the risk for the population. Among those, the GOCE re-entry in 2013 and the Tiangong-1 decay in 2018 are here discussed.

4.2.1 GOCE

The Gravity field and steady-state Ocean Circulation Explorer (GOCE) is an ESA geodynamics and geodetic mission. Its main objective was to map the Earth's gravity field, creating an accurate model of the geoid. It was launched on 17$^{\text{th}}$ March 2009 and injected on an orbit of 283.5 km altitude. Its operational phase lasted for 4.5 years, and the mission came to a natural end when the spacecraft run out of fuel on 21$^{\text{th}}$ October 2013, triggering a fast orbit decay eventually leading to its disintegration in the atmosphere three weeks later, on November 11. The spacecraft re-entered the Earth's atmosphere over the South Atlantic Ocean, close to the Falkland islands[2].
GOCE's re-entry took significantly longer than initially predicted, due to its aerodynamic shape and controlled attitude, and much lower atmospheric densities than predicted. The re-entry was previously studied by the ESA/ESOC Space Debris Office (SDO) and Japan Aerospace Exploration Agency (JAXA). Furthermore, the re-entry of GOCE is particularly interesting, because of the availability of many different measurements, such as TLEs, additional tracking by the Joint Space Operations Center (JSpOC), dedicated radar tracking, GPS solutions, and accurate solutions for the attitude. All these data allow for benchmarking the models and approaches (Geul et al. [2018]).
Considered its aerodynamics shape, the study of the GOCE re-entry could be potentially extended for the study of long cylindrical objects with fixed centre of mass versus centre of gravity pose, e.g. rocket bodies. This specific configuration can, under certain conditions, lead to attitude stabilisation and, if anticipated correctly, give rise to increased accuracy in the re-entry predictions (Cicalò et al. [2017]).
The orbital configuration of the satellite on 9$^{\text{th}}$ November 2013, is retrieved from TLE data, and available in Table 4.1, the state is expressed in Keplerian elements.
Table 4.2 provides the standard deviation of errors at TLE epoch derived state for both classical and enhanced TLEs. They are made available by Geul et al. [2018], and the derivation is based on weighted differencing method (Geul et al. [2017]). The residuals refers to 9$^{\text{th}}$ November 2013. The uncertainty set used within the present thesis is the one of the enhanced TLEs.
Given the initial condition summarised in Table 4.1, the spacecraft is expected to re-enter

[2]Sharing Earth Observation Resources, *GOCE*: `https://directory.eoportal.org/web/eoportal/satellite-missions/g/goce`, accessed: 30/04/2020.

Table 4.1: Initial condition of the GOCE satellite on November, 9$^{\text{th}}$ 2013.

a [km]	e [-]	i [°]	Ω [°]	ω [°]	M [°]
6545.6389	0.0006656	96.5433	342.5402	243.5102	116.5957

Table 4.2: Initial standard deviation of errors at TLE epoch. Source: Geul et al. [2018].

Type	$\sigma_{r,R}$ [km]	$\sigma_{r,S}$ [km]	$\sigma_{r,W}$ [km]	$\sigma_{v,R}$ [m s^{-1}]	$\sigma_{v,S}$ [m s^{-1}]	$\sigma_{v,W}$ [m s^{-1}]
enhanced TLE	0.089	2.4	0.033	2.9	0.11	0.018
classic TLE	0.46	6.2	0.14	7.6	0.46	0.13

after 31.77 hours. This value consists of an overestimation of the actual re-entry time of around 4 hours. The mismatch is induced by several factors. Firstly, the TLEs used may be affected by an unspecified error, which is not given by public sources and is not estimated in the present work. Moreover, semi-analytical methods are an approximation of the real motion of the satellite, therefore, an additional source of error may arise from the mathematical model itself. Finally, the spacecraft shape and attitude are not considered. Concluding, there are several influencing aspects which are not taken into account. Nevertheless, the results shown are not meant to be a correct estimation of the re-entry time, but they have the scope to prove that the DA-based methodology developed can be effectively applied to the re-entry problem.

4.2.2 Tiangong 1

This Section is completely based on the information retrieved from the work done by Pardini and Anselmo [2019], who monitored the orbital decay of the Chinese space station Tiangong-1 until the re-entry into the Earth's atmosphere.
Tiangong-1 was one of the most massive objects to re-enter without control in the second half of the 2010s. Therefore, it could have represented a potential threat to people and properties, justifying the intensive re-entry campaign promoted by the Inter-Agency Space Debris Coordination Committee (IADC). Unfortunately, no detail about the spacecraft's design, structure and materials was released by China, preventing a reliable prediction concerning the components that could have potentially survived the re-entry conditions. Tiangong-1, whose name translates as "Heavenly Palace 1", was a single-module space station operated by the China National Space Administration, and blasted off on 29$^{\text{th}}$

September 2011. It was placed in a nearly circular orbit with an altitude of about 350 km and inclination just less than 43°. It was used to test docking and rendezvous techniques, and to host two crewed missions. Tiangong-1 was originally planned to be deorbited in 2013, after two years of operations and the completion of a series of technological tests, being replaced by Tiangong-2, a similar but improved laboratory. The controlled re-entry was foreseen in the South Pacific Ocean Uninhabited Area (SPOUA). However, China repeatedly extended the length of the Tiangong-1 mission until 16$^{\text{th}}$ March 2016, when ground controllers lost the contact with the vehicle, likely due to an on-board fatal power failure. In May 2017, China informed the United Nations Office for Outer Space Affairs (UNOOSA) that the operational orbit of the vehicle was under constant and close surveillance. The average altitude of the space station was around 349 km, and it was decaying at a rate of approximately 160 m/day. Under these conditions, the re-entry of Tiangong-1 was expected sometime between October 2017 and April 2018.
From the beginning of February, i.e., when the mean altitude with respect to the equatorial radius of the Earth descended below 270 km, the nominal re-entry time began to converge towards the first week of April 2018. Tiangong-1 finally re-entered the Earth's atmosphere on April, 2$^{\text{nd}}$ 2018, over the southern Pacific Ocean.
The TLE data set used as initial state for the study of the Tiangong-1 re-entry is in Table 3.7 (Chapter 3). The standard deviations for the error estimation are in Table 4.3. They refer to the Tiangong-1 TLE epoch 03/07/2014, and obtained by Morselli [2014], from mixed radar and optical observations. They do not refer to the initial epoch for the re-entry prediction, nevertheless, since there are no publicly available sources for the TLE estimation error, the standard deviations in Table 4.3 are used as feasible errors for the TLE epoch 1/04/2018.

Table 4.3: Estimated standard deviation for mixed radar and optical observations, in Cartesian elements, for the Tiangong-1.

$\sigma_{r,X}$ [km]	$\sigma_{r,Y}$ [km]	$\sigma_{r,Z}$ [km]	$\sigma_{v,X}$ [m s^{-1}]	$\sigma_{v,Y}$ [m s^{-1}]	$\sigma_{v,Z}$ [m s^{-1}]
0.180	0.226	0.289	0.319	0.201	0.319

4.3 Comparison between the DA-based formulation and the numerical Monte Carlo

To prove the reliability of the methodology proposed, a comparative study is made, using traditional Monte Carlo method as the exact solution to be replicated as closely as possible. While the DA-based methodology is built using the DACE 2.0 library in C++, the numerical Monte Carlo simulations are performed in the `MAtlab` software environment.
The strategy adopted consisted of the following steps. The initial conditions and standard deviations proposed above, are used to generate a cloud of normal distributed random points, both for the GOCE and Tiagong-1 spacecrafts. In the first case, uncertainties are defined in the RSW reference frame (where R is the radial direction, S the along-track, and W the cross-track), while Cartesian coordinates are used in the latter, before transforming the expansion in Keplerian elements. In the numerical Monte Carlo environment, the new starting points are integrated separately. Differently, in the DA-based approach, the original condition is propagated and the domain splitting technique is applied. The criterion for the splitting decision is applied to the additional DA expansion of the perigee altitude h_p. The settings for both analysis are reported in Table 4.4. The method requires the initialisation of the domains size which is chosen equal to 4 times the standard deviation, in order to include more than the 99.9936% of the generated points. As a last step, each uncertainty requested is located in the corresponding subdomain and evaluated. Thus, a first remark is that the constraint satisfaction technique does not guarantees the complete success in evaluating all the cloud points due to the expansion divergence. In fact, of the initial 100,000 points, only about the 56% of them is correctly evaluated. Moreover, thanks to the normal distribution, the majority of points will fall in the subdomains close to the center point, and thus more likely to be correctly represented. Concerning the numerical Monte Carlo analysis, due to the computational cost, 20,000 samples where considered sufficient to obtain a reliable representation of the re-entry distribution.
The results presented consist of an illustration of the DA-based integration in Section

Table 4.4: DA-based methodology, parameters for the comparative analysis.

DA order	Max. number of splits	Accepted tolerance	Number of samples
6	10	1e-5	100,000

4.3.1, followed by the re-entry time window analysis and the spread of the impact locations on the Earth's surface, Sections 4.3.2 and 4.3.3. The re-entry epoch predictions are

shown by means of Probability Density Functions (PDFs). Comparing the two different approaches, a correlation close to 100% is desirable. The impact locations are shown by means of ground risk maps, showing the re-entry probability and the spread in latitude and longitude. Finally, Section 4.4 concerns the global sensitivity indices calculation, and the resulting computational time savings. For this final analysis the numerical experiment differs from the previous strategy and it will be described later.

4.3.1 Analysis of the DA integration

The methodology proposed exploits the domain splitting routine in conjunction with the constraint satisfaction procedure to assess the re-entry of space objects. Each domain can split a maximum of 10 times, in order to avoid unnecessary computational effort and to prevent the creation of excessive small-sized domains. To give an insight about the application of the domain splitting technique to the GOCE re-entry, refer to Figure 4.1. The figure shows the domains with respect to the velocity components R and S, where R is the radial direction and S the along-track direction. The constraint satisfaction success for each domain is given by the coloured side bar. In particular, the success criteria is defined as in Section 3.6 (Chapter 3). The percentage refers to the acceptable output values given by the CS, divided by the number of samples belonging to each subdomain. The pattern is not homogeneous, showing that some domains are better conditioned compared to others, where the coefficients explode and do not guarantee the convergence of the constraint satisfaction algorithm. It is possible to remark that the positive V_S semi-plane tends to have higher success values. This effect is due to the initial GOCE position which is located far from the perigee. Thus, a positive ΔV_S will cause the orbit circularisation, which is beneficial from a mathematical viewpoint as demonstrated in the previous analysis. Finally, the rounded shape is due to the normal distribution, while the 100% values on the boundaries are often the case of a single point being present, and its success.

The average number of splits performed in each direction is provided in Table 4.5. It is computed over all final sets at the end of the integration. It is interesting to notice that overall no split is performed along the cross-track direction (over R_W and V_W), meaning that the in-plane components are the ones that affect the most the DA expansion. From the tables, it is seen that the other four DA variables have almost the same influence. The most influencing variable is the velocity in the along-track direction V_S, followed by the radial component of the position R_R. The radial velocity V_R and the along-track position R_S almost have the same influence. In conclusion, the average number of split is a consequence of both the physical effect of the variable, and of its initial domain size.

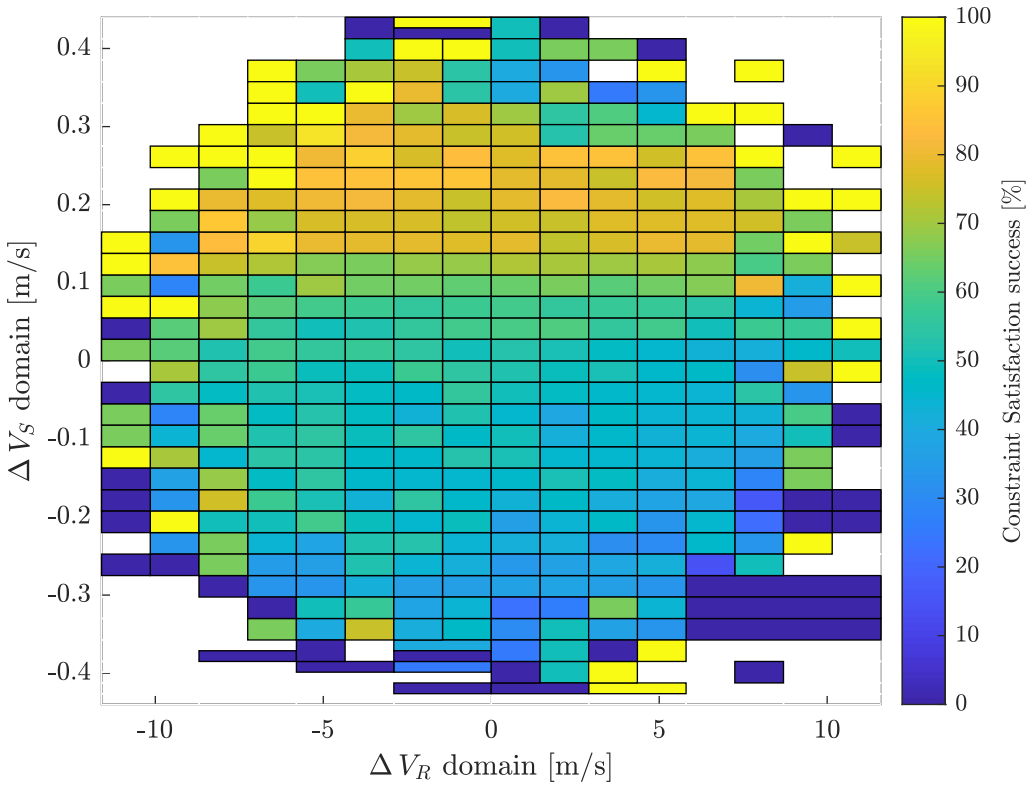

Figure 4.1: GOCE re-entry, domains with respect to the velocity components R,S.

Table 4.5: The average number of splits performed in each direction computed over all final sets at the end of the integration.

Direction	R_R	R_S	R_W	V_R	V_S	V_W
# splits	2.64	2.17	0	2.18	2.99	0

4.3.2 Re-entry epoch prediction

Figure 4.2 shows the probability density functions of the re-entry time spread obtained for the GOCE satellite and the Tiangong-1 space station. The Monte Carlo results are outlined in blue, while the estimation made by DA is in red. The boundaries given by the intervals $\pm\sigma$ and $\pm 3\sigma$ are also indicated, together with the the median of the MC (in

blue) and the DA (in red). Consider Figure 4.2a, given the initial state and the uncertainties outlined above, the GOCE is expected to re-enter in a time window of about 200 minutes. The distribution is not completely symmetric, since the re-entry is most likely to occur before the reference state, rather than after.
For the Tiangong-1, the re-entry window is around 5 hours, as provided in Figure 4.2b. The pdf is almost perfectly symmetric.
The correlation between the two probability density functions is 99.12% and 98.76%, respectively, proving that, by means of the method under investigation, it is possible to reach an extremely good accuracy as compared with a standard Monte Carlo campaign.

4.3.3 Ground risk map

The GOCE central reference point re-enters at 83° S, 25° W. Despite the re-entry time window covers about 3 hours, the impact distribution is spread over a region that covers all the latitudes, due to the high inclination of the GOCE satellite (96.54°). For this reason, the GOCE satellite can potentially re-enters over all the populated territories of the Earth. Figure 4.3 provides the ground casualty risk maps created by the numerical Monte Carlo the DA-based approaches, in the presence of uncertainties in the satellite initial state. The side bar provides the re-entry relative probability, expressed as the number of samples in that particular time band divided by the total number. On the left side of Figure 4.3b it is also shown the population density by latitude. All the latitudes are highlighted in red because, as already pointed out, the spacecraft can potentially re-enter over all the populated latitudes.
Regarding the Tiangong-1, the central point re-enters in about 29 hours, in the point located at 36° S, 17° W. The spread covers about 3 orbital ground tracks. Also in this case the numerical Monte Carlo result (Figure 4.4a), and the DA-based methodology output (Figure 4.4b) provide almost the same result. The population under treat lives between 43° S and 43° N, which is the orbital inclination.
The estimation is overall quite accurate, and also the re-entry probability associated with each impact location is almost the same with the two approaches. All the impact locations lie on the same continuous track, which is more rarefied on the outer limits, where less points are present, isolated from the rest. Overall, it can be concluded that the DA-based methodology is enough precise to be a valid alternative to the numerical Monte Carlo for the re-entry prediction simulations campaigns.

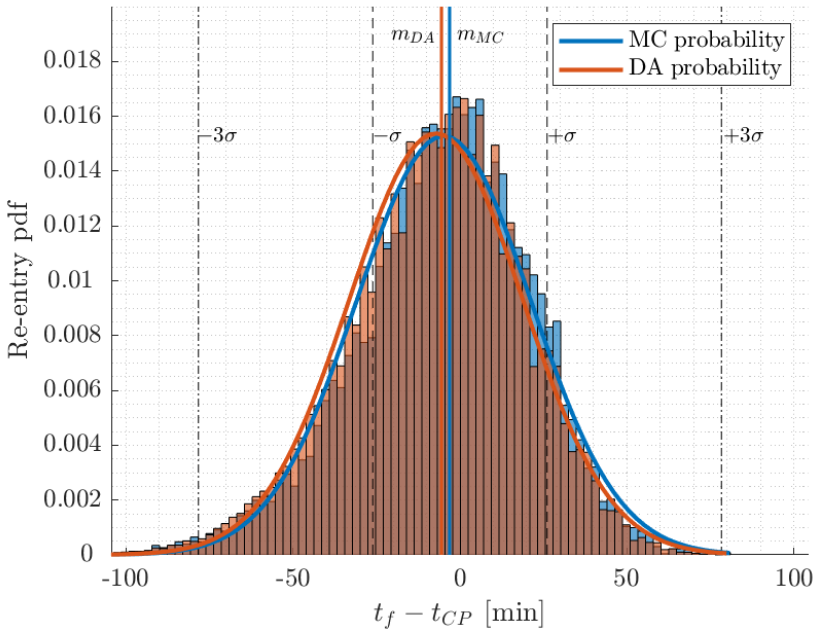

(a) GOCE

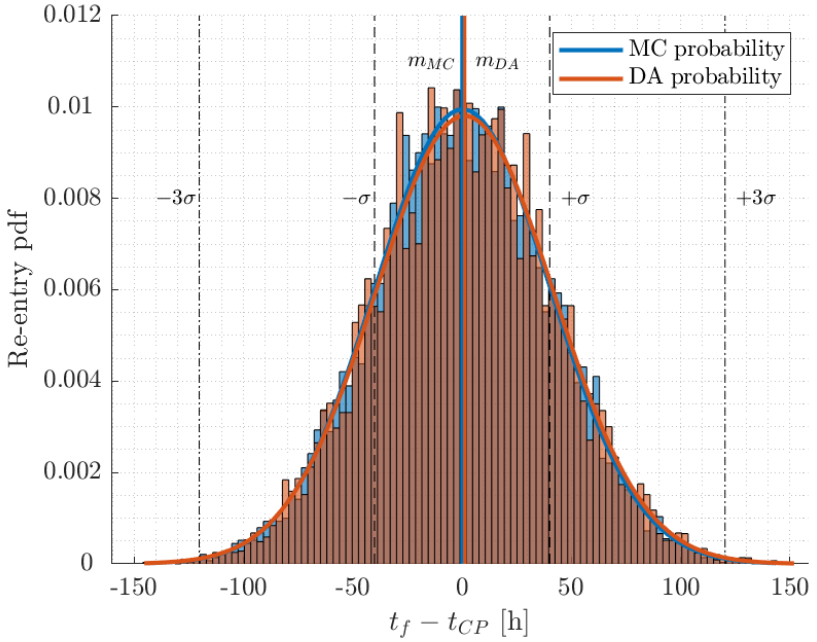

(b) Tiangong-1

Figure 4.2: Probability density functions obtained with the two approaches.

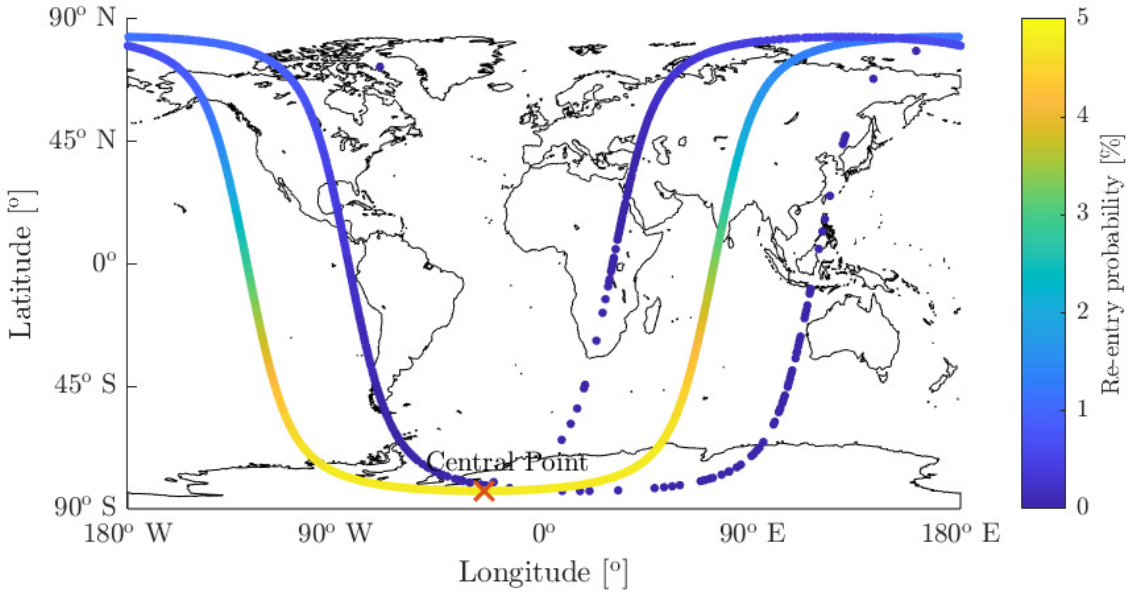

(a) Numerical Monte Carlo

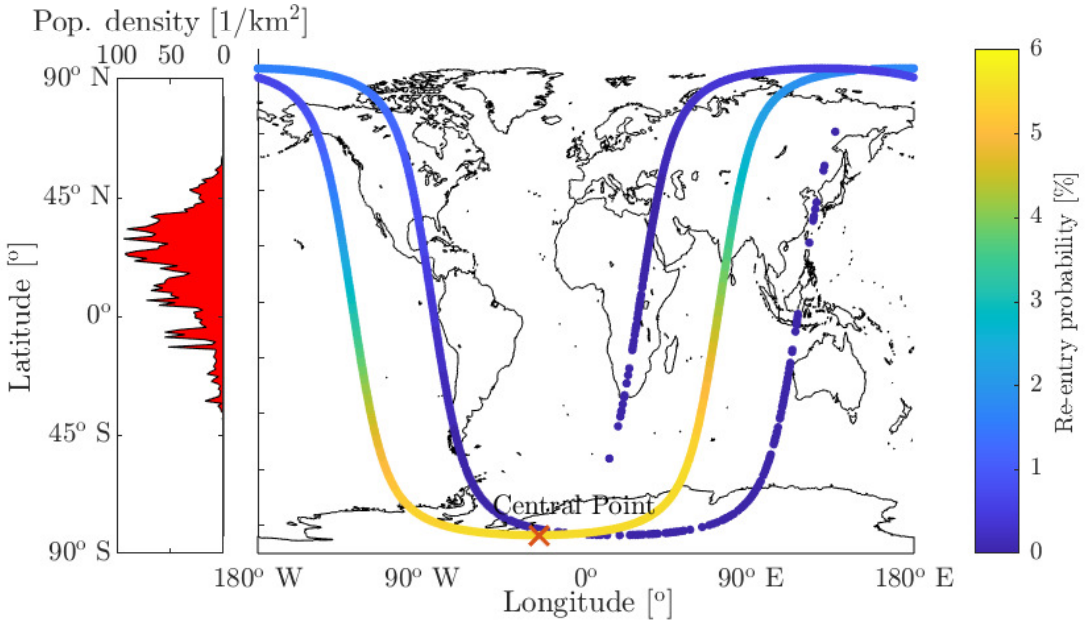

(b) DA-based methodology

Figure 4.3: Ground casualty risk of the GOCE re-entry, according to the two approaches.

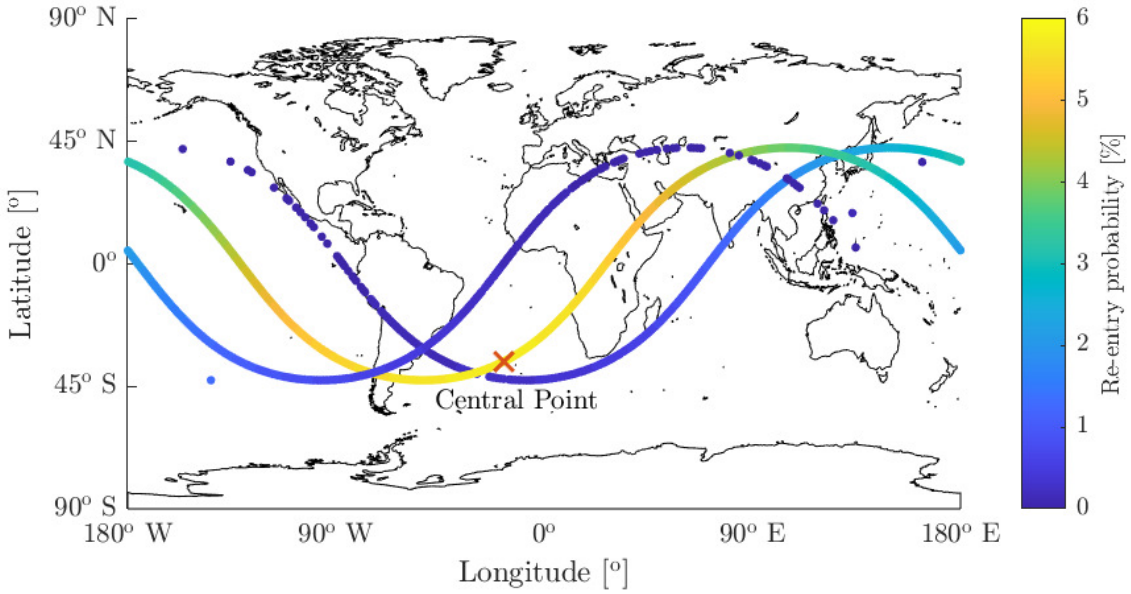

(a) Numerical Monte Carlo

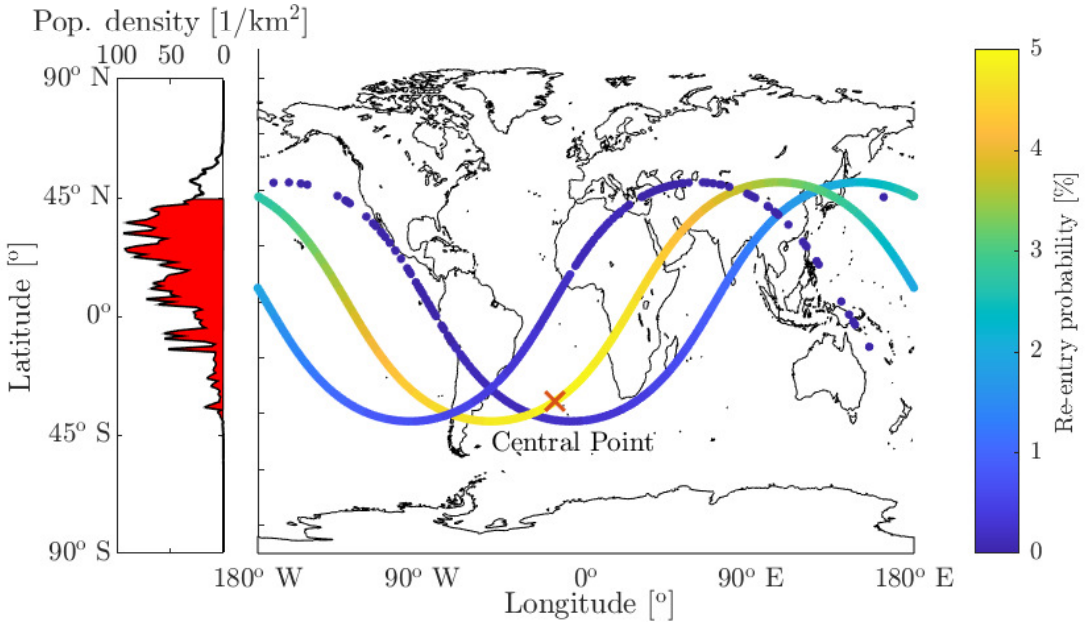

(b) DA-based methodology

Figure 4.4: Ground casualty risk of the Tiangong-1 re-entry, according to the two approaches.

4.4 Sensitivity analysis

The last step of the comparative analysis has consisted in the computation of Sobol' global sensitivity indices, using the procedure described in Section 4.1. The chosen quantity of interest is the relative re-entry time, $t_{final} - t_{CP}$, from the original initial conditions. The uncertainty set of variables chosen for the GOCE and Tiagong-1 objects is again different in the two cases.

The parameters used for the DA-based routine are provided in Table 4.6. In particular, the sample size N given must be divided by a factor 100 for the numerical Monte Carlo approach. The greater number of samples used in the DA environment is justified by the failures in the constraint satisfaction routine, and by the irrelevant cost of each polynomial evaluation. The parameter N defines the overall number of simulations, which is equal to $N\,(2+n)$ where n is the number of uncertain variables, in this case, 6. The numerical experiment differs from the previous analysis since samples are generated from a Sobol' pseudo-random sequence. Thus, the domain bounds have been chosen accordingly to some predefined limits.

Figure 4.5 shows the Sobol' indices for the influence on the GOCE and Tiangong-1 re-

Table 4.6: DA-based methodology, parameters for the sensitivity analysis.

DA order	Max. number of splits	Accepted tolerance	Samples dimension N
4	10	0.0001	1,000,000

entry times, for the numerical Monte Carlo analysis and the DA-based methodology. The first order Sobol' indices $S_{1\,i}$ are in blue, while the total ones are in red $S_{T\,i}$. As a first remark, in each case first-order indices are almost equal to the total ones, and their sum is equal to one. Therefore, it is possible to conclude that uncertainties in the model contributes to a shift in the re-entry time independently, and that their effects is uncorrelated and purely additive.

Figure 4.5a illustrates the result in the GOCE satellite case. The indices refer to the position and velocity in the RSW reference frame. To perform the sensitivity analysis, the 10% of the original standard deviation has been taken.

The only influencing parameters are the in-plane contributions, so the radial and along-track directions. In fact, the cross-track components of the velocity and the position are characterised by a zero index. The reason is that those variations only affect the orientation of the orbital plane in the space, in the i and Ω coordinates, without any consequence on the actual re-entry trajectory, which is only rotated. The most important contribution is the one given by the along-track velocity variation, followed by the radial position, and,

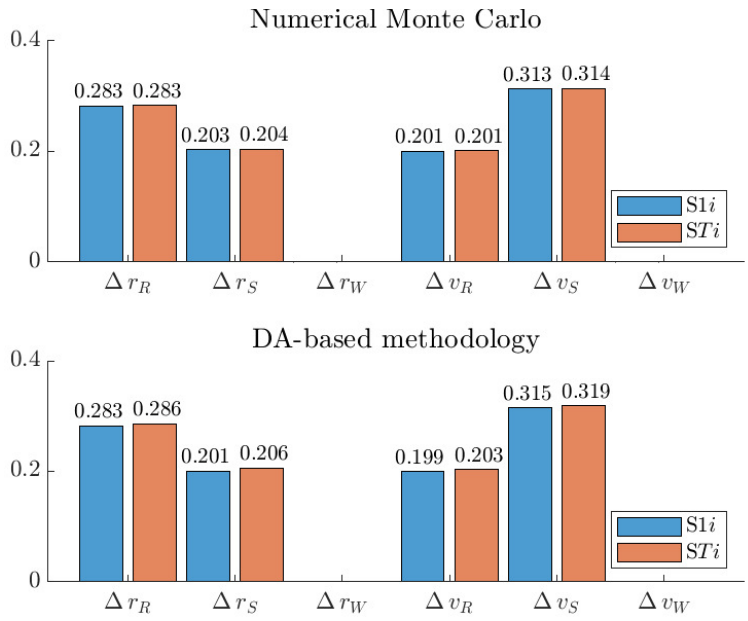

(a) GOCE, position and velocity in the RSW frame

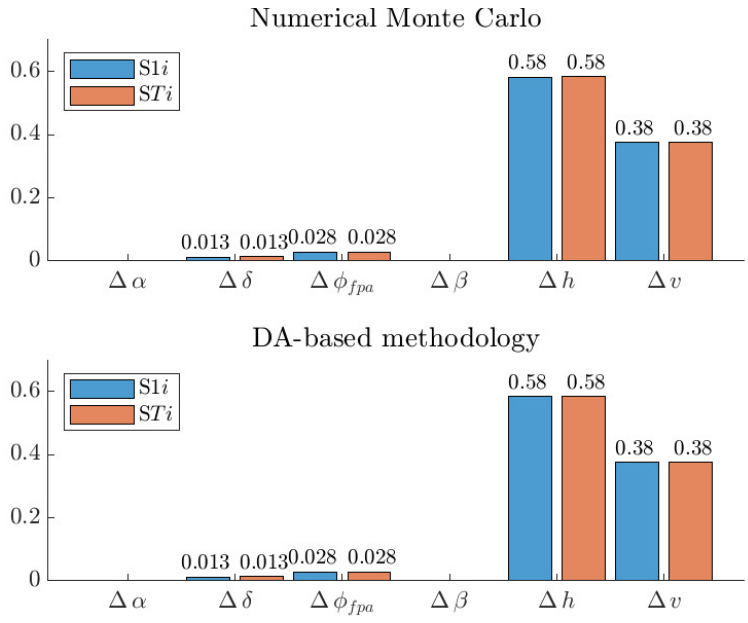

(b) Tiangong-1, flight elements

Figure 4.5: Sensitivity analysis, comparison between the numerical MC and the DA-based methodology.

finally, the contributions caused by a displacement in the along-track position and the radial velocity.
For the Tiangong-1, the sensitivity analysis has been based on the flight elements $\{\alpha, \delta, \phi_{fpa}, \beta, h, v\}$, to provide an alternative elements set for the study of the influence of the parameters on the re-entry time. The domain bounds used are provided in Table 4.7. The values are physically feasible but arbitrarily chosen in accordance with the previous study in Section 3.7. The first order and total Sobol' indices for the flight element set are provided in Figure 4.5b. As expected, the azimuth β has no influence on the re-entry time, because it only produces a rotation of the orbital plane, without affecting the orbital semi-major axis and the eccentricity. In addition, also the right ascension α has no influence on the re-entry time. The most influencing variation is the one applied to the position magnitude h, followed by a displacement in the velocity magnitude v. Also uncertainties in the flight path angle ϕ_{fpa} and the declination δ have a limited influence. In conclusion, the proposed methodology is able to approximate with extremely good

Table 4.7: Standard deviations of error in flight elements.

σ_α [°]	σ_δ [°]	$\sigma_{\phi_{fpa}}$ [°]	σ_β [°]	σ_h [km]	σ_v [m s^{-1}]
0.0002	0.0002	0.0002	0.0002	0.01	0.01

accuracy the indices given by the Monte Carlo simulation, even if only a fraction of the requested samples converges in the constraint satisfaction routine. Also, concerning the processing time, the DA-based approach is computationally less intensive, as shown in Table 4.8. The computational time of the DA-based approach is in both cases 2 times smaller, compared with the numerical Monte Carlo. Therefore, in this particular implementation, the methodology results to be a valid and more economical alternative to the classical Monte Carlo, for the computation of global sensitivity indices.
A final comment concerns the effect of the domain dimensions on the Sobol' indices. In

Table 4.8: Computational time for the sensitivity analysis.

Method	Numerical Monte Carlo	DA-based methodology
Computational time	59 min 36 min	31 min 17 min

fact, global sensitivity indices only depends on the relative ratio between the intervals of each variable. Therefore, when the reciprocal ratio changes, the values of the indices grow in the same direction of the increased dimensions.

Moreover, a scale of the domain dimensions by a constant factor does not affect the values of the indices. Thus, for the GOCE, the domain is only 10% of the initial one, and for the Tiangong-1 the variable intervals are small. Once determined the desired ratios between the variables, it was possible to adopt scaled bounds in order to preserve the DA expansion convergence and the indices accuracy.

Chapter 5

Conclusions and future work

This chapter concludes the thesis work. Section 5.1 includes a summary and some details about the findings of the thesis. Section 5.2 regards the limitations of the research done, which lacks, for instance, of the modelling of the uncertainties in the attitude and the atmospheric composition. In Section 5.3, some major details regarding possible extensions are discussed.

5.1 Summary and findings of the thesis

The present thesis aimed at providing an innovative methodology to study the spacecraft re-entry in the Earth's atmosphere. Accurate predictions of the re-entry epoch and location are required to evaluate possible risks for the population, and typical errors are often of the order of thousands of kilometres, even when simulations are issued one or two hours before the actual event.
The re-entry problem is addressed through the differential algebra mathematical environment. This approach allows to represent the satellite state vector through Taylor series of the initial uncertain variables, and propagate the re-entry. Thus, the polynomial expansion can be evaluated in a cloud of displaced conditions without performing additional integration. The spacecraft is modelled as a point-mass, which initial state is affected by uncertainties. The dynamics of the spacecraft is expressed in averaged form. Semi-analytical methods, based on the King-Hele formulation, are used to model the effect of the atmospheric drag on the orbital semi-major axis and eccentricity. The thesis provides the mathematical formulation of the re-entry modeling, and an analysis of the features of the numerical environment created. The atmospheric density model used is non linear, and built by superimposing exponentially decaying partial atmospheres. The main results from the model analysis have shown how DA expansions are highly affected by

the nonlinearities arising from the numerical integration. In fact, their convergence region is limited, especially when the atmospheric density increases as the satellite approaches the Earth. Further findings from the numerical viewpoint regard the better convergence in the case of low eccentricity orbit, and the validation of uncertainty sets expressed in multiple reference frames.
A particular attention is given to the implementation of the domain splitting and constraint satisfaction routines, which are essential to guarantee the method convergence and the application of realistic uncertainties.
The innovative DA-based methodology is tested on the historical re-entry of two objects, the GOCE satellite and the Chinese space station Tiangong-1. The comparison with numerical Monte Carlo simulation has provided a good accuracy in the estimation of the re-entry PDF, and also a precise approximation of the ground casualty risk map for the impact points distribution. The global sensitivity analysis proved the capability of the DA-based methodology to correctly estimate the Sobol' first-order and total indices, also halving the computational time.

5.2 Limitations

This thesis is not meant to be a full and exhaustive description of the re-entry problem, which is extremely complex to characterise. Therefore, some intrinsic limitations are present, which have been accepted because are not considered relevant for the scopes of the research. Uncertainties in the attitude determination and the atmospheric composition are clearly fundamental if the aim is to reach an acceptable reliability of the re-entry epoch and position forecasts. Also, another interesting aspect that could be worth to investigate is the behaviour of the spacecraft below the fragmentation altitude. Moreover, an event function would be beneficial if the interest consists in knowing exactly the time instant when the fragmentation altitude is reached, and not when it is crossed. Concluding the section, the modelling of additional perturbations would be required to fully describe the satellite motion.

Uncertainties in the re-entry problem
In the thesis, only uncertainties in the initial state vector are considered. In reality, uncertainties in the spacecraft attitude and in the atmospheric composition play a relevant role, completely comparable, if not superior, to the difficulty in determining the exact initial state. In fact, those uncertainties lead together to the unreliability of re-entry predictions. The model discussed in this framework cannot provide the exact re-entry epoch

and position of the objects analysed, because it lacks of those uncertainties modeling. The results are also affected by the use of semi-analytical equations, which are averaged, and therefore an approximation of the full dynamics.
Moreover, the satellite is assumed to be a sphere, thus, the attitude do not play any role, and the tumbling of the spacecraft during the deorbiting phase is not expected to influence its re-entry. Of course, especially for the analysis in Chapter 4, where real reentered objects are considered, this cannot be considered true.
A reliable analysis of the re-entry would require the use of a more accurate atmospheric model, preferably also including the Sun activity, which is seasonally and time varying.

Drag coefficient
The role of the the drag coefficient C_D has not been investigated, since it is not modelled frequently and it is difficult to estimate. The task becomes particularly complex when the spacecraft is tumbling, as it happens during the uncontrolled deorbiting. Moreover, during the re-entry phase, at unspecified altitudes, lift starts to have a role, especially because solar panels may act as wings. Close to the fragmentation altitude, satellites cannot be considered in orbit anymore, this means that the equations describing their motion do not belong anymore to the orbital mechanics field, but they refer to the parabolic flight.

Event function
The integrator developed in the C++ environment lacks of an event function, which would allow to stop the integration exactly when the chosen re-entry altitude is reached. Instead, the current version only interrupts the integration when the re-entry condition is passed.

Additional orbital perturbations
A final limitation regards the possibility to include additional effects to the model, as the luni-solar gravity, which is the strongest perturbation after drag and J_2.

5.3 Remarks for future work

The present work aims to prove the feasibility of the application of semi-analytical methods and differential algebra to the re-entry problem. Therefore, provided that the method has some benefits, a future research would include and investigate other aspects. Atmospheric drag causes the orbit to become circular, which is a singularity condition for the equations used in this thesis. Equinoctial elements would avoid the problem, increasing

the robustness of the model. Moreover, a future study can implement different models for the satellite trajectory, which can potentially avoid the numerical instabilities and nonlinearities induced by the drag effect on the orbital motion. Finally, parallelisation would reduce the whole simulation computational cost.

Equinoctial elements

When the eccentricity is near zero, or even zero, the semi-analytical equations are singular. The re-entry causes the eccentricity to approach singularity conditions. Therefore, further developments would include the use of a different set of orbital elements, for example the equinoctial elements, which do not experience singularities in the presence of circular orbit configurations. The equations of motion in equinoctial elements are available in Vallado [2013].

$$\begin{cases} a_f = k_e = e\,cos(\omega + f_r\,\Omega) \\ n \\ a_g = h_e = e\,sin(\omega + f_r\,\Omega) \\ L = \lambda_M = M + \omega + f_r\,\Omega \\ \chi = p_e = \tan^{f_r}\left(\dfrac{i}{2}\right)\sin(\Omega) = \dfrac{\sin(i)\,\sin(\Omega)}{1+\cos^{f_r}(i)} \\ \psi = q_e = \tan^{f_r}\left(\dfrac{i}{2}\right)\cos(\Omega) = \dfrac{\sin(i)\,\cos(\Omega)}{1+\cos^{f_r}(i)} \end{cases} \tag{5.1}$$

True retrograde equatorial orbits (i = 180 °) are the only cases that cause problems because p_e, q_e are undefined.

f_r is the retrograde factor, it is equal to +1 for all direct orbits and -1 for nearly retrograde orbits, it is introduced to solve the singularity problem. Often it is ignored, since retrograde equatorial orbits are virtually non-existent.

Re-entry theoretical formulation

The final phase of the re-entry is extremely rapid. Before disintegrating in the Earth's atmosphere, the spacecraft loses tens of kilometres of altitude in few seconds, moving from an orbital trajectory to a parabolic path. As demonstrated throughout the thesis, numerical instabilities arise in this phase, causing the DA expansion coefficients to diverge. Therefore, a mathematical formulation, specific for the deorbiting, could potentially limit the numerical instabilities.

In this sense, an alternative model has been applied by Mehta et al. [2015]. The trajectory dynamics of a simple spherical object re-entering the Earth's atmosphere is modeled as a point mass, and tracked through the atmosphere down to ground. The elements representing the satellite state are $\{h,\, V,\, \gamma,\, \chi,\, \phi,\, \lambda\}$. h is the altitude, V is the speed of

the object, γ is the flight path angle, D is the drag force, g is the gravitational acceleration, ω_E is the Earth's rotational speed, R_E is the radius of the Earth, χ is the path direction angle, and ϕ and λ are latitude and longitude respectively. The equations providing their time derivatives are

$$\begin{cases} \dfrac{\mathrm{d}h}{\mathrm{d}t} = V\ \sin\gamma \\ \dfrac{\mathrm{d}V}{\mathrm{d}t} = -\dfrac{D}{m} - g\ \sin\gamma + \omega_E^2(R_E+h)\cos\phi(\sin\gamma\cos\phi - \cos\gamma\cos\chi\sin\phi) \\ \dfrac{\mathrm{d}\gamma}{\mathrm{d}t} = \left(\dfrac{V}{R_E+h} - \dfrac{g}{V}\right)\cos\gamma + 2\omega_E\sin\chi\cos\phi + \\ \qquad + \omega_E^2\left(\dfrac{R_E+h}{V}\right)\cos\phi(\cos\chi\sin\gamma\sin\phi + \cos\gamma\cos\phi) \\ \dfrac{\mathrm{d}\chi}{\mathrm{d}t} = -\left(\dfrac{V}{R_E+h}\right)\cos\phi\sin\chi\tan\phi + 2\omega_E(\sin\phi - \cos\chi\cos\phi\tan\gamma) - \\ \qquad - \omega_E^2\left(\dfrac{R_E+h}{V\cos\gamma}\right)\cos\phi\sin\gamma\sin\chi \\ \dfrac{\mathrm{d}\phi}{\mathrm{d}t} = \left(\dfrac{V}{R_E+h}\right)\cos\gamma\cos\chi \\ \dfrac{\mathrm{d}\lambda}{\mathrm{d}t} = \left(\dfrac{V}{R_E+h}\right)\dfrac{\cos\gamma\sin\chi}{\cos\phi} \end{cases} \tag{5.2}$$

The gravitational acceleration is modeled as a function of the altitude given as

$$g(h) = g_0\left(\frac{h}{R_E+h}\right)^2 \tag{5.3}$$

where the value of g_0 is 9.81 m/s.

Parallel computation benefits

In addition, DA propagation with automatic domain splitting can be implemented to make use of parallelisation techniques as, after splitting, each reference point is propagated independently of all the others. Propagating several boxes in parallel can provide large savings in computational time, while allowing for an increase of the number of polynomials which can be handled. In comparison, to achieve similar results, classical point-wise Monte Carlo simulations would have to be run on massively parallel clusters with tens of thousands of cores. Automatic domain splitting can therefore take significant advantage of parallelisation. Thus, the computational time can be drastically reduced (Wittig et al. [2015]).

Bibliography

Milton Abramowitz and Irene A. Stegun. *Handbook of Mathematical Functions With Formulas, Graphs, and Mathematical Tables*. U.S. Government Printing Office, Washington, D.C., 10th edition, 1972.

Roberto Armellin, Aleksander Lidtke, David Gondelach, Camilla Colombo, Hugh Lewis, Quirin Funke, and Tim Flohrer. Processing two line element sets to facilitate reentry prediction of spent rocket bodies from the geostationary transfer orbit. *The 6th International Conference on Astrodynamics Tools and Techniques (ICATT)*, March 2016.

Javier Martín Ávila. Differential algebra techniques for space applications. Master's thesis, E.T.S.I. Aeronáuticos (UPM), Madrid, 2016.

Martin Berz. *Modern Map Methods in Particle Beam Physics*. Academic press, London, UK, 1999. ISBN 9780120147502.

Martin Berz and Kyoko Makino. *COSY INFINITY version 9 reference manual, MSU Report MSUHEP060803*. Michigan State University, East Lansing, MI 48824, 2006.

Ales Bezděk and David Vokrouhlický. Semianalytic theory of motion for close-Earth spherical satellites including drag and gravitational perturbations. *Planetary and Space Science*, 52(14):1233 – 1249, 2004. ISSN 0032-0633. doi: https://doi.org/10.1016/j.pss.2004.08.004.

Dirk Brouwer. Solution of the problem of artificial satellite theory without drag. *Astronomical Journal*, 64:378, November 1959. doi: 10.1086/107958.

Sean Bruinsma. The DTM-2013 thermosphere model. *J. Space Weather Space Clim.*, 5: A1, 2015. doi: 10.1051/swsc/2015001.

François E. Cellier and Ernesto Kofman. *Continuous System Simulation*. 2006, New York, NY 10013, USA, 2013. ISBN 978-0-387-30260-7.

Stefano Cicalò, James Beck, and Edmondo Minisci. EXPRO+ GOCE Benchmarking re-entry prediction uncertainties, Executive Summary. January 2017.

Camilla Colombo. Planetary orbital dynamics (PlanODyn) suite for long term propagation in perturbed environment. *6th International Conference on Astrodynamics Tools and Techniques (ICATT)*, March 2016.

Camilla Colombo. Long-Term Evolution of Highly-Elliptical Orbits: Luni-Solar Perturbation Effects for Stability and Re-entry. *Frontiers in Astronomy and Space Sciences*, 6, July 2019. doi: 10.3389/fspas.2019.00034.

Camilla Colombo and Colin McInnes. Orbital Dynamics of "Smart-Dust" Devices with Solar Radiation Pressure and Drag. *Journal of Guidance, Control, and Dynamics*, 34 (6):1613–1631, 2011. doi: 10.2514/1.52140.

G. E. Cook, Desmond G. King-Hele, and Michael J. Lighthill. The contraction of satellite orbits under the influence of air drag V. With day-to-night variation in air density. *Philosophical Transactions of the Royal Society of London. Series A, Mathematical and Physical Sciences*, 259(1096):33–67, 1965. doi: 10.1098/rsta.1965.0053.

Howard D. Curtis. In Howard D. Curtis, editor, *Orbital Mechanics for Engineering Students (Third Edition)*. Butterworth-Heinemann, Boston, third edition edition, 2014. ISBN 978-0-08-097747-8. doi: https://doi.org/10.1016/B978-0-08-097747-8.05001-5.

Pierluigi Di Lizia, Franco Bernelli-Zazzera, and Martin Berz. High Order Integration and Sensitivity Analyisis of Multibody Systems using Differential Algebra. *XIX Congress of the Italian Association of Aeronautics and Astronautics*, January 2007.

Pierluigi Di Lizia, Roberto Armellin, and Michèle Lavagna. Application of high order expansions of two-point boundary value problems to astrodynamics. *Celestial Mechanics and Dynamical Astronomy*, 102:355–375, December 2008. doi: 10.1007/s10569-008-9170-5.

John R. Dormand and Peter J. Prince. A family of embedded Runge-Kutta formulae. *Journal of Computational and Applied Mathematics*, 6(1):19 – 26, 1980. ISSN 0377-0427. doi: https://doi.org/10.1016/0771-050X(80)90013-3.

Jim Fletcher J and Ram Sharma. Lifetime Estimation of the Upper Stage of GSAT-14 in Geostationary Transfer Orbit. *International Scholarly Research Notices*, 2014, October 2014. doi: 10.1155/2014/864953.

Stefan Frey, Camilla Colombo, and Stijn Lemmens. Extension of the King-Hele orbit contraction method for accurate, semi-analytical propagation of non-circular orbits. *Advances in Space Research*, 64(1):1 – 17, 2019. ISSN 0273-1177. doi: https://doi.org/10.1016/j.asr.2019.03.016.

Jacco Geul, Erwin Mooij, and Ron Noomen. TLE uncertainty estimation using robust weighted differencing. *Advances in Space Research*, 59(10):2522 – 2535, 2017. ISSN 0273-1177. doi: https://doi.org/10.1016/j.asr.2017.02.038.

Jacco Geul, Erwin Mooij, and Ron Noomen. Analysis of Uncertainties and Modeling in Short-Term Reentry Predictions. *Journal of Guidance, Control, and Dynamics*, 41: 1–14, February 2018. doi: 10.2514/1.G003258.

David Gondelach, Aleksander Lidtke, Roberto Armellin, Camilla Colombo, Quirin Funke, and Tim Flohrer. Re-entry prediction of spent rocket bodies in GTO. *26th AAS/AIAA Space Flight Mechanics Meeting*, February 2016.

René Hoogendoorn, Erwin Mooij, and Jacco Geul. Uncertainty Propagation for Statistical Impact Prediction of Space Debris. *Advances in Space Research*, 61, October 2017. doi: 10.1016/j.asr.2017.10.009.

Luigi G. Jacchia. Thermospheric Temperature, Density, and Composition: New Models. *SAO Special Report*, 375, 1977.

Desmond King-Hele. *Theory of satellite orbits in an atmosphere.* Butterworths Mathematical Texts, London, 1964. ISBN 978-0-216-92252-5.

Joseph J. F. Liu. Advances in orbit theory for an artificial satellite with drag. *Astrodynamics Conference*, August 1982. doi: 10.2514/6.1982-1399.

Mauro Massari, Pierluigi Di Lizia, Francesco Cavenago, and Alexander Wittig. Differential Algebra software library with automatic code generation for space embedded applications. January 2018. doi: 10.2514/6.2018-0398.

Piyush Mehta, Martin Kubicek, Edmondo Minisci, and Massimiliano Vasile. Debris re-entry modeling using high dimensional derivative based uncertainty quantification. *AAS/AIAA Astrodynamics Specialist Conference, ASC 2015*, October 2015.

Edmondo Minisci, Romain Serra, Massimiliano Vasile, Annalisa Riccardi, Stuart Grey, and Stijn Lemmens. Uncertainty treatment in the GOCE re-entry. *1st IAA Conference on Space Situational Awareness (ICSSA)*, November 2017.

Alessandro Morselli. *High order methods for Space Situational Awareness*. PhD thesis, Politecnico di Milano, 2014.

Carlos Ortega Absil, Romain Serra, and Massimiliano Vasile. De-orbiting and re-entry analysis with generalised intrusive polynomial expansions. *International Astronautical Congress*, September 2016.

Carmen Pardini and Luciano Anselmo. Re-entry predictions of three massive uncontrolled spacecraft. *23rd International Symposium on Space Flight Dynamics*, October 2012.

Carmen Pardini and Luciano Anselmo. Re-entry predictions for uncontrolled satellites: results and challenges. May 2013.

Carmen Pardini and Luciano Anselmo. Assessing the risk and the uncertainty affecting the uncontrolled re-entry of manmade space objects. *Journal of Space Safety Engineering*, 5(1):46 – 62, 2018. ISSN 2468-8967. doi: https://doi.org/10.1016/j.jsse.2018.01.003.

Carmen Pardini and Luciano Anselmo. Monitoring the orbital decay of the Chinese space station Tiangong-1 from the loss of control until the re-entry into the Earth's atmosphere. *Journal of Space Safety Engineering*, 6(4):265 – 275, 2019. ISSN 2468-8967. doi: https://doi.org/10.1016/j.jsse.2019.10.004.

Alfio Quarteroni, Riccardo Sacco, and Fausto Saleri. *Numerical Mathematics (Texts in Applied Mathematics)*. Springer-Verlag, Berlin, Heidelberg, 2006. ISBN 3540346589.

Mirco Rasotto, Alessandro Morselli, Alexander Wittig, Mauro Massari, Pierluigi Di Lizia, Roberto Armellin, C. Y. Valles, and Guillermo Ortega. Differential algebra space toolbox for nonlinear uncertainty propagation in space dynamics. *The 6th International Conference on Astrodynamics Tools and Techniques (ICATT)*, March 2016.

Joseph F. Ritt. *Differential Algebra*. American Mathematical Society, Providence, RI, 1950. ISBN 0486616665.

Alexander Ronse and Erwin Mooij. Statistical Impact Prediction of Decaying Objects. *Journal of Spacecraft and Rockets*, 51, August 2013. doi: 10.2514/6.2013-4682.

Andrea Saltelli, Marco Ratto, Terry Andres, Francesca Campolongo, Jessica Cariboni, Debora Gatelli, Michaela Saisana, and Stefano Tarantola. *Global Sensitivity Analysis. The Primer*, volume 304. January 2008. doi: 10.1002/9780470725184.ch6.

Ilya M. Sobol. Global sensitivity indices for nonlinear mathematical models and their Monte Carlo estimates. *Mathematics and Computers in Simulation*, 55(1):271 – 280,

2001. ISSN 0378-4754. doi: https://doi.org/10.1016/S0378-4754(00)00270-6. The Second IMACS Seminar on Monte Carlo Methods.

Zhen-Jiang Sun, Pierluigi Di Lizia, Franco Bernelli-Zazzera, and Yazhong Luo. High-Order State Transition Polynomial with Time Expansion Based on Differential Algebra. *4th IAA Conference on Dynamics and Control of Space Systems*, May 2018.

Graham. G. Swinerd, W. J. Boulton, and Desmond G. King-Hele. Contraction of satellite orbits in an oblate atmosphere with a diurnal density variation. *Proceedings of the Royal Society of London. A. Mathematical and Physical Sciences*, 383(1784):127–145, 1982. doi: 10.1098/rspa.1982.0124.

Noelia Sánchez-Ortiz, Nuria Guijarro López, Ignacio Grande, Luis Tabera, Adam White, Sean Bruinsma, and Stijn Lemmens. *Re-entry Prediction Uncertainties derived from Environmental and Observation considerations*. Darmstadt, DE, April 2017.

Mirko Trisolini and Camilla Colombo. A density-based approach to the propagation of re-entry uncertainties. *27th International Symposium on Space Flight Dynamics*, February 2019.

Mirko Trisolini, Hugh Lewis, and Camilla Colombo. Demisability and survivability sensitivity to design-for-demise techniques. *Acta Astronautica*, 145, January 2017. doi: 10.1016/j.actaastro.2018.01.050.

David A. Vallado. *Fundamentals of Astrodynamics and Applications*. Microcosm Press, Hawthorne, CA, 4th edition, 2013. ISBN 1881883140.

Nguyen X. Vinh, James M. Longuski, Adolf Busemann, and Robert D. Culp. Analytic theory of orbit contraction due to atmospheric drag. *Acta Astronautica*, 6(5):697 – 723, 1979. ISSN 0094-5765. doi: https://doi.org/10.1016/0094-5765(79)90028-6.

Alexander Wittig. Differential Algebra Lab. 2015.

Alexander Wittig, Roberto Armellin, Camilla Colombo, and Pierluigi Di Lizia. Long-term orbital propagation through differential algebra transfer maps and averaging semi-analytical approaches. *24th AAS/AIAA Space Flight Mechanics Meeting*, pages 339–357, September 2014a.

Alexander Wittig, Pierluigi Di Lizia, Roberto Armellin, Franco Bernelli-Zazzera, Kyoko Makino, and Martin Berz. An automatic domain splitting technique to propagate uncertainties in highly nonlinear orbital dynamics. *Advances in the Astronautical Sciences*, 152, February 2014b.

Alexander Wittig, Pierluigi di Lizia, Roberto Armellin, Kyoko Makino, Franco Bernelli-Zazzera, and Martin Berz. Propagation of large uncertainty sets in orbital dynamics by automatic domain splitting. *Celestial Mechanics and Dynamical Astronomy*, 122: 239–261, 2015.

Alexander Wittig, Camilla Colombo, and Roberto Armellin. Long-term density evolution through semi-analytical and differential algebra techniques. *Celestial Mechanics and Dynamical Astronomy*, 128, February 2017. doi: 10.1007/s10569-017-9756-x.